On topography-related dynamics in the Argentine Basin

Léa Poli

Thèse de Doctorat de Sorbonne Université

Sciences de l'environnement d'Ile de France

Ecole doctorale 129

Laboratoire d'Océanographie et du Climat : Expérimentation et Approches Numérique

Léa Poli

On topography-related dynamics in the Argentine Basin

Defended the 03-10-2023 in front of the jury :

Damien Cardinal	LOCEAN,SU,Paris	Jury chairman
Irene Polo	UCM,Madrid	Rapporteur
M.D.Pérez Hernández	IOCAG,ULPGC,Las Palmas	Rapporteur
Boris Dewitte	CERFACS, Toulouse	Jury member
Jérôme Sirven	LOCEAN,SU,Paris	Thesis supervisor
Camila Artana	ICM,Barcelone	Thesis co-supervisor
Christine Provost	LOCEAN,Paris	Thesis supervisor

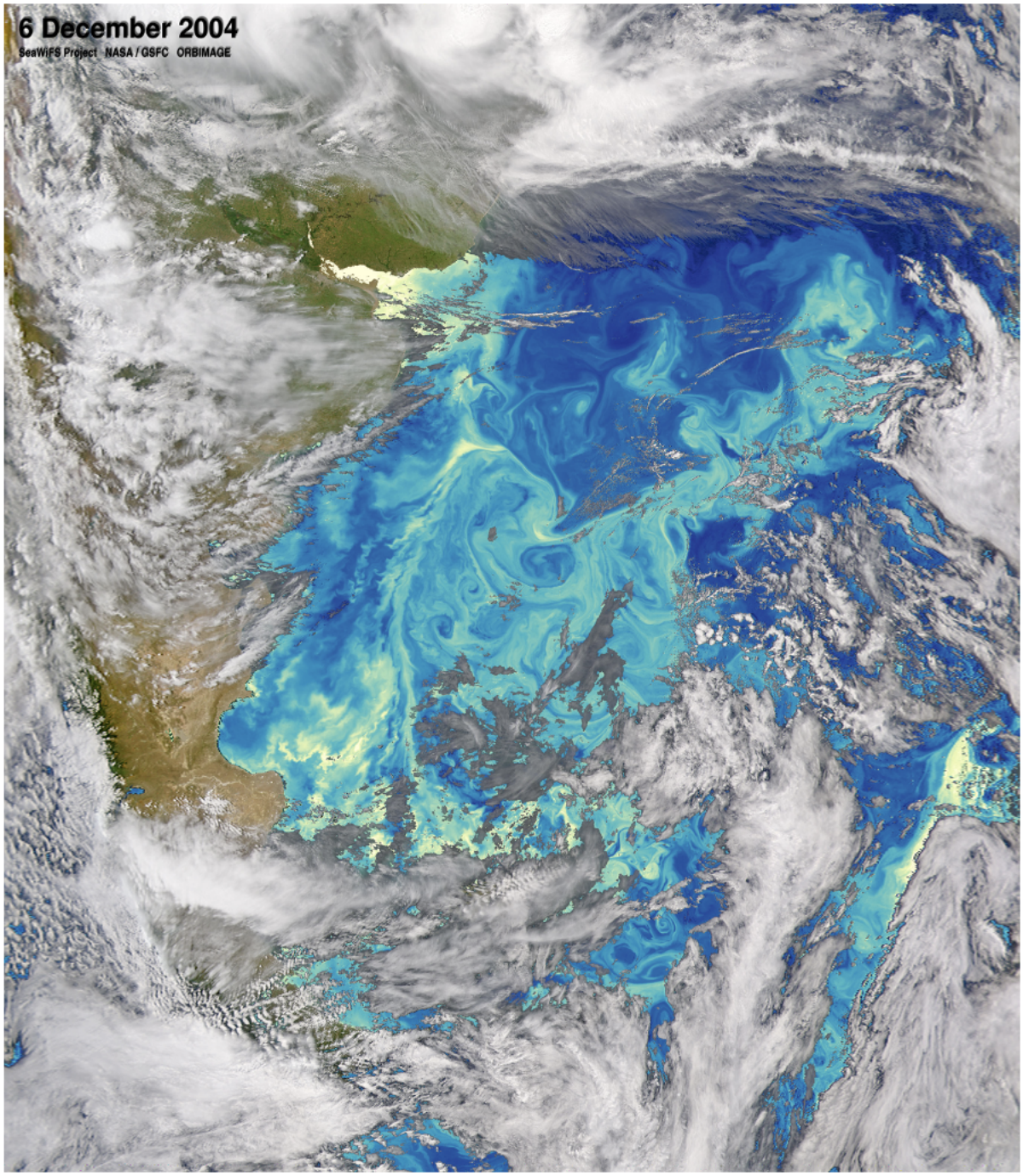

Figure 1: Phytoplankton bloom in the Malvinas current : nutrient-rich, cold and fresh water masses from the Antarctic circumpolar current are transported toward the north by the Malvinas current. https://earthobservatory.nasa.gov/images/5123/beautiful-blooms-in-south-atlantic-ocean.

Scientific Activities during the Ph.D.

Publications in peer-reviewed scientific journals :

- **Poli, L.**, Artana, C.,Provost, C., Siven,J., Le Blanc-Pressenda,R., Collapses, maxima, multi-year modulation and trends of the Zapiola anticyclone: insights from Mercator Reanalysis.(submitted)

- **Poli, L.**, Artana, C., Provost, C. (2022). Topographically trapped waves around South America with periods between 40 and 130 days in a global ocean reanalysis. Journal of Geophysical Research: Oceans, 127, e2021JC018067. https://doi.org/10.1029/2021JC018067.

- **Poli, L.**, Artana, C., Provost, C., Sirven, J., Sennéchael, N., Cuypers, Y., Lellouche, J.-M. (2020). Anatomy of subinertial waves along the Patagonian shelf break in a 1/12° global operational model. Journal of Geophysical Research: Oceans, https://doi.org/10.1029/2020JC016549

- Artana, C., Provost, C., Ferrari, R., Bricaud, C., **Poli, L.**, Park, Y.-H. (2022). Tides, internal and near-inertial waves in the Yermak Pass at the entrance of the Atlantic Water to the Arctic Ocean. Journal of Geophysical Research: Oceans, 127, e2022JC019082. https://doi.org/10.1029/2022JC019082.

- Artana, C., Provost, C., **Poli, L.**, Ferrari, R., Lellouche, J.-M. (2021). Revisiting the Malvinas Current upper circulation and water masses using a high-resolution ocean reanalysis. Journal of Geophysical Research: Oceans, 126, e2021JC017271. https://doi.org/10.1029/2021JC017271.

- Abot, L., Provost, C., **Poli, L.**, (2023) Recent Convection Decline over the Northern Nordic Seas: an insight from the Mercator Ocean System over 2008-2023 DOI: 10.1029/2022JC019320.

International conferences:

- **Poli, L.**, Artana, C., and Provost, C.: Topographically Trapped Waves Around South America: Oceanic Teleconnections between Equatorial Pacific and Tropical Atlantic, EGU General Assembly 2023, Vienna, Austria, 24–28 Apr 2023, EGU23-3178, https://doi.org/10.5194/egusphere-egu23-3178, 2023.Oral presentation.

- Provost, C., Artana, C., Ferrari, R., Bricaud, C., **Poli, L.**, and Park, Y.-H.: Tides, Internal and Near-Inertial Waves in the Yermak Pass at the Entrance of the Atlantic Water to the Arctic Ocean., EGU General Assembly 2023, Vienna, Austria, 24–28 Apr 2023, EGU23-3330, https://doi.org/10.5194/egusphere-egu23-3330, 2023.Oral presentation.

- Artana, C. and Provost, C.: Intense Anticyclones and Near Inertial Trapped Waves at the Global Argentine Basin Array of the Ocean Observatory Initiative, EGU General Assembly 2023, Vienna, Austria, 24–28 Apr 2023, EGU23-3318, https://doi.org/10.5194/egusphere-egu23-3318, 2023. Poster that i presented.

- Abot, L.,Provost, C., **Poli, L.**, Recent Convection Decline in the Greenland Sea - insights from the Mercator Ocean System over 2008-2020, EGU General Assembly 2023, Vienna, Austria, 24–28 Apr 2023, EGU23-3170, https://doi.org/10.5194/egusphere-egu23-3170, 2023. Oral presention by Louise Abot.

- **Poli, L.**, Artana, C., Provost, C., Topographically Trapped Waves around South America with periods between 40 and 130 days in a global ocean reanalysis, DOI: 10.24400/527896/a03-2022.3532. Keynote Oral Session. Ocean Surface Topography Science Team Meeting 2022, Venice, Italy.

- **Poli, L.**, Artana, C., Provost, C., Sirven, J., Sennéchael, N., Cuypers, Y., Lellouche, J.-M.: Anatomy of subinertial waves along the Patagonian shelf break in a 1/12° global operational model. Online conference. Ocean Surface Topography Science Team Meeting, 2020.

- **Poli, L.**, Artana, C., Provost, C., Sirven, J., Sennéchael, N., Cuypers, Y., Lellouche, J.-M.: Anatomy of subinertial waves along the Patagonian shelf break in a 1/12° global operational model. Online conference. European Geophysical Union Meeting, 2020.Oral presentation.

Teaching

- Tutorial classes: 64 hours per year
  - First year of bachelor: "Earth, Environment, Climate: external earth" Introduction to oceanography, meteorology, hydrology and paleoclimate.
  - Third year of bachelor : "Physical oceanography"
- Co-supervision of interns:
  - Ruben Leblanc Pressenda: ARGO floats data analyses in the Argentine Basin.
  - Adrien Bella: Study of the variability in the Yaghan Basin, Drake passage, using mooring observations and Glorys12 model outputs.
  - Mareva July Wormit: Biogeochemistry in the Argentine Basin, insight from Ocean Observatory Initiative in-situ observations, biogeochemical model outputs developed at Mercator Ocean, and satellite observations.
  - Mae Presas Ferrer (ULPGC): Assessing the temporal variability of the subantarctic front and the polar front across the Malvinas Plateau using a global ocean reanalysis.

Courses

- Courses ED129 : Changement climatique : sciences, sociétés, politique (24h)
- Courses ED129 : Impacts du changement climatique (21h)

Field work

Within a French-Spanish collaboration we (C. Artana and I) could participate to an oceanographic cruise on the R/V Sarmiento de Gamboa. The cruise started on March 08 2021 from Punta Arenas (Chile) and ended on April 15 2021 in Las Palmas (Gran Canaria) and waspreceeded by 3 week-confinement in Punta Arenas to prevent any COVID cases.

Abstract

The Argentine Basin (>5000 m) is home to rather unique oceanic structures of prime importance to the global circulation. In this thesis, we focus on elements of circulation (ocean waves and currents) constrained by topography. To the west, the Patagonian continental shelf of variable slope and direction hosts a variety of topographic waves. By combining outputs of a high-resolution reanalysis (GLORYS12), in-situ and satellite data, two types of sub-inertial waves were documented, fast and slow waves. Fast waves propagating along the Patagonian shelf break, with phase velocities between 1 m/s and 7 m/s, periods ranging from 5 to 130 days and wavelengths from 1,200 to 12,000 km. Their characteristics depend upon stratification, slope, shelf width, latitude and mean flow. High-frequency waves with periods between 5 and 40 days are often locally forced by strong variations of the zonal wind south of 47°S(Poli et al., 2020), whereas lower-frequency waves with periods between 40 and 130 days propagate from the equatorial Pacific to the tropical Atlantic (22°S, Poli et al., 2022). The Madden-Julian Oscillation (MJO) plays a key role in forcing these low-frequency waves in two ways. (a) By an oceanic teleconnection involving equatorial Kelvin waves reaching the American west coast, and (b) by an atmospheric teleconnection reinforcing southerly winds in the southeast Pacific. In addition, local winds, which are not necessarily linked to the MJO, modulate and trigger low-frequency waves (40-130 days period) in specific locations, such as the Brazil-Malvinas confluence and the Drake Passage. All these waves have an impact on along-shore currents : during the positive phase, the near-surface current is increased by around 0.1 m/s. In addition, these waves contribute to the supply of nutrients sustaining the high primary production on the Patagonian shelf. Slow waves propagate in the core of the Malvinas Current with phase velocities between 0.10 and 0.30 m/s, periods around 20, 60 and 100 days, and wavelengths ranging between 450 and 1200 km. These waves were tracked back to Drake Passage and the Malvinas Escarpment.

In the center of the basin, the Zapiola anticyclone is located above a sedimentary deposit and displays an intensity equivalent to that of the strongest ocean currents (>100 Sv) with enhanced bottom velocities reaching 0.1 m/s. Using GLORYS12 reanalysis, we constructed a time series of Zapiola transport. Transport reaches extreme values ranging from -18 Sv to 250 Sv. The extrema show a seasonal distribution, with a majority of weak events occuring in austral winter. When the Zapiola anticyclone collapses, it becomes more permeable to the influences of surrounding waters, and the water charac-

teristics in the center of the Zapiola are modified. In particular, cyclonic eddies originating from the polar front penetrate up to the center. During strong events, wind stress curl is reinforced and turbulent kinetic energy is enhanced around the anticyclone. The region around the Zapiola anticyclone exhibits a multi-year modulation, with periods of 4-5 years (1993-1997, 1998-2003 and 2004-2009) of low (high) salinity corresponding to low (high) transport. Over the last 27 years, waters of the Argentine basin became warmer and saltier in the first 2000 m of the water column. These trends are concomitant with an increase of turbulent kinetic energy in the south of the basin which is probably associated with the southward migration of the subtropical front (Poli et al., 2023).

Résumé

Le Bassin Argentin (>5000 m) abrite des structures océaniques uniques et de première importance pour la circulation mondiale. On se concentre dans cette thèse sur des éléments de circulation (ondes et courants) contraints par la topographie. A l'ouest, le talus continental Patagonien de pente et direction variables est parcouru par une grande variété d'ondes topographiques. En combinant les sorties d'une réanalyse océanique de haute résolution (GLORYS12), des données in-situ et satellitaires, nous avons mis en évidence deux familles d'ondes sub-inertielles, des ondes rapides et des ondes longues : Des ondes rapides se propageant le long de la rupture du plateau continental patagonien avec des vitesses de phase comprises entre 1 m/s et 7 m/s, des périodes allant de 5 à 130 jours et des longueurs d'ondes allant de 1200 à 12000 km. Leurs propriétés sont fonction de la stratification, de la pente du talus et de la largeur du plateau, de la latitude, et du courant moyen. Des ondes de haute fréquence avec des périodes comprises entre 5 et 40 jours sont souvent forcées localement par des fortes variations du vent zonal au sud de 47°S (Poli et al., 2020), tandis que des ondes de plus basse fréquence avec des périodes entre 40 et 130 jours se propagent du Pacifique équatorial à l'Atlantique tropical (22°S, Poli et al., 2022). L'oscillation de Madden-Julian (MJO) joue un rôle clé dans le forçage de ces ondes de basse fréquence de deux manières: (a) par une téléconnexion océanique impliquant des ondes de Kelvin équatoriales atteignant la côte ouest américaine et (b) par une téléconnexion atmosphérique renforçant les vents du sud dans le Pacifique sud-est. En outre, les vents locaux, qui ne sont pas nécessairement liés à la MJO, modulent et déclenchent des ondes de basse fréquence (de période entre 40 et 130 jours) à des endroits spécifiques, tels que la confluence Brésil-Malouines et le Passage de Drake. Toutes ces ondes ont un impact sur les courants de bord : pendant la phase positive des ondes, le courant près de la surface augmente 0,1 m/s. Ces ondes participent à l'apport de nutriments soutenant la forte production primaire sur la plateforme patagonienne. Des ondes plus lentes sont observées dans le cœur du courant des Malouines. Leur vitesse de phase est comprise entre 0.10 à 0.30 m/s, leur période autour de 20, 60 et 100 jours et leur longueur d'onde comprise entre 450 et 1200 km. Elles proviennent du passage de Drake et de l'escarpement des Malouines (Poli et al., 2020).

Au centre du bassin, l'Anticyclone de Zapiola est situé au-dessus d'un dépôt sédimentaire et montre une intensité équivalente à celle des plus puissants courants océaniques (>100 Sv) avec des vitesses renforcées au fond, qui atteignent 0.1 m/s. A l'aide de la réanalyse GLORYS12 nous avons construit une

série temporelle de transport du Zapiola. Le transport atteint des valeurs extrêmes allant de -18 Sv à 250 Sv. Les extrema présentent une distribution saisonnière avec une majorité d'événements faibles en hiver austral. Lorsque l'anticyclone du Zapiola s'effondre, il devient plus perméable aux influences des eaux environnantes et les caractéristiques des eaux au centre du Zapiola sont modifiées. En particulier des tourbillons cycloniques provenant du front polaire pénètrent jusqu'au centre. Lors des événements forts, le rotationnel du vent est renforcé et l'énergie cinétique turbulente est augmentée autour de l'anticyclone La région autour de l'anticyclone du Zapiola présente une modulation multi annuelle avec des périodes de 4-5 ans (1993-1997,1998-2003 et 2004-2009) de faible (forte) salinité correspondant à un transport faible (fort). Au cours des 27 dernières années, le bassin Argentin voit ses eaux devenir plus chaudes et plus salées dans les 2000 m. Ces tendances sont concomitantes avec une augmentation d'énergie cinétique turbulente au sud du bassin probablement associé à la migration vers le sud du front subtropical (Poli et al., 2023).

Contents

1 Introduction **11**

1.1 The Argentine Basin 11

1.2 The two western boundary currents: the Malvinas and Brazil Currents. 13

1.3 The Patagonian Shelf 16

1.4 The Zapiola Anticyclonic Circulation: 19

1.5 Ph.D. Objectives 21

2 Anatomy of Subinertial Waves Along the Patagonian Shelf Break in a 1/12° Global Operational Model. **24**

3 Topographically Trapped Waves around South America with periods between 40 and 130 days in a global ocean reanalysis : An Oceanic teleconnection between the equatorial Pacific and the tropical Atlantic. **47**

4 Collapses, maxima, multi-year modulation and trends of the Zapiola anticyclone: insights from Mercator Reanalysis. **66**

5 Conclusions and perspectives **116**

5.1 Conclusions 116

5.2 Perspectives on waves 120

5.2.1 Origins of slow waves in the core of the MC 120

5.2.2 Fast Waves along the Patagonian Platform 121

5.3 Perspectives on the Zapiola anticyclonic circulation and the Argentine Basin. 124

5.3.1 Bottom circulation in the Argentine Basin. 124

5.3.2 High frequency modes of variability within the Basin 124

5.3.3 Water masses transformation in the Argentine Basin. 125

5.3.4 Climate projections on Zapiola circulation 126

Chapter 1

Introduction

The ocean is a key element of the climate system. It covers 71% of the earth surface, drives weather patterns and controls the climatic variations by exchanging heat, moisture and carbon with the atmosphere. In recent years, the ocean has stored at least 89% of the heat excess due to human-induced greenhouse gas emissions, making climate change irreversible (Von Shuckman et al., 2020).Ocean dynamics controlled the distribution of heat and carbon ocean uptake.

1.1 The Argentine Basin

The Argentine Basin located in the Southwest Atlantic reaches depths between 3000 m and 6000 m and is delimited by the Mid-Atlantic Ridge to the east and the shallow (<200m) and wide (> 1000 km at 49°S) Patagonian Platform to the west bordered by a sinuous slope of variable steepness. Between 52°S and 49°S, isobaths between 300m and 3000m are west-east orientated and the slope is gentle (2,000 m over 300 km), at 45°S the isobaths merge and the slope steepens. To the south of the Argentine Basin, the relatively shallow (< 2000 m) Malvinas Plateau (52°S-48°S - 58°W-32°W) is bounded to the north by a steep wall called the Malvinas Escarpment with a zonal extension of about 3000 km (Figure 1.1a). A gap located at 37°W-49°S cuts the escarpment. At the center of the Basin, the Zapiola rise, a sedimentary deposit, centered at 45°S-45°W stretches in the zonal direction and it submit is about 1200 m above the abyssal plain (Ewing et al., 1964; Le Pichon et al., 1971). To the southwest of the Zapiola rise the slope is steep due to the presence of a wide depression reaches 6000 m. To the north east of the Zapiola rise,

the slope is gentle with maximum depth of 5000 m. The Argentine Basin is thus a quasi-closed basin where the dynamics are closely related to the topography.

The deep Argentine Basin is the main conduit for water masses between the Atlantic and the Southern Ocean (Jullion et al., 2010) as it is located between the Antarctic Circumpolar Current (ACC) and the subtropical gyre (Figure 1.1b).

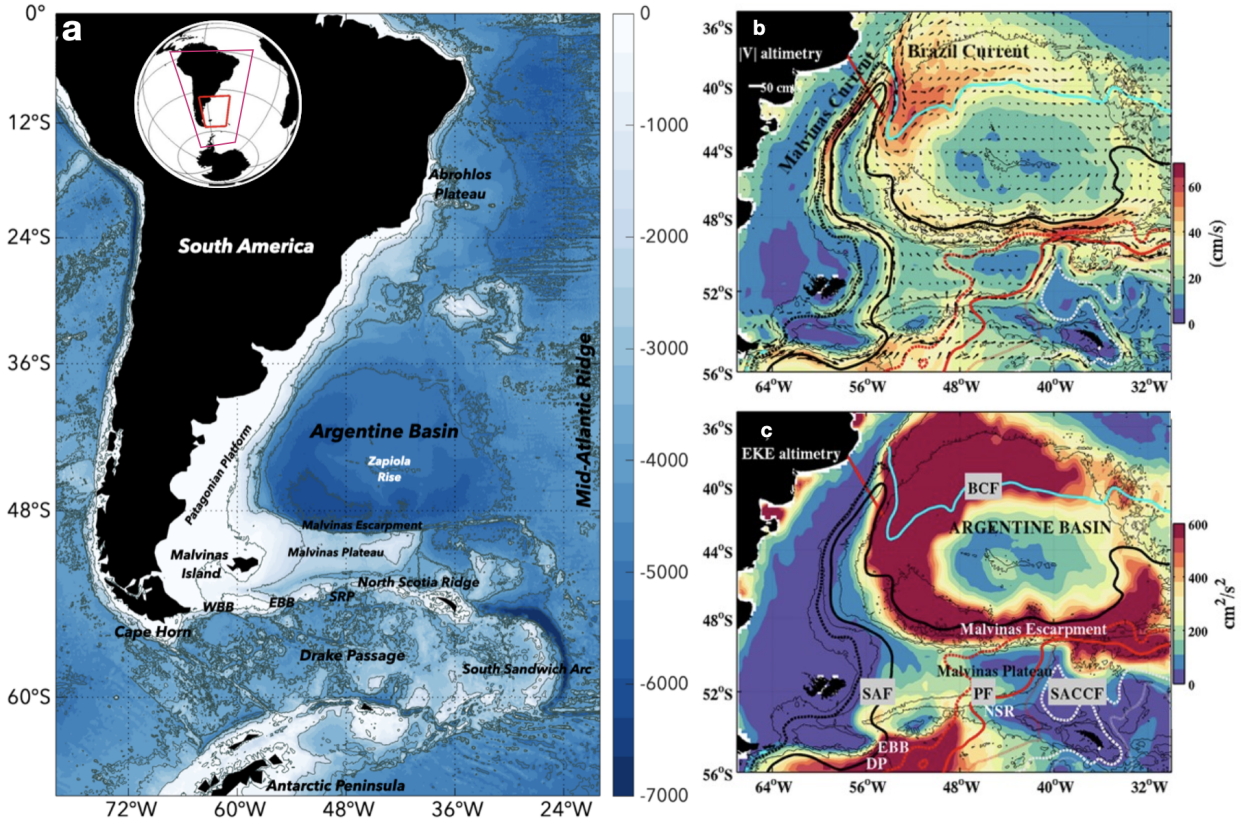

Figure 1.1: a) Bathymetry around South America in from Smith and Sandwell (1994) Mean surface velocity magnitude (in cm/s). b) mean surface velocities (larger than 10 cm/s) from gridded altimetry for the 2007–2016 period. c) Mean eddy kinetic energy per unit mass (in cm2/s2) for the 2007–2016 period. The mean locations of the main Antarctic Circumpolar Current (ACC) fronts as defined by Barré et al. (2011) are plotted: Subantarctic Front (SAF), in black (SAF-M solid line and SAF-N dashed line); Polar Front (PF), in red (PF-M solid line and PF-N and PF-S dashed line); and Southern ACC (SACCF) in grey (SACCF-N and SACCF-S in dashed lines).(Pannels b and c from Artana et al., 2018).

The Argentine Basin is one of the most energetic regions of the world ocean in terms of mean flow and mesoscale activity (Mason et al., 2017). Two strong currents flow along the western boundary : the Malvinas Current (MC) and the Brazil Current (BC) (Figure 1.1b). The encounter of the MC and the BC, known as the Brazil-Malvinas Confluence (BMC) generates strong mesoscale activity with surface Eddy Kinetic Energy (hereafter EKE) exceeding 0.2 m^2s^{-2} (Figure 1.1c). At the center of the Basin, a

minimum of EKE is associated with the Zapiola Anticyclonic circulation.

1.2 The two western boundary currents: the Malvinas and Brazil Currents.

The MC is a powerful western Boundary current (with a mean transport at 41°S of 38 Sv, Artana et al., 2019, Figure 1.2) which emanates from the ACC. Because of the topographic barrier of the South Sandwich Arc (Figure 1.1a), the ACC fronts veer to the north and cross the North Scotia Ridge through several passages. The Polar front crosses the ridge through the Shag Rock Passage (SRP in Figure 1.1a) and veers eastward following the Malvinas Escarpment. The Subantarctic Front (made of two branches, the northern (SAF-N) and main branch (SAF-M)) makes its way through passages located to the west (WBB) and east of Burdwood (EBB) Bank (Peterson and Whitworth, 1989). Both branches cross the shallow Malvinas Plateau and follow the Patagonian continental slope forming the MC. The MC is a barotropic-equivalent current (Vivier & Provost, 1999). The MC comprises two narrow jets south of 43°S alineated with two bottom terraces (Frey et al., 2021, Piola et al., 2013). The northern branch follows the SAF-N and flows along the 200m isobath (Artana et al., 2021) while the main jet follows the main SAF along the 1,500-m isobath (Artana et al., 2018a). At 45°S, the isobaths converge, the jets join and surface velocities reach 0.6 m/s (Figure 1.1 b, Artana et al., 2021).

The MC flows northward up to 38°S where it retroflects southward forming a sharp cyclonic loop called the Malvinas return flow (MRF, Peterson & Whitworth, 1989). At 38°S, the MC encounters the BC the western boundary current of the subtropical gyre which advects southward warm and salty subtropical waters southward. The region of encounters of the two currents is called the BMC and is associated with lateral temperature gradients as high as 1°C per 100 m (Barré et al., 2006; Gordon & Greengrove, 1986) and is one of the most energetic region of the world ocean in terms of meso and submesoscale. At the collision with the BC, the MC splits in two branches: the inner branch keeps flowing northward sinking below the BC while the outer branch forms the MRF (Artana et al., 2019; Provost et al., 1995).

The BC has a mean transport increasing with latitude (20 Sv at 36°S, Artana et al., 2019). The BC leaves the continental slope at about 38°S, that is nearly 15° north of the zero isoline in the mean wind

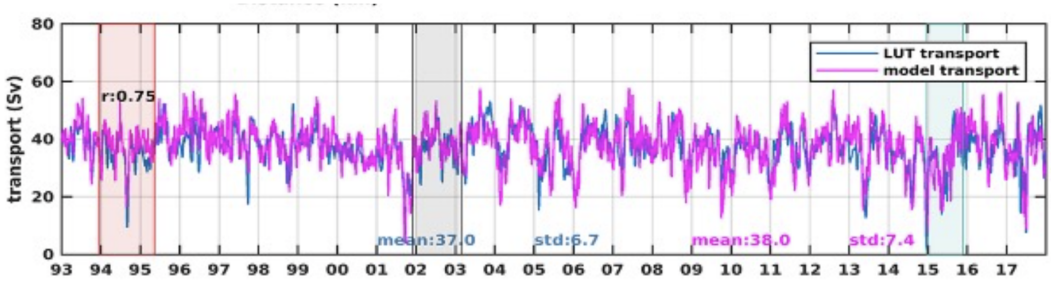

Figure 1.2: Malvinas Current volume transport in Sv computed with the Look up table method in the upper 1,500 m (blue) and model outputs in the upper 900 m (magenta). The in-situ measurements periods are indicated in colors. (From Artana et al.,2019)

stress curl. The role of the dynamics of two colliding jets has been invoked to explain the BC mean separation latitude (or mean subtropical front (STF) location) with theoretical and numerical models (e.g., Agra & Nof, 1993; Matano, 1993). Those studies suggest that the MC imparts a momentum responsible for determining the mean latitude of separation of the STF from the slope. The latitude of separation of the BC from the slope has been observed to vary at different time scales. At the seasonal scale the location of the separation of the STF from the slope shows excursion of about 200 km along the 2,000-m isobath with a poleward migration in austral summer and equatorward shift in winter (Saraceno et al., 2005). Part of the BC, referred to as the overshoot of the BC (BCO), flows southward and returns to the northeast at about 45°S, the other part of the BC flows eastward along the STF forming the South Atlantic Current.

The MC, which connects two of the most energetic regions of the world ocean, the Drake Passage and the BMC, is rather steady and exhibits weak EKE values (Figure 1.1c). Part of the EKE coming from the Drake Passage is dissipated through bottom friction and mixing over the Malvinas Plateau (Artana et al., 2019, Figure 1.3a, visible as a minimum in Figure 1.1c). The MC shows a little seasonality relative seasonal standard deviation of 2 % and no significant trend in the last 27 years (Artana et al.,2019, Figure 1.2).

The MC transport at 41°S in the upper 900m exhibits synoptic extrema (Figure 1.2). Maxima and minima are associated with eddies coming from the Argentine Basin: transport maxima (in blue in Figure 1.3c) are associated with cyclonic eddies detached from the PF and transport minima (in red in Figure 1.3c) with southward displacement of the Subantarctic Front due to large anticyclonic anomalies from the BC. Downstream the MC transport is perturbed by "blocking events" occuring approximately once

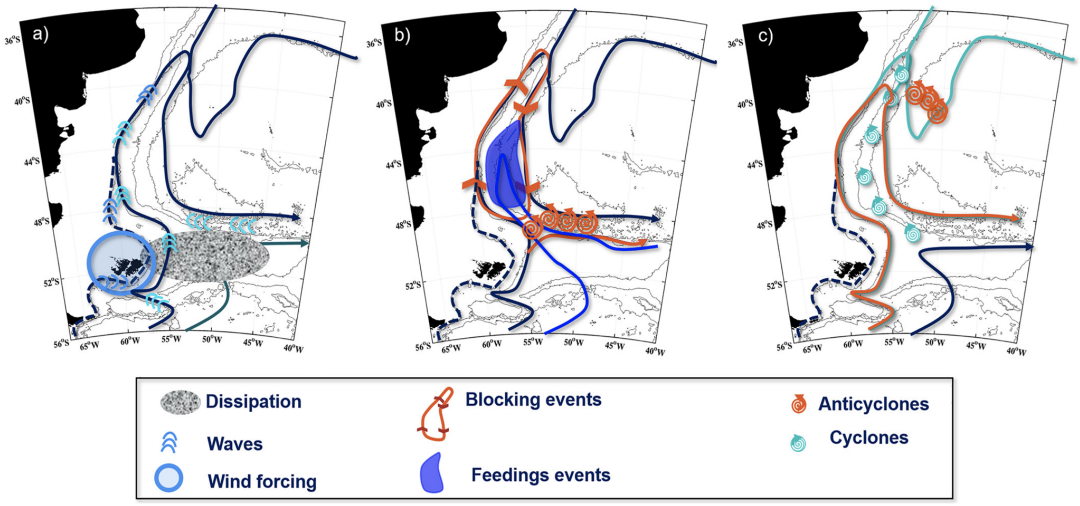

Figure 1.3: Schematics of physical processes in the MC (a) Gray shading represents dissipation over the Malvinas Pateau of the mesoscale activity leaking through North Scotia Ridge (Artana et al.,2016). Trapped waves (locally wind forced and remotely forced) propagating along the Patagonian slope are schematized in blue (Poli et al., 2020). (b) Blocking events in red: anticyclonic anomalies cut the MC from the Antarctic Circumpolar Current at 49°S; the MC does not collapse as a recirculation cell is established (Artana et al., 2016, Artana et al., 2018c). Feeding events in blue: waters from the South of the Polar Front are injected into the MC and recirculate between the MC and Malvinas Return Flow (Artana et al., 2018c). (c) Maxima and minima of the MC transport at 41°S are associated with eddies coming from the Argentine Basin: Transport maximum cases (in blue) are associated with cyclonic eddies detached from the PF and transport minimum cases (in red) with southward displacement of the Subantarctic Front due to large anticyclonic anomalies from the Brazil Current (Artana, et al., 2018b). (Figure from Artana et al., 2021)

a year (documented by Artana et al., 2018c, Figure 1.3b), during which the MC is cut from it source at 49°S by anticyclonic perturbations coming from the Malvinas Escarpment. The MC does not collapse as a recirculation cell is established (Artana et al., 2016, Artana et al., 2018c). Episodes of "feeding" events have also been documented : in some occasions, the jet associated with the PF-N meanders north of the Malvinas Plateau and feeds the recirculation between the MC and the MRF with polar waters (Figure 1.3b).

However, the MC plays a minor role in the velocity variations observed at the confluence at seasonal and interannual scales. Velocity trends are small over the MC while they are large at the BMC and the overshoot (0.1 m/s/decade at the surface) as the BC migrated southward over the last 25 years (Artana et al., 2021). Over the last decade, the number of blocking events at 59°W became more frequent (35 during 93-05 and 65 during 05-17). The southward displacement of the BC overshoot could contribute to that increase (Artana et al., 2021).

The MC transports up to 38°S cold and nutrient rich subantarctic waters which play a key role in the development of the rich ecosystem present over the Patagonian platform. Therefore, understanding the dynamics of the MC is key for the knowledge of the bio-physical phenomenon occurring in the region. The spectral analysis of in-situ (measured velocities) and satellite observations (derived transport) (Vivier & Provost, 2001, Spadone & Provost, 2009, Artana et al., 2019) highlighted the presence of oscillations at periods around twenty days and between 40 and 130 days probably associated with trapped waves propagating along the Patagonian slope.

1.3 The Patagonian Shelf

The Patagonian continental shelf is one of the largest continental shelf of the planet and one of the richest in living (a vast marine ecosystem) and non-living resources (oil and gas reservoirs). The Patagonian continental shelf-break presents chlorophyll concentrations as large as those observed in eastern boundary upwelling systems ($> 0.25 - 0.30$ mg/m^3, Figure 1.4a). They are associated with the observed massive phytoplankton blooms (Romero et al., 2006; Valla and Piola, 2015). Biological abundance of this region cascades from phytoplankton to higher trophic levels: scallops, anchovies, hakes, squids, etc (e.g. Acha et al., 2004). As a consequence, this region hosts one of the largest fisheries of the world (Figure 1.4b).

Namely the southern Ocean is known as a High-Nutrient Low-Chlorophyll Region (HNLC, Venables

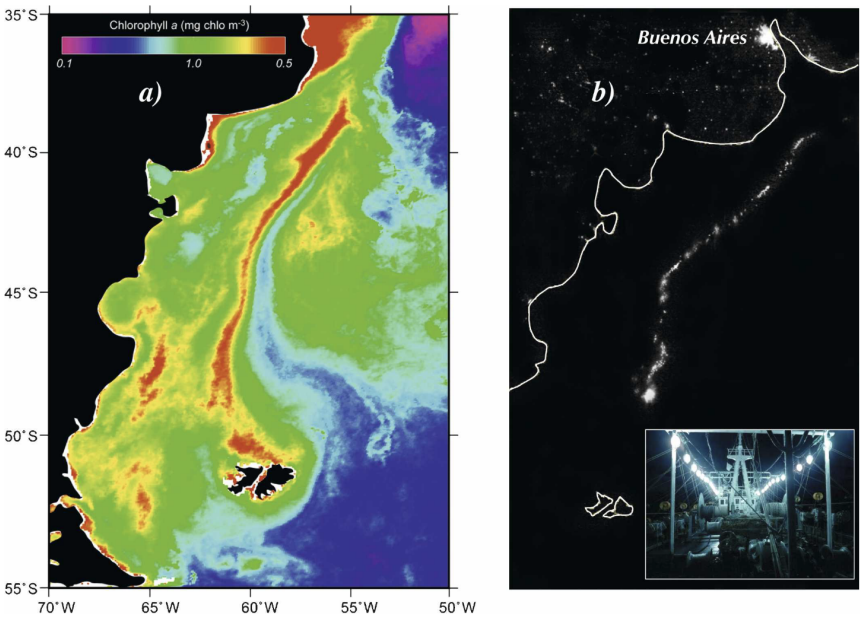

Figure 1.4: (a) Summer values of surface chlorophyll-a derived from SeaWiFS (mg m^{-3}) in the Patagonia region; (b) nighttime lights in the southwestern Atlantic. The lights over the Patagonian shelf break are generated by squid fishing vessels (inset) (after Rodhouse et al., 2001). (From Matano and Palma., 2008)

& Moore, 2010); indeed the primary production is low and fairly constant despite the availability of macronutrients (such as phosphate, nitrites, silicates and nitrates). The limiting factor to the primary production is the availability of micronutrients (e.g., iron, zinc, cobalt). The micronutrients are present over the Patagonian Platform due to atmospheric deposition of dust coming from the south American continent and sediment–water exchange (Figure 1.5 c). The macronutrients are advected from the south by the MC which flows northward along the shelf break bringing cold, nutrient-rich Subantarctic waters (Figure 1.5 a,b and d). Our understanding of the mechanisms that produce the shelf-break blooms of chlorophyll-a is still fragmentary despite the crucial role they play in sustaining the whole food chain.

Indeed, advection of nutrients from the MC to the patagonian platform implies cross-shelf exchanges associated with upwelling episodes (Valla & Piola., 2015). Valla & Piola [2015] suggest that the shelf-break dynamics are controlled by the MC divergence with respect to the continental slope. Trapped waves (TW) have been proposed as a possible mechanism that enhances nutrient fluxes to the upper layer and affects the primary production of the Patagonian Shelf, as they have an influence in coastal circulation, exchanges and mixing (Huthnance, 1995). In-situ observations have pointed at the possible existence of TWs propagating northward along the Patagonian slope. Velocity spectra obtained from current-meter moorings deployed at 41°S across the slope near the BMC showed large energy peaks

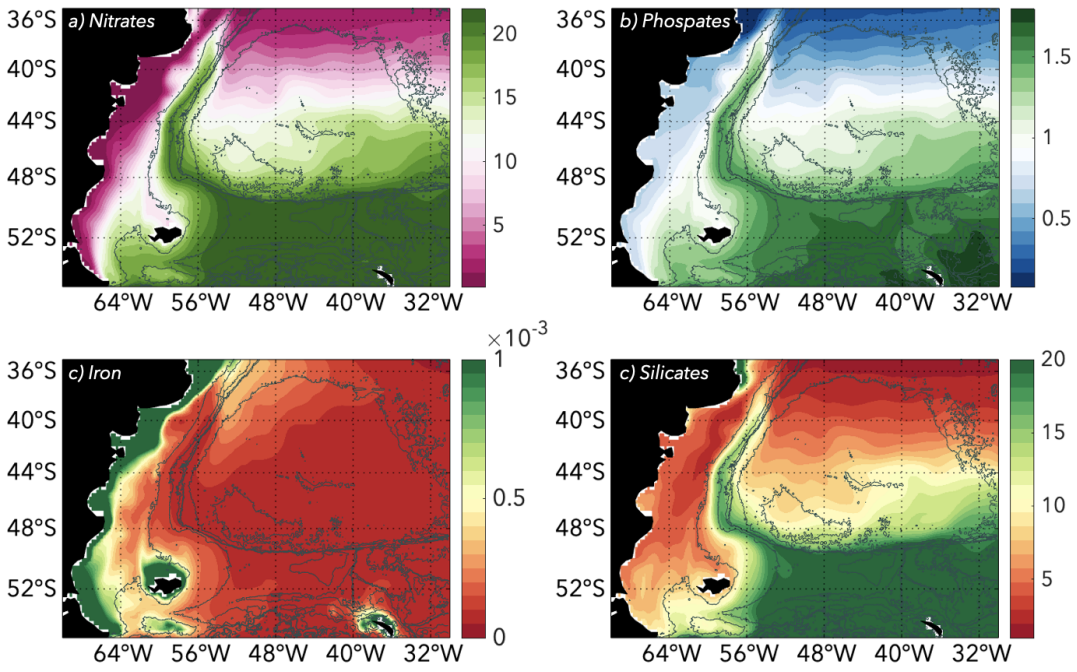

Figure 1.5: Surface distribution of nitrates (a), phosphates (b) iron (c) and silicates(d) in $mmol/m^3$ from the biogeochemical hindcast for global ocean produced at Mercator-Ocean (https://doi.org/10.48670/moi-00019).

between 5 and 110 days (Vivier & Provost, 1999; Vivier et al., 2001). Despite these observations, there is still no characterization of TWs along the Patagonian slope. As the TWs propagate rapidly, they are not entirely resolved in satellite-altimetry-derived maps of sea level anomalies (SLAs) (Ballarotta et al., 2019). The transport time series at 41°S computed from Altimetry exhibits a lower standard deviation than the one computed from the global ocean reanalysis (Figure 1.2) . Indeed, even if the variance preserving spectra of both transports exhibit peaks at similar periods (intraseasonal, semiannual, and annual period, Figure 1.6), the spectrum of the model transport shows differencies at periods between smaller than 100 days and especially at periods lower than 20 days. This lack of energy at high frequency has been attributed to TWs, as they are aliased in altimetry data (Nyquist frequency of 14 days) and better resolved in the model.

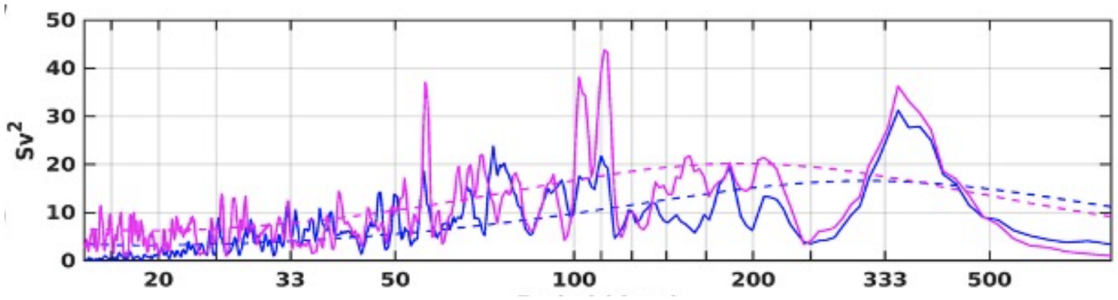

Figure 1.6: Variance preserving spectra of the LUT (blue) and model (magenta) MC volume transport. The dotted line shows the 90% confidence level against the red noise background from a first-order autoregressive process.(from Artana et al., 2019).

1.4 The Zapiola Anticyclonic Circulation:

The Zapiola anticyclonic circulation (hereafter ZAC) is located at the center of the Argentine basin above a sedimentary deposit of the Zapiola Rise. The ZAC signs in the mean EKE as a minimum (Figure 1.1c). The existence of the ZAC was unknown untill the late 80's where Flood & Shor, [1988] inferred the presence of anticyclonic bottom flow around the Zapiola Drift from analysis of mud wave structures. This first guess have been corroborated by near-bottom current meters measurements in the subsequent years in the southern (Whitworth et al., 1991) and northern branch (Weatherly, 1993) of the ZAC. They measured mean flows of about 0.1 m/s in southeastward and northwestward directions. During the World Ocean Circulation Experiment (WOCE) Hydrographic Program Section A11 sampled across the ZAC at 45°S in 1993 (Saunders & King, 1995). They estimated a synoptic transport up to 175 Sv from CTD data and Shipborn ADCP. A small mean transport of 50 Sv was obtained using altimetry-derived surface geostrophic velocities over the period 1993-2007 (Saraceno et al., 2009) whereas Argo float drift velocities at 1000 m over the period 2004-2010 led to a larger mean transport of 140 Sv (Colin de Verdiere and Ollitrault, 2016). Recently, Johnson and King, [2023] estimated a mean ZAC transport of 110 Sv using deep Argo temperature-salinity profiles and historical shipboard CTD. They also highlighted the bottom intensified nature of the ZAC. The Zapiola Anticyclone is believed to be driven by energy transfers from the strong mesoscale eddy kinetic energy to the mean kinetic energy (e.g De Miranda et al., 1999, Bigorre and Dewar, 2009). The ZAC itself is a local minimum in EKE and hosts mainly cyclonic eddies (Saraceno and Provost, 2012).

Saraceno et al., [2009] produced a transport time series derived from altimetry data which exhibit a substantial time variability with values ranging between 78 to +128 Sv (Figure 1.7). Thus at times

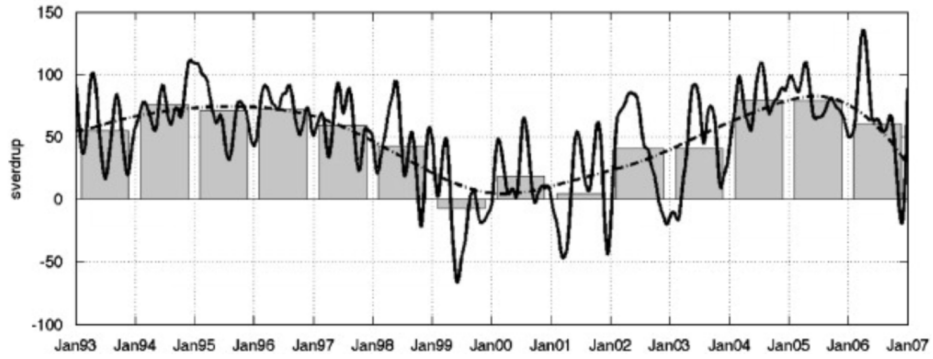

Figure 1.7: 90 days low-passed filtered ZAC transport time series and the analogous average with a 4.3-year filter, by a dash-dotted line. (from Saraceno et al., 2009)

the ZAC collapses. The vertical structure in terms of velocities and water masses associated with those collapses have not been explored yet. The ZAC contributes to the stirring of the strongly contrasted water masses of different remote origins. Near the surface it promotes exchanges between the polar waters from the ACC and the tropical waters from the South Atlantic Current. At depth, elements of the deep waters formed in the North Atlantic (as the North Atlantic Deep Water) encounter waters formed off the Antarctic Continent (as the Lower Circumpolar Deep Water or the Upper Circumpolar Deep Water), and the stirring and mixing associated with the ZAC possibly constitute an important factor in determining the characteristics of global deep water masses.

1.5 Ph.D. Objectives

We focus on several elements of circulation (ocean waves and currents) constrained by topography and aim at providing elements of answer to the following questions :

We first examine on trapped waves along the Patagonian Platform :

- What types of waves propagate along the Patagonian Slope ?
- How are they triggered ?
- How do the structure of the waves evolve during their propagation ?
- What are the impact of the waves on the background circulation ?
- How are they represented in the different sets of observations and in a global ocean reanalysis ?

We then extend our analysis to the whole South American slope. Then we explore the ZAC trying to answering to the following questions:

- How is the ZAC organized in the vertical ?
- How does the ZAC transport vary and what is happening during ZAC collapses in terms of circulation pattern and forcings ?
- Is there a connection between hydrographic characteristics in the basin and the ZAC transport ?
- What are the trends in the last thirty years in terms of hydrographic properties, wind forcing and dynamics (e.g EKE evolution) in the Argentine Basin?

To provide some answers to these questions we use in-situ observations, satellite observations and model outputs.

We use tide gauges data, ARGO float measurements and mooring current-meter data.

Within a French-Spanish collaboration we (C. Artana and I) could participate to a oceanographic cruise on the R/V sarmiento de Gamboa and deploy 10 ARGO floats (5 classic and 5 deep) in the ZAC(the location of deployment is indicated in Figure 1.8a). The cruise started on March 08 2021 from Punta Arenas (Chile) and ended on April 15, 2021, in Las Palmas (Gran Canaria).

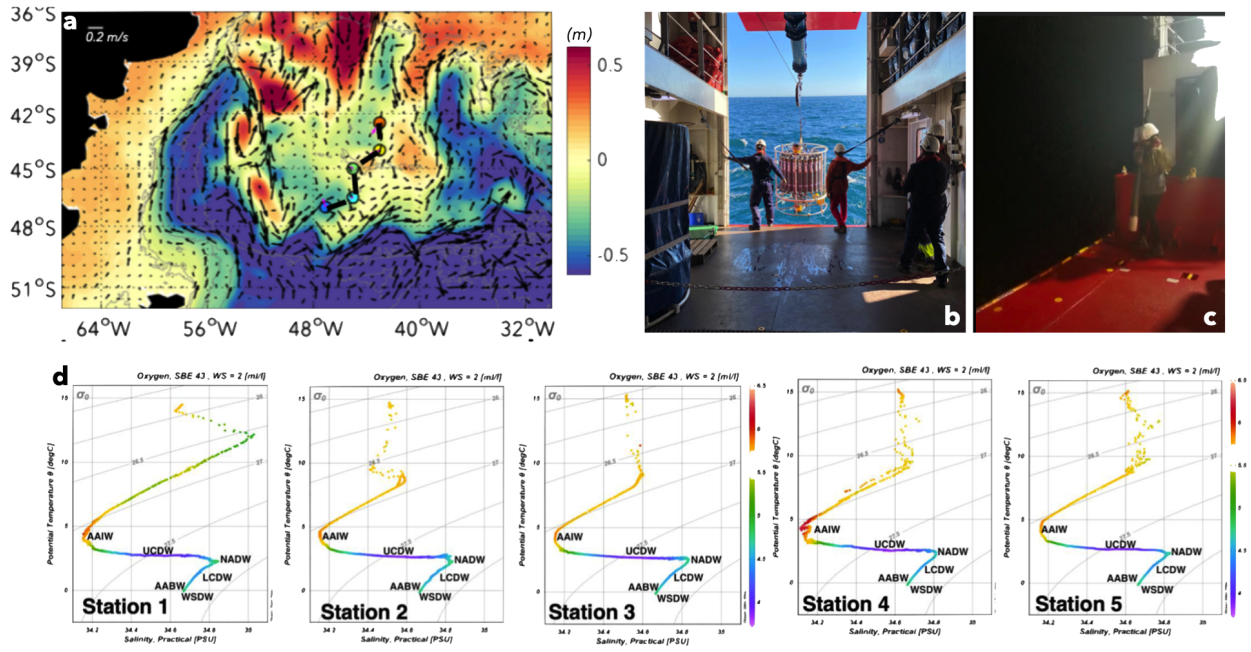

Figure 1.8: a) SSH and surface velocities from operational mercator model averaged over the 12, 13 and 14 March 2021. Colors circles show the deployment locations of CTD and LADCP. b) Niskin bottles and CTD. c) ARGO float deployment. d) $\theta - S$ diagrams measured by the CTD. Colors indicate measured oxygen in ml/l.

The ARGO floats were provided by Coriolis in the framework of the BACI LEFE GMMC project. The floats were successfully deployed. The main objective was to document the circulation at 1000 and 3000 m and the water masses between 0 and 4000 m.

We also used current-meter moorings deployed in 1993–1995, 2001–2003, and 2014–2015 across the continental slope at 41°S near the Confluence (Ferrari et al., 2017; Spadone & Provost, 2009; Vivier & Provost, 1999) and tide gauges data.

We used Data Unification and Altimeter Combination System (DUACS) delayed-time altimeter gridded (1/4° regular grid) daily product (Pujol et al., 2016; Taburet et al., 2019) available at http://marine.copernicus.eu/. This product results from an optimal interpolation in space and time, combining measurements from different satellite altimeters. Its effective resolution is about 20 days in time and 200 km in space (e.g. Archer et al., 2020).

To replace all those observations in a larger spatio-temporal context we used the high-resolution (1/12°) global Mercator Ocean reanalysis (hereafter GLORYS12) which has been developed in the framework of the Copernicus Marine Environment Monitoring Service (CMEMS, http://marine.copernicus.eu/). GLORYS12 covers the period from 1993 to 2019 (Lellouche et al., 2021). The ocean surface is forced by

the global ERA-Interim atmospheric reanalysis from the European Center for Medium-Range Weather Forecasts. The Mercator model jointly assimilates along track satellite altimetric data, satellite sea surface temperature, sea-ice concentration, and in-situ temperature and salinity vertical profiles (Lellouche et al., 2021). It uses a reduced-order Kalman filter with a 3-D multivariate modal decomposition of the background error and a 7-day assimilation cycle (Lellouche et al., 2021). Artana et al. (2018 a and c) evaluated the performance of the GLORYS12 reanalysis over the Malvinas Current and found a good agreement with observations. We performed further model assessment using different sets of independent and non-independent data and found an overall good agreement.

The thesis is organized as follows :

In the second chapter, we examine trapped waves propagating along the Patagonian platform. We first compare possible signatures of TW in observations and the Mercator Ocean reanalysis in along-shore velocity and sea level. Then we explore fast waves detected at the shelf break above the 300m isobath and interpret them using the idealized model from Brink and Chapman (1987). Linear theory is presented in the Appendix. Slower velocity variations in the core of the MC above the 1500 m isobath are also examined.

In the third chapter, we examine TWs at periods ranging between 40 and 130 days propagating all around South America. These waves constitute an oceanic teleconnection between the equatorial Pacific and the tropical Atlantic. We first further assess GLORYS12 reanalysis comparing model SLA with observations from tide gauges located around South America. We then explore the sea level spectral content around South America and the propagation characteristics of the waves. Finally, we investigate the wave occurrences, the forcing mechanism, the vertical structure and the impact on along-shore velocities around South America.

In the fourth chapter, we examine the ZAC. We first focus on the general circulation of the Argentine Basin and produce a 27-year-long ZAC transport time-series which was used to select extreme events compsising weak and strong transport events. Then, we focus on the hydrographic properties of the Argentine Basin with particular interest in long term trends, low-frequency changes and extreme events. Finally, we discuss the role of transient kinetic energy and wind stress curl in shaping the ZAC.

Ultimately, in chapter five, we conclude and present the perspective of this thesis.

Chapter 2

Anatomy of Subinertial Waves Along the Patagonian Shelf Break in a 1/12° Global Operational Model.

TW have been proposed as a possible mechanisms that could modulate the transport from the nutrient-rich Malvinas Current up to the Patatagonian Platform. We investigate the dynamics associated with

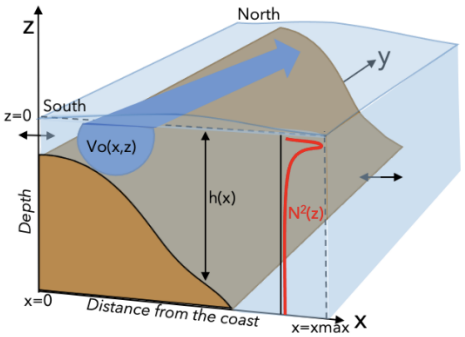

Figure 2.1: Set-up of the linear model with its associated coordinates system. The infinite coastline is at $x = 0$; the topography is defined by a function $h(x)$ and the mean hydrography characterized by the Brünt-Väisälä frequency $N^2_\infty(z)$. There is a meridional mean flow $V_o(x, z)$.

these waves and rely on linear theory (described in Appendix). The idealized framework is shown in Figure 2.1. The coastline is straight, follows a South-North direction, and defines the y axis ($x = 0$).

The mean ocean surface is at $z = 0$ (upward orientation of the z coordinate axis). The ocean is above a continental slope defined by a function $z = -h(x)$. The ocean is stratified, with a mean Brünt-Väisälä frequency $N^2_\infty(z)$ depending only on z. The Coriolis parameter is f and its latitudinal dependence is neglected (f plane). ,Moreover we assume that the ocean is in hydrostatic equilibrium and the Boussinesq approximation can be made.

AGU ADVANCING EARTH AND SPACE SCIENCE

JGR Oceans

RESEARCH ARTICLE
10.1029/2020JC016549

Key Points:

- Velocity signals with phase speeds of 140–300 cm/s at the shelf break and 10–30 cm/s in the core of the Malvinas Current (MC) were identified
- At the shelf break, wind-forced fast waves modulated the inner MC jet and possibly contributed to upwelling
- Slowly propagating waves in the core of the MC came from the Malvinas Escarpment or the Drake Passage

Correspondence to:
C. Artana,
cartlod@locean-ipsl.upmc.fr

Citation:
Poli, L., Artana, C., Provost, C., Sirven, J., Sennéchael, N., Cuypers, Y., & Lellouche, J.-M. (2020). Anatomy of subinertial waves along the Patagonian shelf break in a 1/12° global operational model. *Journal of Geophysical Research: Oceans*, *125*, e2020JC016549. https://doi.org/10.1029/2020JC016549

Received 25 JUN 2020
Accepted 12 NOV 2020

Anatomy of Subinertial Waves Along the Patagonian Shelf Break in a 1/12° Global Operational Model

Léa Poli[1], Camila Artana[2], Christine Provost[1], Jérôme Sirven[1], Nathalie Sennéchael[1], Yannis Cuypers[1], and Jean-Michel Lellouche[2]

[1]LOCEAN-IPSL, Sorbonne Université (UPMC), Paris, France, [2]Mercator Ocean, Parc Technologique du Canal, Ramonville Saint Agne, France

Abstract The Patagonian slope hosts a variety of waves. We used a state-of-the-art ocean reanalysis to examine waves at the shelf break and in the core of the Malvinas Current (MC) at periods larger than 10 days. Statistics over 25 years indicated three types of signals: in phase signals at specific locations of the shelf break to the south of 47°S; fast propagating signals all along the shelf break (phase speed from 140 to 300 cm/s) at periods between 5 and 110 days; and slower signals in the core of the MC (phase speeds from 10 to 30 cm/s) at 20-day, 60-day, and 100-day periods. The large zonal wind stress variations south of 47°S forced in-phase along-slope velocity variations and triggered fast propagating waves at distinct sites corresponding to abrupt changes in the shelf-break orientation. The shelf-break waves modulated the intensity of the inshore jet, which varied from 0 to 30 cm/s at 100 m depth, and had spatial and temporal structures and scales consistent with those of observed upwelling events. Slow propagating waves in the core of the MC had along-slope wavelengths between 450 and 1,200 km and were not forced by the local winds. They were tracked back to the Drake Passage and the Malvinas Escarpment.

Plain Language Summary The sinuous Patagonian slope hosts a variety of waves that are yet poorly documented. We examined the waves in a state-of-the-art ocean model assimilating observations. Strong westerly winds forced fast waves at the shelf break. These waves modulated the intensity of the coastal jet of the Malvinas Current (MC) and the shelf-break upwelling. Slow waves propagating from the Malvinas Escarpment and the Drake Passage modified the velocities of the MC main jet.

1. Introduction

The Malvinas Current (MC), a major western boundary current of the South Atlantic Ocean, is an offshoot of the Antarctic Circumpolar Current (Figure 1a) that flows northward following the Subantarctic Front (SAF) along the eastern continental slope of South America. The MC, which borders one of the widest continental shelves of the world, is strongly controlled by bottom topography. Between 52°S and 49°S, the bottom slope is west-east orientated and gentle (2,000 m over 300 km) and the MC is rather wide (300 km) with mean northward surface velocities of 30 cm/s (Figures 1a and 1b). At 48°S, isobaths are east-west orientated and the MC mean surface velocities are zonal with a mean value of 40 cm/s. The largest mean surface velocities in the MC (>60 cm/s) are observed north of 43°S where the bottom slope is steep (Figures 1a and 1b) and the MC is organized in one narrow jet. South of 43°S, the MC is characterized by a relatively stable two-jet structure alienated with two bottom terraces (Piola et al., 2013). The mean location of the onshore jet corresponds to a northern branch of the SAF (SAF-N), while the main jet follows the main SAF along the 1,500-m isobath (Figure 1b; Artana et al., 2018). At 38°S, the MC encounters the Brazil Current forming the Brazil-Malvinas Confluence. The surface eddy kinetic energy (EKE) at this region is among the greatest in the world ocean with values exceeding 2,000 cm^2/s^2 (Figure 1c). In contrast, the EKE in the MC is rather small (200 cm^2/s^2) since the Malvinas Plateau filters a large part of the mesoscale activity from Drake Passage (Artana et al., 2016).

In situ observations have pointed at the possible existence of trapped waves (TW) propagating northward along the Patagonian slope. Velocity spectra obtained from current-meter moorings deployed at 41°S across the slope near the Brazil Malvinas Confluence showed large energy peaks between 5 and 110 days (Vivier & Provost, 1999; Vivier et al., 2001). Despite these observations, there is still no characterization of TW along the Patagonian slope. As the TW propagates rapidly, they are not entirely resolved in satellite-altimetry-derived maps of sea level anomalies (SLAs) (Ballarotta et al., 2019).

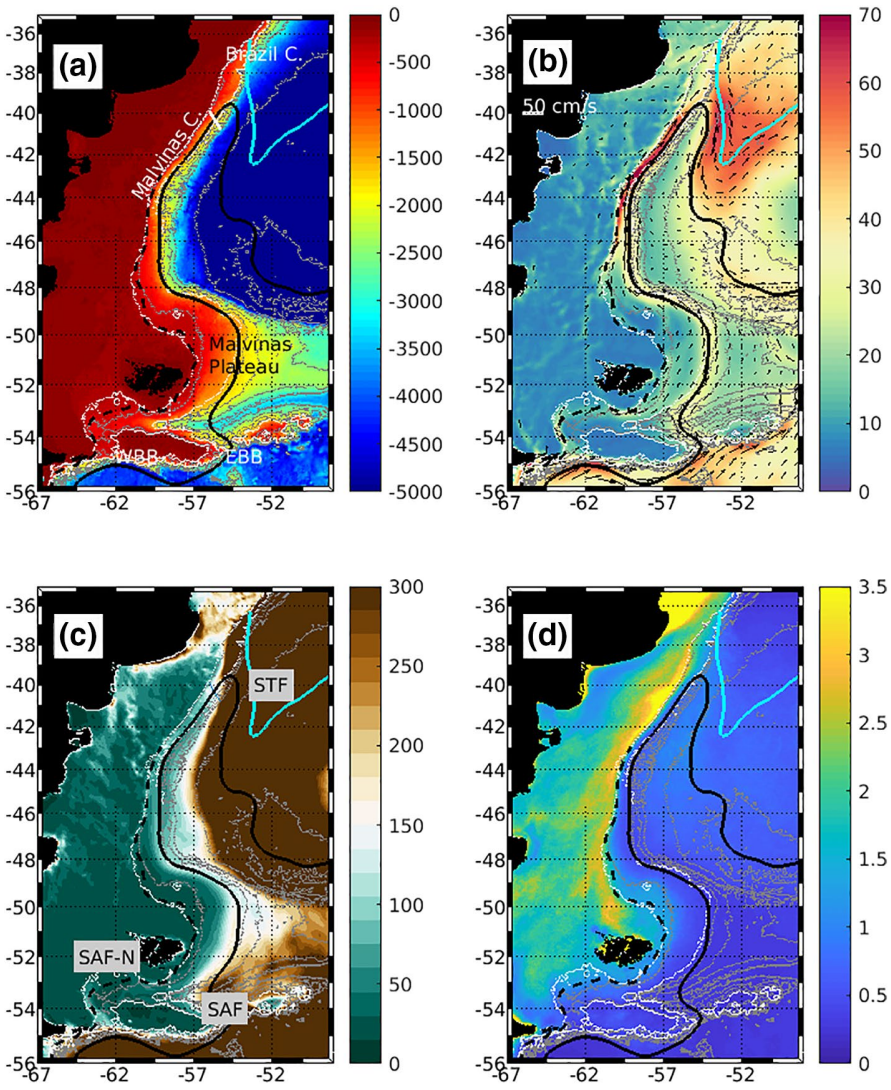

Figure 1. (a) Bathymetry of the Southwest Atlantic (in m) from ETOPO6.2 (update from Smith and Sandwell [1994]). Three passages connecting the Argentine Basin to the Drake Passage are indicated: West of Burwood Bank (WBB), East of Burwood Bank (EBB), and Shag Rocks Passage (SRP). White isolines correspond to 300- and 1,500-m isobaths. (b) Mean surface velocities (arrows) and mean surface velocity intensities in cm/s (color) from GLORYS12 over the period 1993–2017. (c) Mean surface eddy kinetic energy from GLORYS12 over the period 1993–2017 in $(cm/s)^2$. (d) Mean values of surface chlorophyll-a concentration (in mg/m^3) derived from MODIS satellite data. Note the long continuous high values (>2.5 mg/m^3) at the shelf break (2002–2017). The mean locations of the northern branch of the Subantarctic Front (SAF-N) is represented with a black dashed line, that of the main SAF with a continuous black line (defined as in Barré et al. [2011]), and that of the Brazil Current front (BCF) with a cyan line (defined as in Ferrari et al. [2017]). The white segment at 41°S in (a) marks the sites of successive mooring deployments.

The MC carries cold, nutrient-rich subantarctic waters that play a key role in the development of the biological activity in this region: massive phytoplankton blooms are observed over the Patagonian shelf (Romero et al., 2006; Valla & Piola, 2015). The inner portion of the Patagonian continental shelf break presents chlorophyll concentrations peaking at 2.5–3.0 mg/m^3 (Figure 1d). TW disturbs the upper thermocline and could enhance the fluxes of nutrients to the shelf break.

High-resolution ocean models (1/12°) that assimilate in situ observations and along-track satellite altimetry, such as the Mercator Ocean physical reanalysis at 1/12°, could provide some insights on TW propagating along the Patagonian shelf break. Previous works have assessed the performance of this reanalysis in the

MC system (Artana et al., 2018a, 2019). Here, we further evaluate the spectral content of the reanalysis SLAs and velocities on the slope compared to observations. As a result of this comparison, we use the reanalysis tridimensional fields to examine TWs at the shelf break and in the core of the MC at periods larger than 10 days. The theory from Brink (1982), which idealizes TW as a sum of modes whose spatial structure, phase, and group velocities depend upon the cross-shore topography and stratification, provided guidance.

This paper is organized as follows. We first compare possible signatures of TW in observations and the Mercator Ocean reanalysis. In Section 3, we explore fast waves detected at the shelf break and interpret them using the idealized model from Brink and Chapman (1987). Slower velocity variations in the core of the MC above the 1,500-m isobath are examined in Section 4. Section 5 discusses the results and concludes.

2. Model and Data: Possible Signatures of Trapped Waves

2.1. Mercator Ocean Reanalysis

The high-resolution (1/12°) global Mercator Ocean reanalysis (hereafter GLORYS12) has been developed in the framework of the Copernicus Marine Environment Monitoring Service (CMEMS, http://marine.copernicus.eu/)and extends over a period of 25 years (1993–2017). This reanalysis is based on the current real-time global forecasting CMEMS system (Lellouche et al., 2018) with a few changes in atmospheric forcing, assimilated data, and observation errors. Nucleus of European Modeling of the Ocean platform is the dynamical core of the physical model. The ocean surface is forced by the global ERA-Interim atmospheric reanalysis from the European Center for Medium-Range Weather Forecasts. The model assimilates observations using a reduced-order Kalman filter with a 3-D multivariate modal decomposition of the background error and a 7-day assimilation cycle (Lellouche et al., 2018). The model assimilates jointly along track satellite altimetric data from CMEMS (Pujol et al., 2016), AVHRR satellite sea surface temperature from NOAA, Ifremer/CERSAT Sea-Ice Concentration, and in situ temperature and salinity vertical profiles from the latest CORA in situ databases (Cabanes et al., 2013; Szekely et al., 2016). Artana et al. (2018a) evaluated the performance of the reanalysis GLORYS12 over the MC and found a good agreement with observations. Further comparisons on the continental slope between the model and observations are shown in the following sections.

2.2. GLORYS12 and Satellite Altimetry Spectral Contents Along the Slope

We used Data Unification and Altimeter Combination System (DUACS) delayed-time altimeter gridded (1/4° regular grid) daily product (Pujol et al., 2016; Taburet et al., 2019) available at http://marine.copernicus.eu/. This product results from an optimal interpolation in space and time, combining measurements from different altimeters, and its effective resolution is about 20 days in time and 200 km in space (e.g., Archer et al., 2020).

GLORYS12 produces somewhat larger EKE values on the Patagonian slope than satellite altimetry (Artana et al., 2018a, their Figures 1b and 1d). We built a time series of averaged SLA between the 300- and 1,700-m isobaths all along the slope. Their spectra are shown as a function of latitude for the DUACS product (Figure 2a) and GLORYS12 (Figure 2b). The spectra display striking similarities with significant energy peaks at distinct periods between 10 and 500 days. The annual cycle dominates the spectra. The continuum of energy observed in the spectra to the north of 40°S reflects the outstanding variability at the Brazil-Malvinas Confluence. Some periods such as 20, 60–70, and 100 days exhibited energy all along the slope. Those periods could be associated with waves propagating between the 300- and 1,700-m isobaths. There was no energy at periods shorter than 5 days in either spectrum, and as expected GLORYS12 displayed more energy than altimetry at periods between 5 and 14 days (Figure 2c).

Indeed, satellite gridded data do not capture variations at periods smaller than 14 days.

2.3. GLORYS12 and Mooring Data on the Slope at 41°S

Current-meter moorings have been deployed in 1993–1995, 2001–2003, and 2014–2015 across the continental slope at 41°S near the Confluence (Ferrari et al., 2017; Spadone & Provost, 2009; Vivier & Provost, 1999).

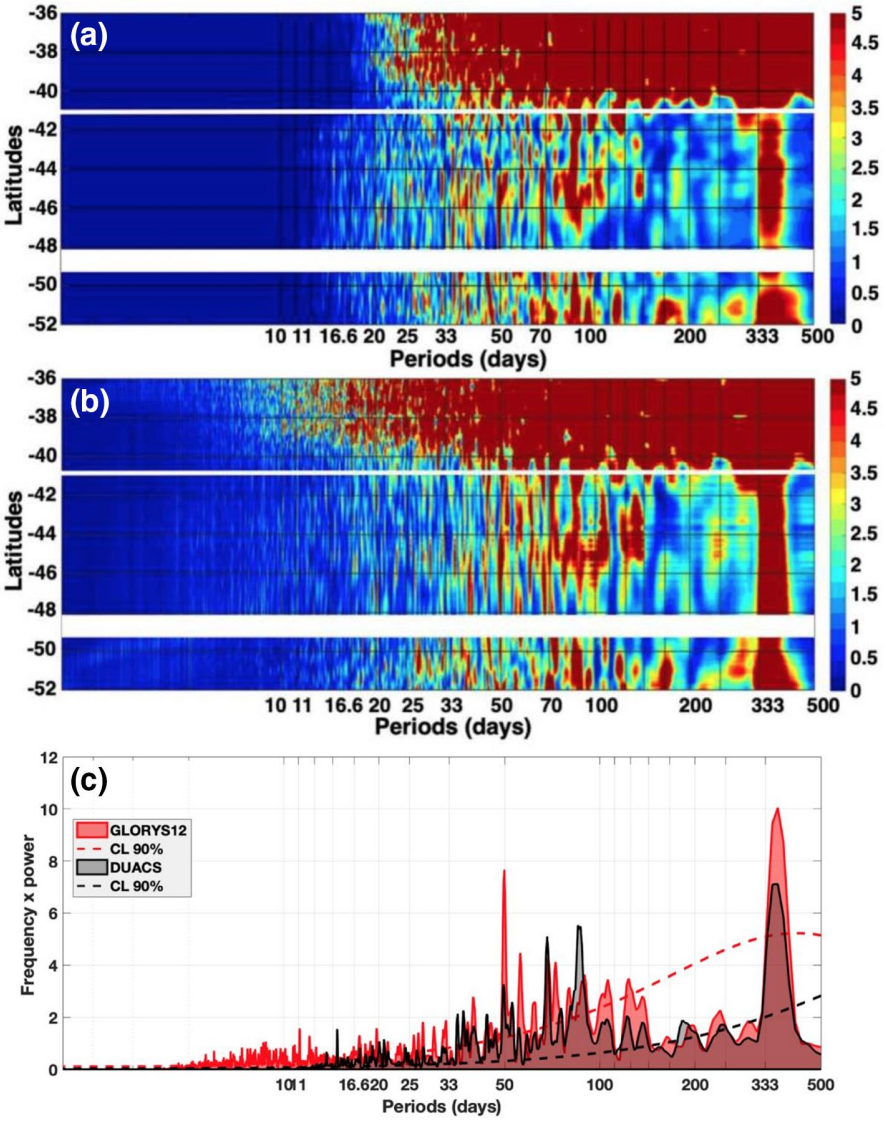

Figure 2. Sea level anomaly (SLA) variance preserving spectra as a function of latitude (SLA was averaged in a longitude band between the 300- and 1,700-m isobaths) (a) from satellite altimetry Data Unification and Altimeter Combination System (DUACS) product and (b) from Mercator reanalysis GLORYS12. White lines at 41°S correspond to the location of the moorings. The gap between 50.5°S and 48°S corresponds to a region with zonal isobaths (Figure 1a). Color bar in cm^2. (c) Sea level anomaly variance preserving spectra averaged between 48°S and 43°S for GLORYS12 (red) and for satellite altimetry DUACS product (black). Dashed lines correspond to a 90% confidence limit.

As GLORYS12 showed no significant energy at periods shorter than 5 days, the mooring data were 5-day low-pass filtered for comparison. In spite of significant differences from one deployment to the other, means and variance ellipses showed consistent patterns with a mean flow toward the North East and ellipses stretched in the direction of the mean flow above the slope, and weaker mean flow and more round ellipses offshore (Figure 3; 1993–1995 in black, 2001–2003 in blue, 2014–2015 in green, and GLORYS12 in red). GLORYS12 accurately reproduced the general patterns and the differences between mooring deployments with, in particular, large variance ellipses during the last deployment due to the Confluence position being exceptionally south from May to September 2015 (Artana et al., 2019; Paniagua et al., 2018). The intensity and direction of the mean flow and the variance ellipses from GLORYS12 were in good agreement with the observations in this highly energetic and complex region (Figure 3).

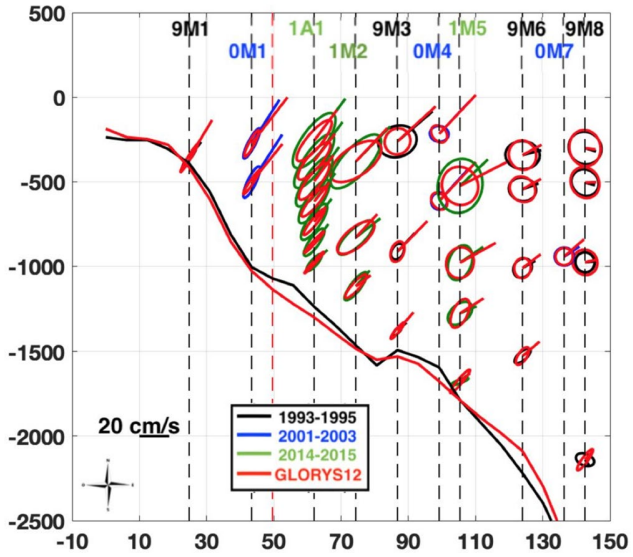

Figure 3. Mean flow and variance ellipses for each current meter at 41°S from 1993 to 1995 in black, 2001 to 2003 in blue, 2014 to 2015 in green, and from GLORYS12 in red; all-time series have been smoothed with a 5-day low-pass filter. 0M1 and 1A1 are both from the same location (red dashed line). They are displaced on the figure for sake of visibility. Black line is the bathymetry from ETOPO6.2 and red line is the model bathymetry.

2.4. Statistics Over 25 Years: Evidence of Different Propagation Velocities Above the 300- and 1,500-m Isobaths in GLORYS12

We examined the propagation of along-slope velocity anomalies at 100 m depth following the 300-m isobath of the Patagonian slope (Figure 4). A 110-day high-pass filter was applied to remove the seasonal cycle. The filtered velocities along the 300-m isobath (colored points in Figure 4a) were correlated with those at locations Φ (60.5°W, 53.5°S), Ω (60.5°W, 47°S), and Ψ (56.8°W, 41°S) (black points in Figure 4a). Lagged correlations are shown as a function of distance from Φ (53.5°S) along the slope (lagged correlations with Φ in Figure 4b, Ω in Figure 4c, and Ψ in Figure 4d). For each point along the isobath, we selected the lag presenting the maximum correlation and applied a linear fit (dashed lines in Figure 4) to estimate propagation velocities. Correlations with Φ were maximum at lag 0 to the south of 200 km ($r > 0.5$) and between 600 and 1,050 km ($0.3 < r < 0.5$, pink dots in Figure 4b), indicating simultaneous signals. In addition, two high-correlation patterns (dashed lines in Figure 4b) suggested northward propagations from Φ and Ω with a phase speed ranging between 140 and 300 cm/s. The correlations associated with these propagating signals diminished with distance and remained significant until 38°S (2,100 km). These features were consistently found in the lagged correlations with point Ω (Figure 4c): maximum correlations at lag 0 nearby Ω and Φ ($r > 0.5$), and two patterns suggesting the same propagating signals at similar phase speeds (dashed lines in Figure 4c). Lagged correlations with Ψ (Figure 4d) showed a slower (phase speed between 20 and 30 cm/s) and more localized propagation between

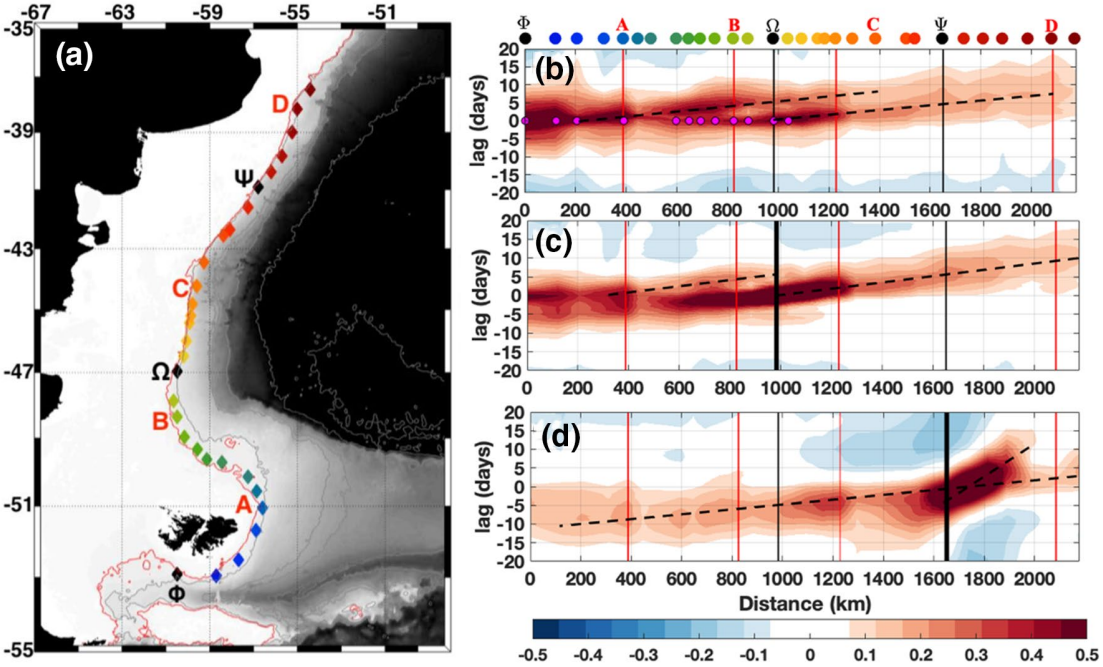

Figure 4. Lagged correlation diagrams of 110-day high-pass filtered along-slope velocities at 100 m depth above the 300-m isobath. (a) Point along the slope used for the correlations with locations Φ (53.5°S), Ω (47°S), and Ψ (41°S). Red line is the 300-m isobath. Background is bathymetry (in m). (b) Along-slope velocity correlations with Φ. *x*-axis is the along-isobath distance from 53.5°S, *y*-axis is the lag in days. Pink dots indicate locations where maximum correlations were obtained at lag 0 day. (c) Along-slope velocity correlations with Ω (axes as in b). (d) Along-slope velocity correlations with Ψ (axes as in b). Only significant correlations (above 90% confidence limit) are colored. Dashed lines correspond to a linear fit of maximum correlations. The slopes provide estimates of the phase velocities (b) 250 ± 50 and 167 ± 15 cm/s, (c) 156 ± 15 cm/s for both dashed segments, (d) 35 ± 3 and 210 ± 50 cm/s.

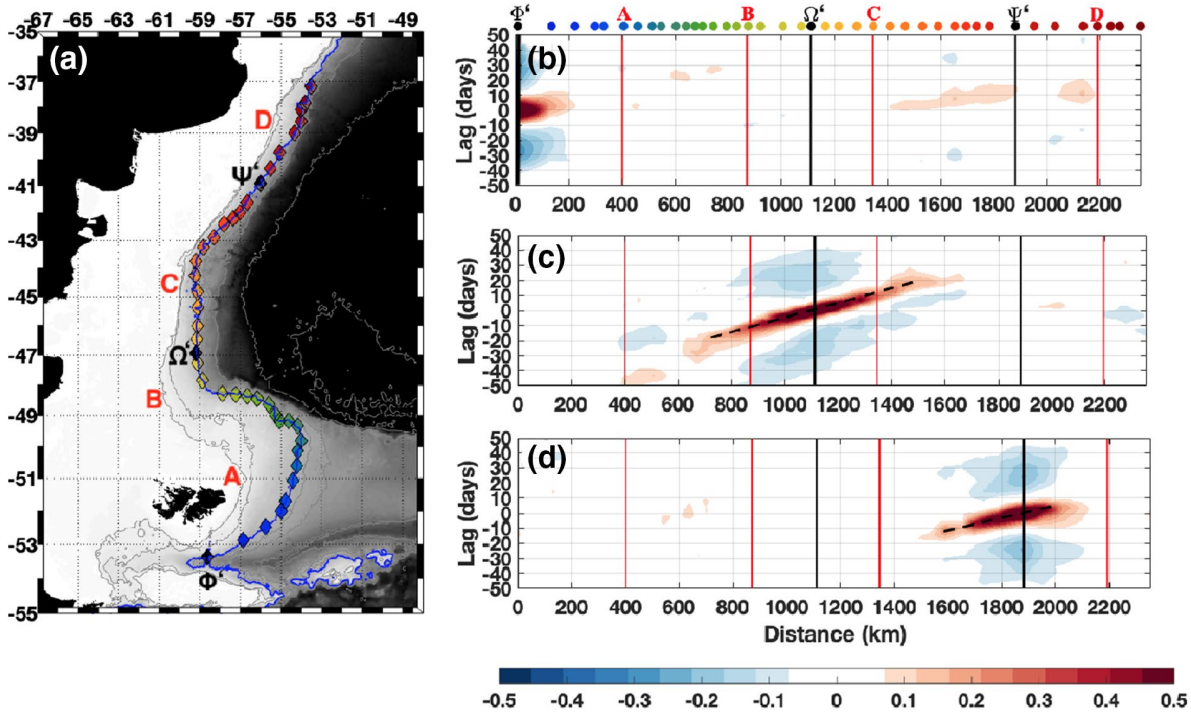

Figure 5. (a) Points along the slope used for the correlations with location Φ′ (58.6°W, 53.35°S), Ω' (59.2°W, 47°S), and Ψ′ (56°W, 41°S), blue line is the 1,500 isobath. Background is bathymetry (in m). (b–d) Lagged correlation diagrams of 110-day high-pass filtered along-slope velocities at 100 m depth over isobath 1,500 m (in the core of the MC) considering point Φ′ (b), Ω' (c), and Ψ′ (d). *x*-axis is the distance along the isobath and *y*-axis is the lag in days. Phase velocities estimated as in Figure 4: (c) 23 ± 2 cm/s and (d) 30 ± 2 cm/s.

1,600 and 2,000 km (43°S and 40°S, with correlations exceeding 0.5) superposed to the faster propagation signals associated with small correlations of 0.25.

Lagged correlations between along-slope velocities above the 1,500-m isobath, in the core of the MC, showed more localized features around Φ′ (58.6°W, 53.35°S), Ω' (59.2°W, 47°S), and Ψ′ (56°W, 41°S) (Figure 5). Correlations at Φ′ ($r > 0.5$) suggested no propagation and a period about 40 days (Figure 5b). The correlation pattern with Ω' indicated propagating signals (with $r > 0.3$) with a phase speed of 20 cm/s with periods of about 50 days extending from 800 to km 1,600 km (Figure 5c). Correlation patterns with Ψ′ suggested propagating signals with a phase speed of about 25 cm/s and a period of 50 days between 1,600 and 2,100 km (Figure 5d). This propagating feature was reminiscent of the one observed at 41°S over the 300-m isobath in Figure 4d.

Statistics over 25 years of GLORYS12 revealed three types of signals: signals merely in phase to the south of 47°S at the shelf break, fast propagating signals with phase speed ranging from 140 to 300 cm/s all along the shelf break, and slower signals in the core of the MC with propagation velocities ranging from 10 to 30 cm/s.

3. Fast Signals at the Shelf Break

3.1. Coherent Forced Response to Wind Pulses Over the 25 Years

The Southwest Atlantic undergoes strong westerlies (Figure 6a) with large wind stress mean values (>0.2 Pa) to the south of 52°S and in the southwestern portion of the deep Argentine Basin. The intensity of the mean wind stress decreases toward the north along the Patagonian slope to 0.05 Pa at 38°S. The zonal wind stress shows a maximum variability (Figure 6b) near Φ.

The zonal wind stress along the slope was highly correlated ($r > 0.8$) with the zonal wind stress at 53.5°S (Φ) up to 47°S (Ω) (not shown). Lagged correlations of the along-slope velocities over the 300-m isobath with

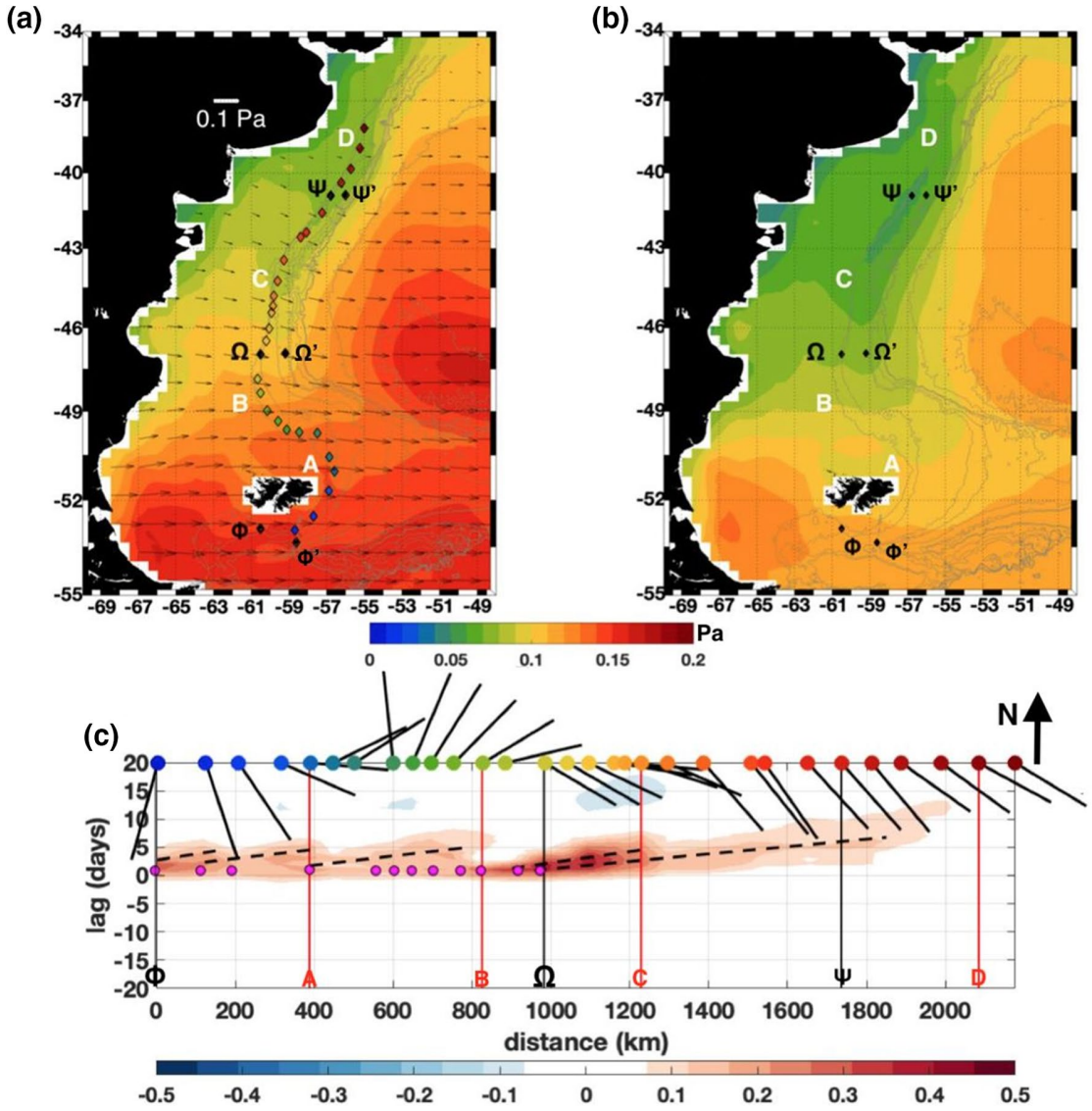

Figure 6. (a) Mean wind stress (1993–2017) from ERA-interim, arrows represent direction and background is intensity (all in Pa). (b) Standard deviation of the zonal wind stress. (c) Lagged correlations between the zonal wind stress at Φ (53°S) and ocean along-slope velocities at 100 m above 300-m isobath over the 25 years of GLORYS12 reanalysis. Only significant correlations are shown. Lagged correlations above the 1,500-m isobath are not significant (not shown). *x*-axis is the distance from Φ along the isobath, *y*-axis is the lag in days, and vertical lines correspond to location of points A, B, C, D, Φ, Ω, and Ψ shown in Figures 6a and 6b. Pink dots indicate locations where correlations with the wind were maximum at lag 1 day. Phase velocity was estimated as in Figure 4: between 108 and 241 cm/s. Stick plot represents the bathymetry gradient along the slope at each colored dot shown in (a). Black arrow represents the north.

the zonal wind stress at Φ (Figure 6c) showed patterns reminiscent of those observed in Figure 4b. Interestingly, correlations at lag 1 day peaked at the distinct locations indicated with pink dots in Figure 6c. These locations showed in-phase along-slope velocity variations (Figure 4b), suggesting a wind-forced quasi-instantaneous response (compare pink dots in Figures 4b and 6c). The wind also triggered the fast propagating signals departing from Φ and Ω (previously identified in Figures 4b and 4c). Other wave departures were observed between 0 and 1,000 km: at 200, 400, 800, and 1,000 km (Figure 6c). They corresponded to changes in direction of the bathymetry gradient (indicated with stick plot in Figure 6c).

In contrast, correlations of the zonal wind stress at Φ' and Ω' with the along-slope velocities over the 1,500-m isobath (not shown) were not significant suggesting that non-propagating signals and the slow propagations were not forced by the local wind.

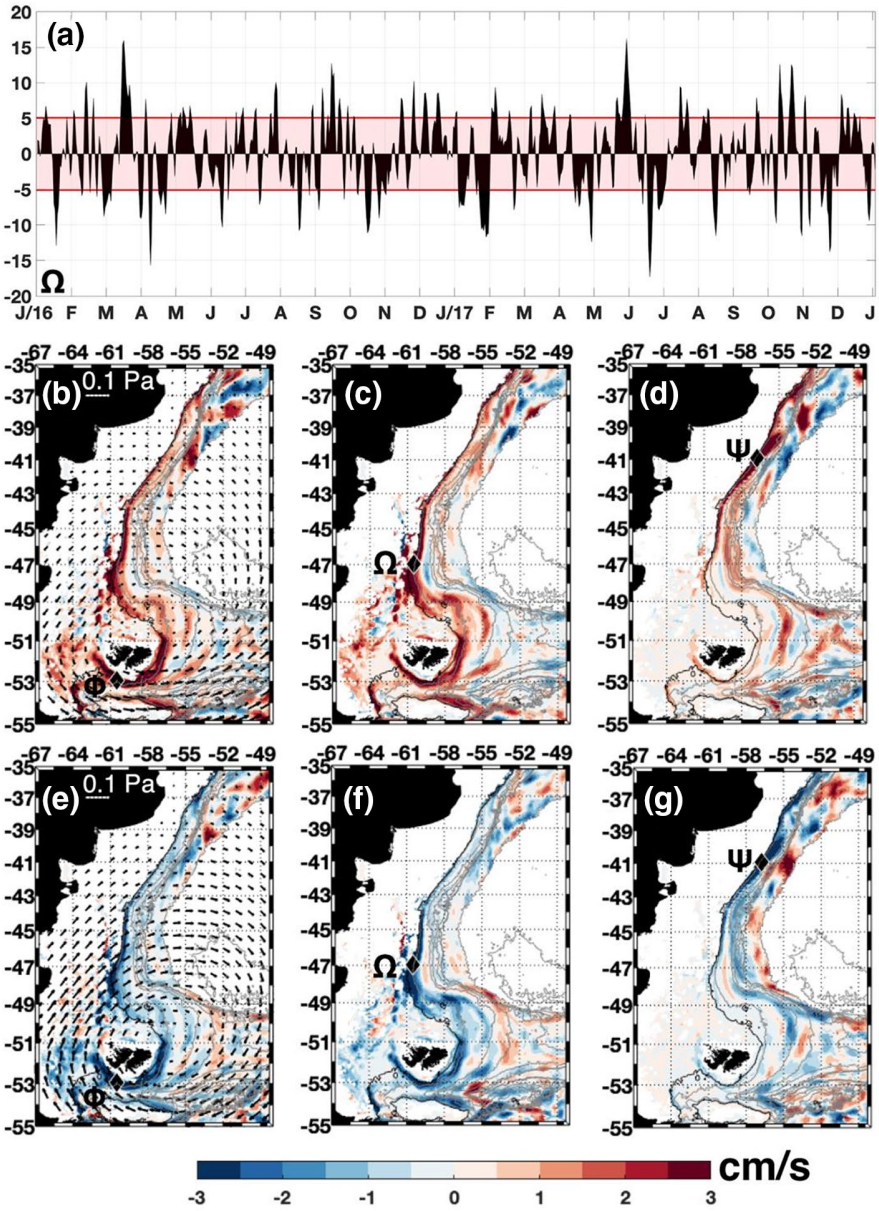

Figure 7. (a) Time series of along-slope 110-day high-pass filtered velocity at 100 m above the 300- m isobath at Ω for 2 years (2016–2017 as an example for sake of clarity). Units are in cm/s and shaded area corresponds to the standard deviation. (b–d) Along-slope velocity composites at 100 m. They were built considering the dates with velocities exceeding the standard deviation at Φ, Ω, and Ψ, respectively (positive phase). The arrows on (b) and (e) indicate the corresponding wind stress anomaly composite. (e–g) Same as (b–d) for the negative phase.

Along-slope velocity composites shown in Figures 7b–7g were obtained from averaging maps for the dates when the amplitude of the along slope velocity filtered time series at Φ (Ω and Ψ, respectively) exceeded one standard deviation. (Figure 7a). This criterion selected about 1,350 (1,400) days for the positive (negative) events for each time series.

The composite maps of positive events (Figures 7b–7d) have similar spatial structures with an opposite sign to the negative ones consistent with wave dynamics.

The wind stress anomalies associated with the composites exhibited a well-defined anticyclonic/cyclonic structure centered around the Malvinas Islands with zonal wind anomalies at Φ (Figures 7b and 7e). The

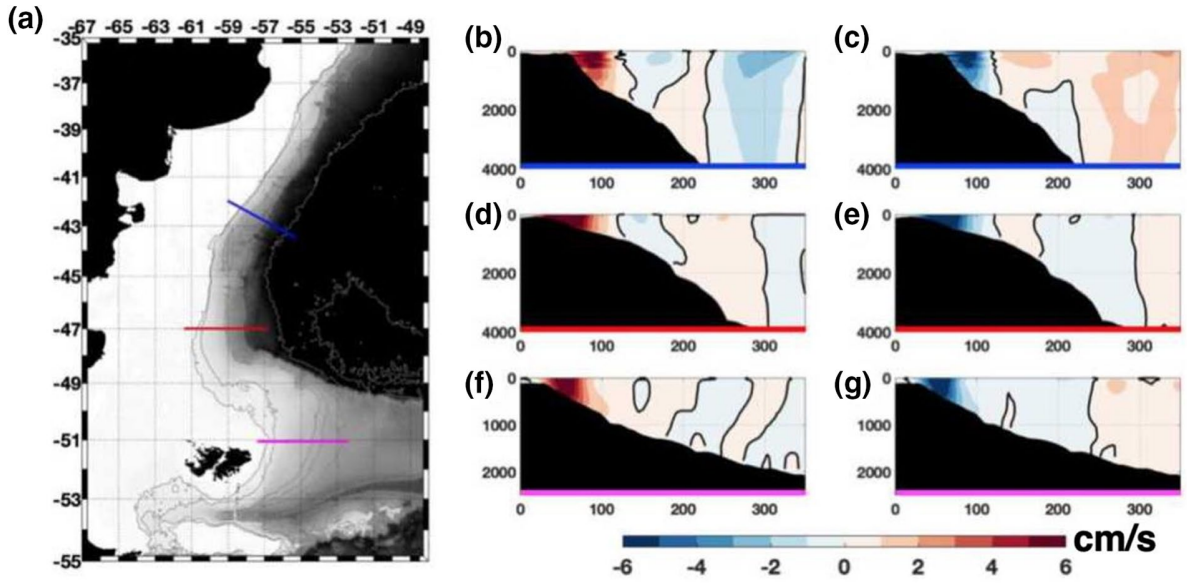

Figure 8. (a) Location of the three sections examined in the appendix using Brink and Chapman's model. GLORYS12 velocity composites (in cm/s) were produced along the sections (b–g) for comparison with theory. They were built averaging fields at dates when filtered velocities at 100 m over the 300-m isobath exceeded the standard deviation. (b and c) Composite of filtered along-slope velocity along the blue section for positive (b) and negative (c) phases for the dates when the filtered velocity at 100 m over the 300-m isobath exceeds the standard deviation. (d and e) Composite of along-slope filtered velocity along the red section for positive (d) and negative (e) phases for the dates when the filtered velocity at 100 m over the 300-m isobath exceeds the standard deviation. (f–g) Composite of along-slope filtered velocity along the magenta section for positive (f) and negative (g) phases for the dates when the filtered velocity at 100 m over the 300-m isobath exceeds the standard deviation.

wave departure locations identified in Figure 6c corresponded to the locations of the largest along-slope velocity anomalies (Figures 7b and 7e). A simultaneous wave departure was seen on the western side of East of Burwood Bank (EBB) Passage. As expected, the composite maps built from Ω time series are similar to those built from Φ. Composite maps exhibit complex cross-slope structure with changing sign velocities (Figures 7b–7g). The composite built from Ψ showed a weak velocity signal all along the shelf break intensified near Ψ, plus a signal over the 1,500-m isobath between 47°S and Ψ (Figures 7d and 7g). These observations were consistent with the superposition of two propagating patterns as seen in Figures 4d and 4a, fast one along the shelf break and a slower one offshore above the 1,500-m isobath.

3.2. Idealized Ocean Response: Cross-Slope Modal Structure

We used the linear theory of Brink and Chapman (1987), which provides the modal structures of sub-inertial frequency waves on a sloping bottom under idealized hypotheses (see Appendix). In spite of idealized assumptions such as a straight coastline with uniform shelf bathymetry, which is not the case of the Patagonian shelf break, the analysis provided some insight in the modal structure of TW. We computed cross-slope modal structures of TW along three sections across the Patagonian slope: the first one at 51°S where the slope is gentle and the bottom relatively shallow (2,000 m), the second one at 47°S where the upper slope is steeper, and the last one at 42°S showing an abrupt bathymetry (Figure 8). The four gravest modes and their dispersion curves for the three sections are shown in Appendix. Along the cross-slope sections, the modes are nearly barotropic, trapped at the shelf break and bottom intensified on the lower slope (see Appendix).

Along the three sections, we built velocity composites corresponding to the dates of significant peaks (above the standard deviation) in the along-slope velocities at 100 m above the 300-m isobath (Figure 8). The three velocity composites featured patterns reminiscent of theoretical modes 2, 3, and 4 (see Appendix). Modes 2, 3, and 4 dispersion curves provided theoretical phase velocities matching the observed one (about 140–300 cm/s) for waves with periods ranging between 5 and 110 days and wavelengths varying from 500 to 2,500 km. The theoretical mode is defined within a multiplicative factor (Brink, 1989); velocity maxima in the composite and the theoretical mode suggested a scaling factor of 6×10^8. Applying the factor scale to

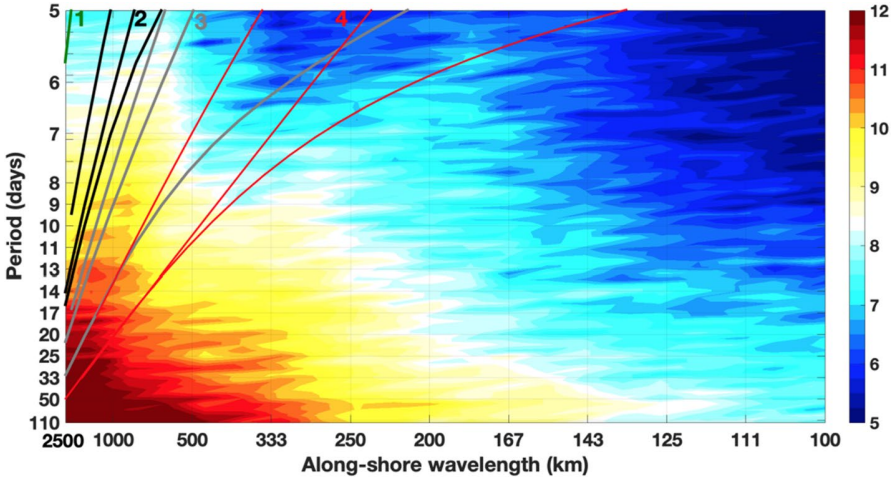

Figure 9. Frequency-wavenumber spectrum of along-slope velocities at 100 m depth above the 300 m isobath. Color bar units: velocity psd. Lines correspond to the dispersion relation for theoretical Shelf Break Trapped Wave (SBTW) modes at 51°S, 47°S, and 42°S (Figure A4 in Appendix) (green lines: mode 1; black lines: mode 2; gray lines: mode 3; red lines: mode 4).

the theoretical mode led to across-slope velocities of the order of 1 cm/s, consistent with the across-slope composites (not shown) and to vertical velocity estimates of the order of 5–20 m/day.

3.3. Period-Wavelength Spectrum of Along-Slope Velocities at 100 m Above the 300-m Isobath

The period-wavelength spectrum of along-slope velocities at 100 m above the 300-m isobath showed energy along patterns consistent with theoretical dispersion relations associated with shelf-break TW of modes 2, 3, and 4 propagating northward (Figure 9). The theoretical dispersion curves computed for several latitudes with different bottom steepness and mean flows (black and gray lines in Figure 9) show that, although the hypothesis of an infinite constant slope is far from being satisfied, the theory provides insight into the dynamics.

We filtered Shelf Break Trapped Wave signals in three period bands (10–40, 30–90, and 80–110 days) and built the corresponding composites (not shown). We obtained similar patterns to those in Figure 7 with wavelengths increasing with periods as expected from theory.

3.4. Impact of the Shelf-Break Waves on the Onshore Jet

South of 42°S, the MC is organized in two relatively stable jets (Piola et al., 2013). The main jet straddles the 1,500-m isobath and corresponds to the main SAF and the largest current core, while the onshore jet associated with the northern branch of the SAF follows the 300-m isobath from West of Burwood Bank (WBB) at 55°S-44°S (Figure 1b). We investigated the potential relation between the fast propagating waves and the onshore jet. The positive phase of the wave corresponded to an intensification of the onshore jet along the shelf break from 55°S to 47°S (Figure 10a). Local along-slope velocity maxima at the shelf break were associated with the regions of wave departure (identified in Figure 6c). The onshore jet split into two branches at 51°S, where the 300- and 500-m isobaths diverge. The two branches merged in a single onshore strong jet at 47°S, where the two isobaths converge (Figure 10a). At 47°S, the onshore jet reached 40 cm/s near the surface (Figure 10b). In contrast, during the negative phase, the onshore jet core velocity diminishes (Figures 10c and 10d).

3.5. Sea Surface Anomalies Accompanying Fast Shelf-Break Waves

The GLORYS12 SLA composite maps built from velocity time series at Φ show a positive/negative signal (>4 cm) over the continental shelf consistent with the anticyclonic/cyclonic wind anomaly pattern creating convergence/divergence associated with the positive and negative phases of the wave (Figures 11b and 11e). Stronger composite SLA patterns were observed on the shelf in the composite for Ω (Figures 11c and 11f).

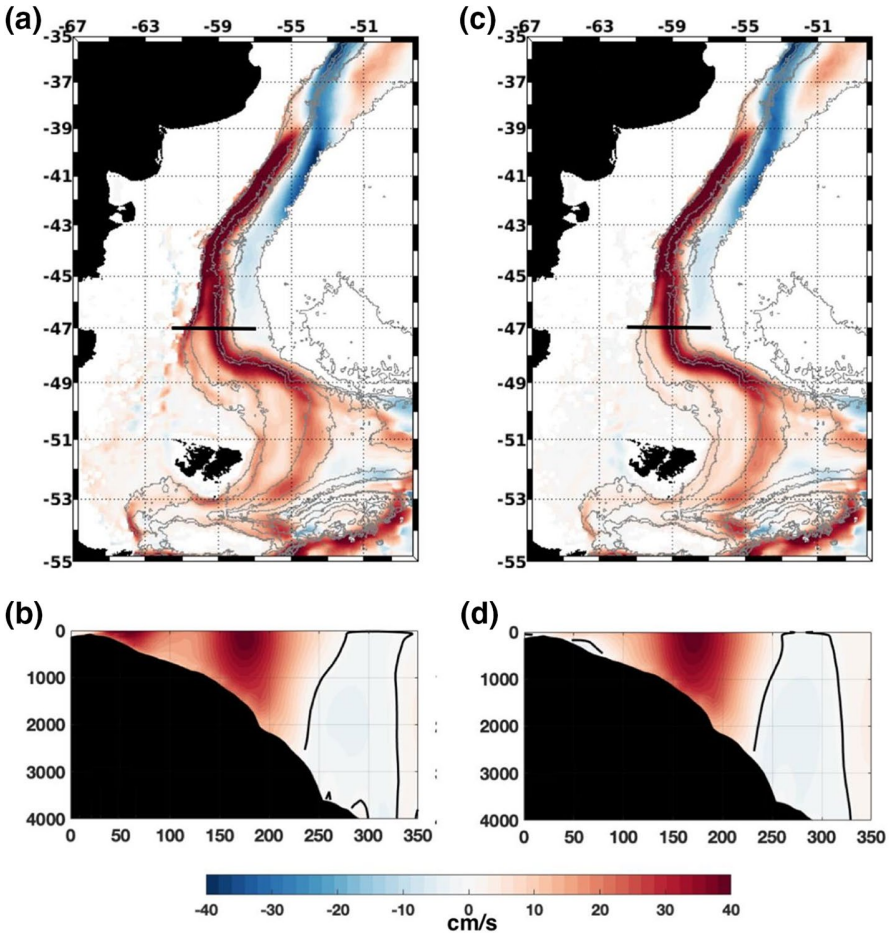

Figure 10. (a) Along-slope velocities corresponding to the positive phase of the fast waves at 47°S (mean flow plus twice the composite of along-slope velocity anomalies from Figure 7b). The 47°S vertical section is shown (b). (b) Along-slope velocity at 47°S section corresponding to (a). (c) Same (a) for the negative phase. (d) Along-slope velocity at 47°S section corresponding to (c). Color bar in cm/s.

All along the shelf break, composite SLA values were small of the order of 2 cm; however, synoptic SLA values at Ω could reach peak values larger than 5 cm lasting less than 10 days (Figure 11a). The SLA composites were consistent with the modes (2–4) predicted by Brink linear theory (Figure A5). In contrast, SLA composites for Ψ (Figures 11d and 11g) showed small amplitudes on the continental shelf (less than 2.5 cm) and a somewhat stronger mesoscale structure of opposite sign (3.5 cm) close to 42°S centered slightly offshore, reminiscent of slow propagating signals observed in Figure 4d.

4. Velocity Variations in the Core of the Malvinas Current

Lagged correlations of along-slope velocity anomalies at 100 m for each filter period are shown in Figure 13. The diagrams featured correlations decreasing with distance from Ω' suggesting continuous damping of the propagating signals along the slope (Figures 13a and 13c). The characteristic time of damping (amplitude reduced by half) was about 10 days for the 10–40-day band-passed signals, 20 days for the 30–90-day band-passed signals, and about 100 days for the larger period signals. The 10–40 day band-pass filter selected waves with a period of about 20 days and a phase speed of 25 ± 1 cm/s between 700 and 1,400 km (Figure 13a). The 30–90-day band-pass filter provided waves with a period of about 60 days and a phase speed of 20 ± 2 cm/s between 600 km (49°S) and 1,500 km (43°S) (Figure 13b). The 80–110-day band-pass filter delivered waves

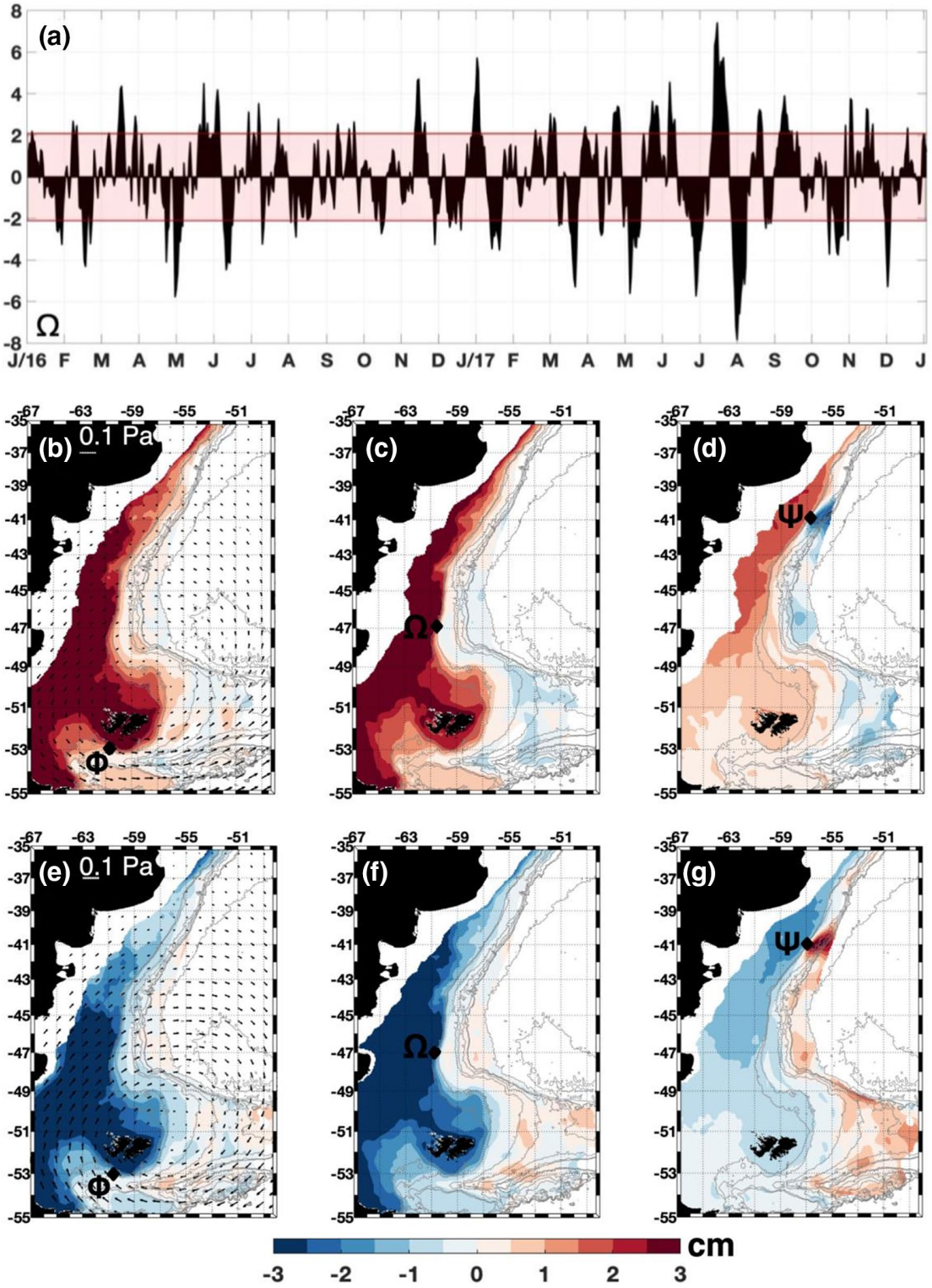

Figure 11. (a) Time series of GLORYS12 sea level anomaly (SLA) above the 300- m isobath at Ω (47°S). (b–g) Composite of model SLAs at the dates of the velocity composites shown in Figure 7. Units are in cm. Only significant values are shown. (b–d) SLA for the positive phase at Φ (53.5°S), Ω (47°S), and Ψ (41°S). (e–g) SLA for the negative phase. The arrows on (a) and (b) indicate the corresponding composite of the wind stress anomaly.

with a period of about 100 days and a phase speed of 14 ± 1 cm/s between 300 and 1,500 km (Figure 13c). The correlation patterns for the three band-passed velocities changed between 1,400 and 1,800 km (between point C and Ψ′, Figure 5a), at a location where the shelf break abruptly changes orientation (from north to northeast) and bottom slope steepens (Figures 13a–13c). There, phase velocities slightly increased. Beyond 2,000 km, lagged correlations indicated southwestward propagating patterns. We interpreted those as signals associated with the Brazil-Malvinas Confluence. Between 1,600 and 2,000 km, the lagged composite diagrams suggested interferences between the northward propagating waves and signals from the Confluence.

Composite maps (Figure 14) were built selecting the days with a band-passed velocity amplitude at Ω' larger than the band-pass velocity standard deviation (Figure 12a): 1,429, 1,461, and 1,415 days were considered for the 20-, 60-, and 100-day period waves, respectively. The 20-, 60-, and 100-day period waves had along-slope wavelengths of about 450, 1,000, and 1,200 km, respectively (Figure 13), and featured an across-slope structure of mode with narrow cores of about 25, 40, and 50 km width, respectively (Figures 14a–14e; 14f–14j; 14k–14o). Upstream 49°S, lagged composites suggested two paths, one from the northern Drake Passage and one from the deep argentine basin along the Malvinas Escarpment (Figure 1a). The two contributions combined around 49°S (around 600 km in Figures 13a–13c) where the distance between the 1,500-m isobath from the Plateau and the 2,800-m isobath from the Escarpment reduces to 50 km (Figures 14a–14e; 14f–14j; 14k–14o). Two deep passages in the North Scotia Ridge connect the Drake Passage to the Argentine Basin: EBB and Shag Rock Passage (SRP) (Figure 1a). The velocity anomaly in the composite maps over the Malvinas Plateau showed patterns suggesting that waves from Drake Passage may proceed through the two passages. This was in agreement with observations showing the SAF crossing the North Scotia Ridge through either EBB or SRP (Artana et al., 2016).

North of 43°S, the signal in the composite maps for the 20- and 60-day waves weakened and stretched along the shelf break, while the signals in the composite maps of the 100-day waves became patchy, an indication of interferences with signals coming from the Confluence.

The 60- and 100-day period waves were associated with consistent elongated SLA anomalies of 2–3 cm amplitude in the composites (Figures 15b and 15c), which clearly showed the two pathways from the Malvinas Plateau and Escarpment. Signals in the SLA composite for the 20-day period waves were blurry (Figure 15a) as these waves had shorter wavelengths, smaller widths, and were more rapidly damped in the model. In contrast, synoptic values of SLA could reach 7 cm for the 20-day period waves, 5 cm for the 60-day period waves, and 2 cm for the 100-day period waves (Figure 12b).

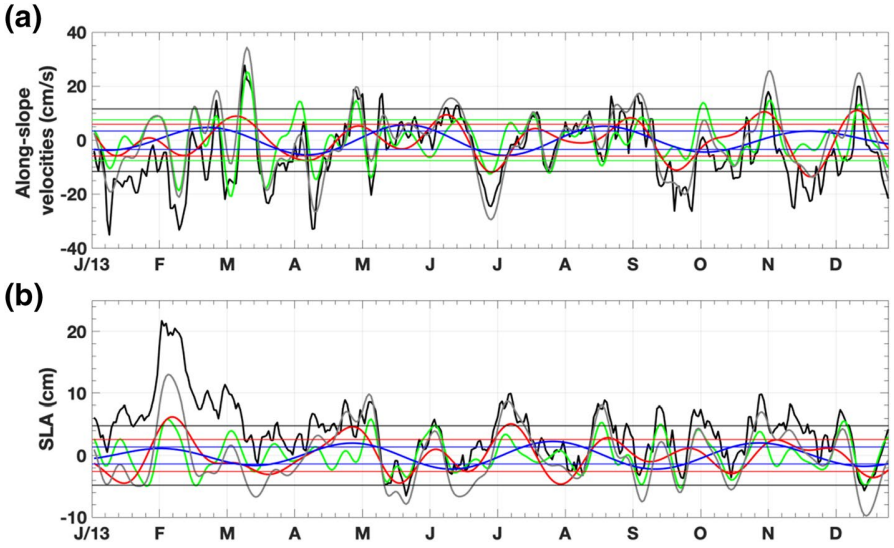

Figure 12. GLORYS12 along-slope velocity anomalies (a) and sea level anomalies (b) time series (in black) for the year 2013 above the 1,500-m isobath at Ω (47°S) and filtered time series with different band-pass filters: 10–40 days (green), 30–90 days (red), and 80–110 days (blue). The three filtered time series are tentatively summed (gray curve).

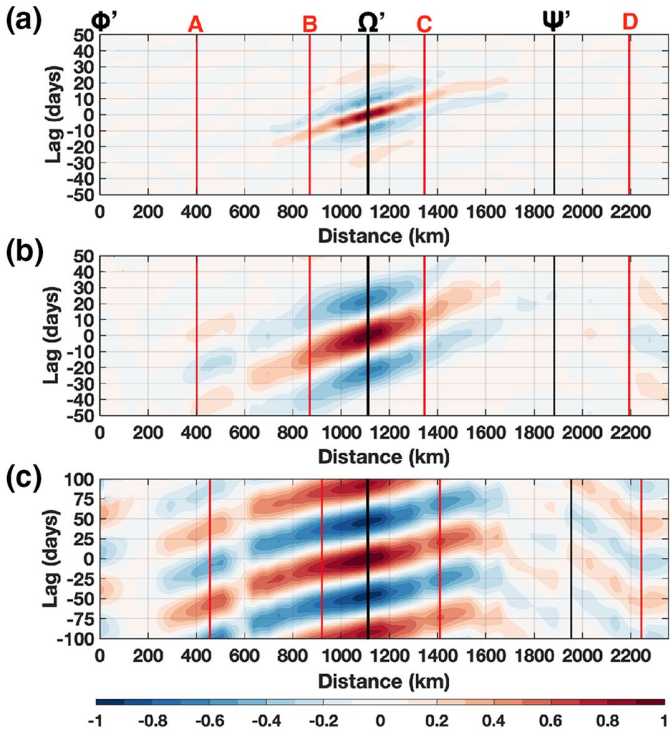

Figure 13. (a) Lagged correlations of 10–40 day band-pass filtered along-slope velocities with the velocities at Ω (47°S), *y*-axis is the lag in days, *x*-axis is the distance along the slope above 1,500 m isobath. (b) Lagged correlations of 30–90-day band-pass filtered along-slope velocities with the velocities at Ω (47°S), *y*-axis is the lag in days, *x*-axis is the distance along the slope. (c) Lagged correlations of 80–110-day band-pass filtered along-slope velocities with the velocities at Ω (47°S), *y*-axis is the lag in days, *x*-axis is the distance along the slope. Phase velocities estimated as in Figure 4: (a) 25 ± 1, (b) 20 ± 1, and (c) 14 ± 1 cm/s.

5. Summary and Discussion

We used GLORYS12 to examine velocity variations at periods larger than 10 days along the complex Patagonian shelf break (variable direction and steepness). Comparisons with current-meter mooring data from the slope near the complex Brazil-Malvinas Confluence region are stringent tests for model performance. They showed that GLORYS12 lacked energy at periods less than 10 days (Figure 3). All along the slope, GLORYS12 reproduced peaks in SLA energy comparable to those from satellite altimetry, with however more energy at time scales shorter than 20 days.

Statistics over 25 years indicated three types of signals: signals in phase to the south of 47°S at the shelf break, fast propagating signals with phase speed ranging from 140 to 300 cm/s all along the shelf break, and slower signals in the core of the MC with propagation velocities ranging from 10 to 30 cm/s.

The large zonal wind stress variations south of 47°S were shown to force in-phase along-slope velocity variations and trigger fast propagating waves at specific locations of the shelf break (Figures 6 and 7). The fast waves (phase speed between 140 and 300 cm/s) departed from distinct sites corresponding to abrupt changes in the shelf-break orientation (Figure 6c). Along-slope velocity anomalies exceeded 15 cm/s at 100 m depth (Figure 7a). The waves impacted the intensity of the inshore jet associated with the SAF-N (Figure 1), which varied from 0 to 30 cm/s at 100 m depth over the 25 years (Figure 10).

The GLORYS12 SLA response to the wind generating the fast waves was large on the continental shelf (SLA composite up to 6 cm) and smaller along the shelf break (composite of 3 cm). Synoptic SLA at the shelf break at 47°S reached peak values larger than 5 cm lasting less than 20 days (Figure 11). Therefore, tracking these waves in the present satellite altimetry maps could be challenging.

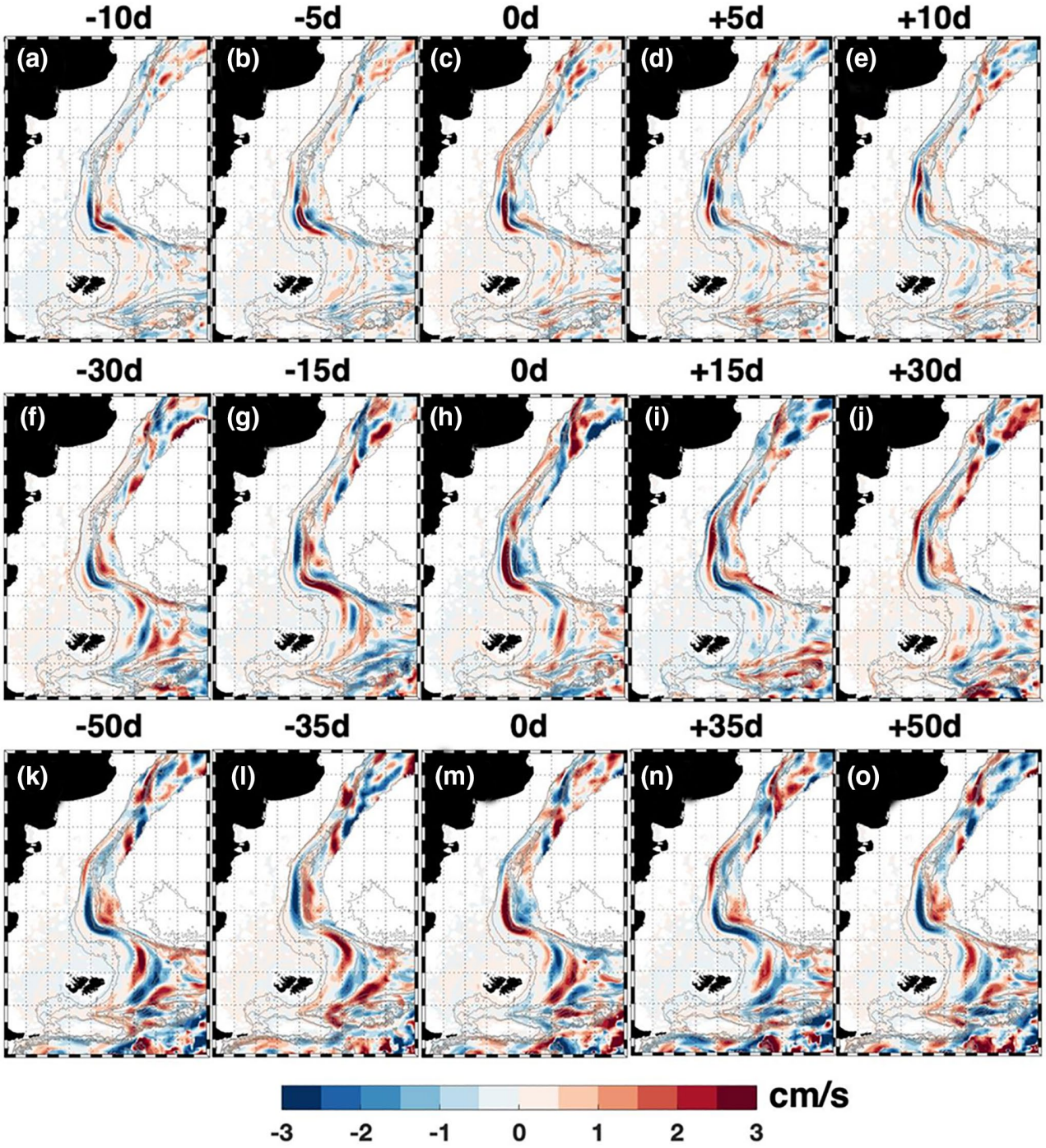

Figure 14. (a–e) Lagged composites of 10–40-day band-pass filtered along-slope velocities at 100 m from the dates when the filtered velocity exceeds the standard deviation at Ω (47°S). (f–j) Lagged composites of 30–90-day band-pass filtered along-slope velocities at 100 m from the dates when the filtered velocity exceeds the standard deviation at Ω (47°S). (k–o) Lagged composites of 80–110-day band-pass filtered along-slope velocities at 100 m from the dates when the filtered velocity exceeds the standard deviation at Ω (47°S).

Although Brink's model is too idealistic (e.g., Brunner et al., 2019) and requires several assumptions such as a straight coastline with similar slope bathymetry, which are not fulfilled along the Patagonian shelf break, it provided guidance to the interpretation of those waves. Their phase speed and their spatial structure across the slope corresponded to modes 2–4 in Brink's model (Figures 7–9). Their positive

w

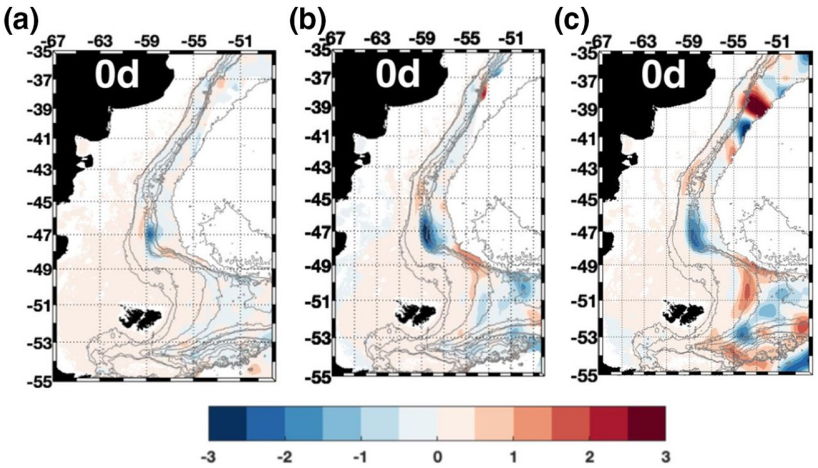

Figure 15. (a) Lag 0 composites of 10–40-day band-pass filtered sea level anomalies (SLAs) from GLORYS12 corresponding to selected dates used in Figure 13c. (b) Lag 0 composites of 30–90 day band-pass filtered SLAs corresponding to selected dates used in Figure 13h. (c) Lag 0 composites of 80–110-day band-pass filtered SLAs corresponding to selected dates used in Figure 13m.

stage featured increased northward along-slope velocity (5–20 cm/s) associated with inshore cross-slope velocities (1–2 cm/s). Scaling with Brink's theory predicted positive vertical velocities of the order 5–20 m/day associated with inshore horizontal velocities of 1 cm/s in the positive phase (reverse in negative phase). Thus, the fast waves could contribute to enhance transport of nutrients from the MC onto the shelf. Short-term moorings above the 200-m isobath at 41°S and 43.8°S provided evidences of upwelling events lasting 5–10 days extending over 500 km at the shelf break and requiring vertical velocities of the order of 13–29 m/day (Valla & Piola, 2015). The shelf-break fast waves in GLORYS12 had spatial and temporal velocity structures consistent with those of the observed upwelling events described in Valla and Piola (2015).

Three types of propagating waves in the core of the MC were identified. They correspond to periods of about 20, 60, and 100 days; phase speeds of 0.26, 0.19, and 14 cm/s; along-slope wavelengths of 450, 1,000, and 1,200 km, respectively; and to a cross-slope mode 2 or 3 with scales ranging from 25 to 50 km. These waves were not forced by the local winds. Composite velocity anomalies of the order of 6 cm/s (built from 1,429, 1,461, and 1,415 cases for the 20-, 60-, and 100-day period waves), associated with these waves were tracked back to the Drake Passage and the Malvinas Escarpment (Figure 14). The forcing mechanisms and the upstream paths of the waves observed in the core of the MC need further investigation.

The waves in the core of the MC changed characteristics at 43°S, accelerated and propagated up to 41°S, where they interacted with perturbations coming from the Brazil-Malvinas Confluence. Nonlinear processes such as scattering, interferences with other signals, damping effects, interaction with the mean flow, refraction, and reflection are beyond the scope of this paper. The impact of the TW on the MC transport and location of the Brazil-Malvinas Confluence is under investigation. Extreme transport maxima in the MC at 41°S were related with cyclonic eddies detached from the PF that propagate northward along the 400-m isobath (Artana et al., 2018a). The significant energetic peaks in a 30–110-day period band found in the MC transport at 41°S and in the velocity time series associated with the subducted inner branch of the MC at 37°S (Artana et al., 2019) could be associated with TW. Theoretical works also suggested that TW could affect the position of the encounter of the Brazil and Malvinas Current (Lebedev & Nof, 1997).

Appendix: Trapped Waves at 51°S, 47°S, and 42°S from Brink and Chapman (1987) Linear Model

Brink and Chapman (1987) considered a linear, inviscid problem with constant rotation, horizontally uniform stratification ($N(z)$), and an alongshore nonvarying bottom topography ($h(x)$). Brink and Chapman's toolbox computes modal structures from bottom topography $h(x)$, offshore stratification $N^2(z)$, mean flow

($V(x, z)$), for a given frequency and wavenumber. We applied the toolbox to three sections (51°S, 47°S, and 42°S) shown in Figure A1a (pink, red, and blue). Following GLORYS12 mean flow values of the Malvinas Current, the idealized mean flow, $V(x,z)$, is composed of one or two northward jets depending on the section (Figures A1b–A1d). Taking into account the two-jet structure intensified the mode in the vicinity of the jets. Similarly, following GLORYS12, we chose an idealized stratification weak and uniform along the Malvinas Current (Figure A1f).

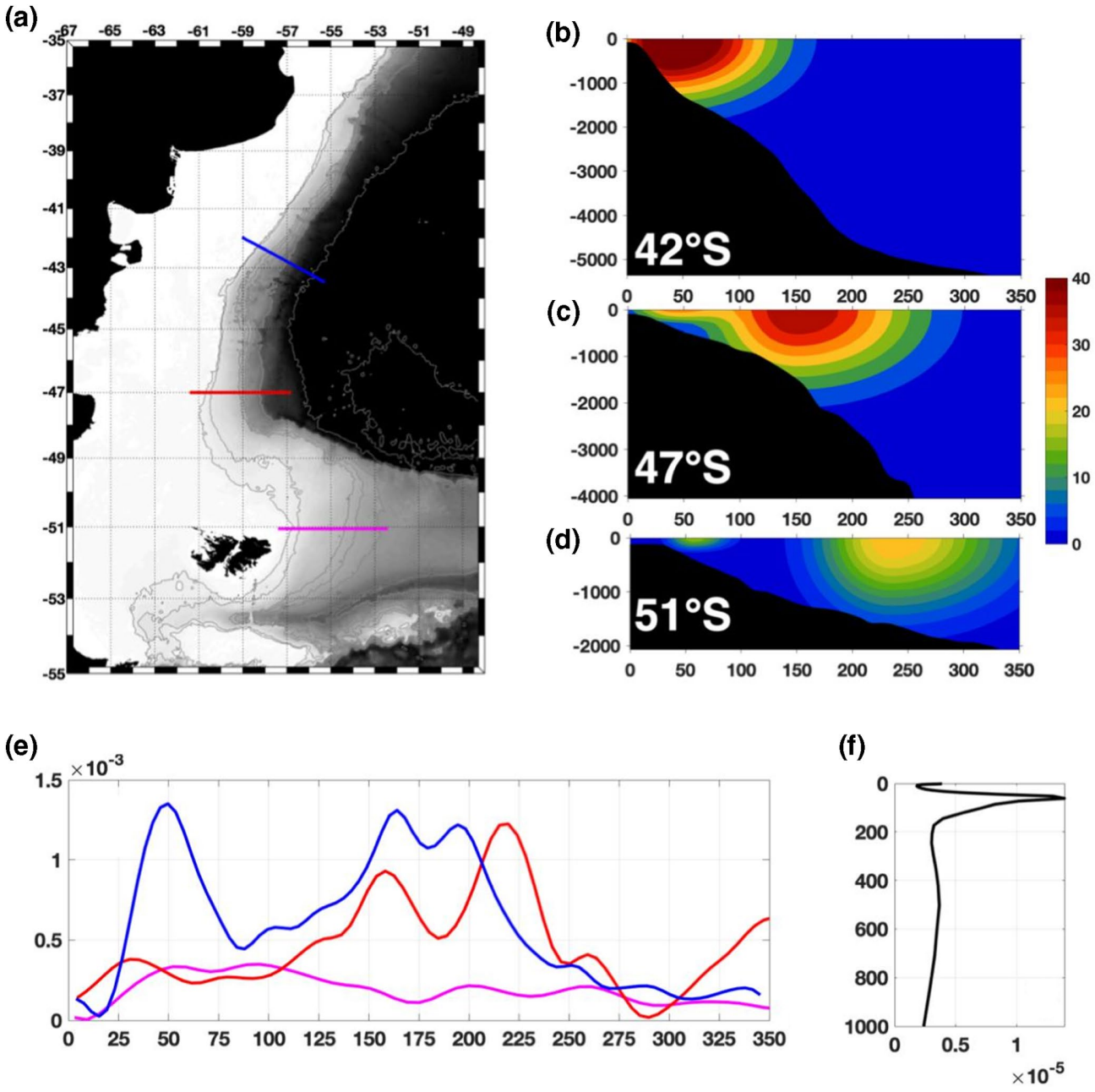

Figure A1. Setup conditions for Brink and Chapman's model application: (a) Bathymetry with the three sections under consideration. (b–d) Idealized mean along-slope velocities for the three sections (51°S, 47°S, and 42°S), x-axis is the distance in km. (e) Mean Burger number is a function of the distance along each section. x-axis is the distance in km and y-axis is the Burger number. (f) Mean Brunt Vaisala frequency at 300 km for each section. x-axis is the Brunt Vaisala frequency in $S-1$, y-axis is depth in meters.

The structure of the modes is dependent on the Burger number: $S = (\alpha\ N/f)^2$ with α the cross-shore slope in m/m, N the mean coastal Brünt-Väisälä frequency, and f the Coriolis parameter (Figure A1e). Small values of S ($S < 1$) correspond to fast propagating barotropic shelf waves, where the rotation dominates over gravity, while a large value ($S > 1$) of S corresponds to slow-propagating baroclinic waves. S along the three cross-slope sections was lower than 1 suggesting barotropic modes. The three modes featured larger velocity anomalies near the shelf break for the three sections (Figure A2). The mode 3 featured inshore across slope velocity associated with positive vertical velocities for the three sections (Figure A3).

For 1,500 km (consistent with the length of the Patagonian slope of the order of 3,000 km), the theory provided waves with periods ranging between 1 and 30 days and phase speeds between 30 and 800 cm/s (Figures A4a and A4b). We focused on probably realistic wavelengths ranging between 600 and 1,500 km for which theory predicts low dispersive modes 2–4 waves (Figure A4b) with phase speeds ranging from 50 to 300 cm/s (Figure A4b).

Data Availability Statement

The satellite data and model outputs are available at Copernicus Marine Environment Monitoring Service (CMEMS; http://marine.copernicus.eu/) and the in situ data are available at SEANOE (www.seanoe.org; cf. https://doi.org/10.17882/51479, https://doi.org/10.17882/51483, and https://doi.org/10.17882/51492).

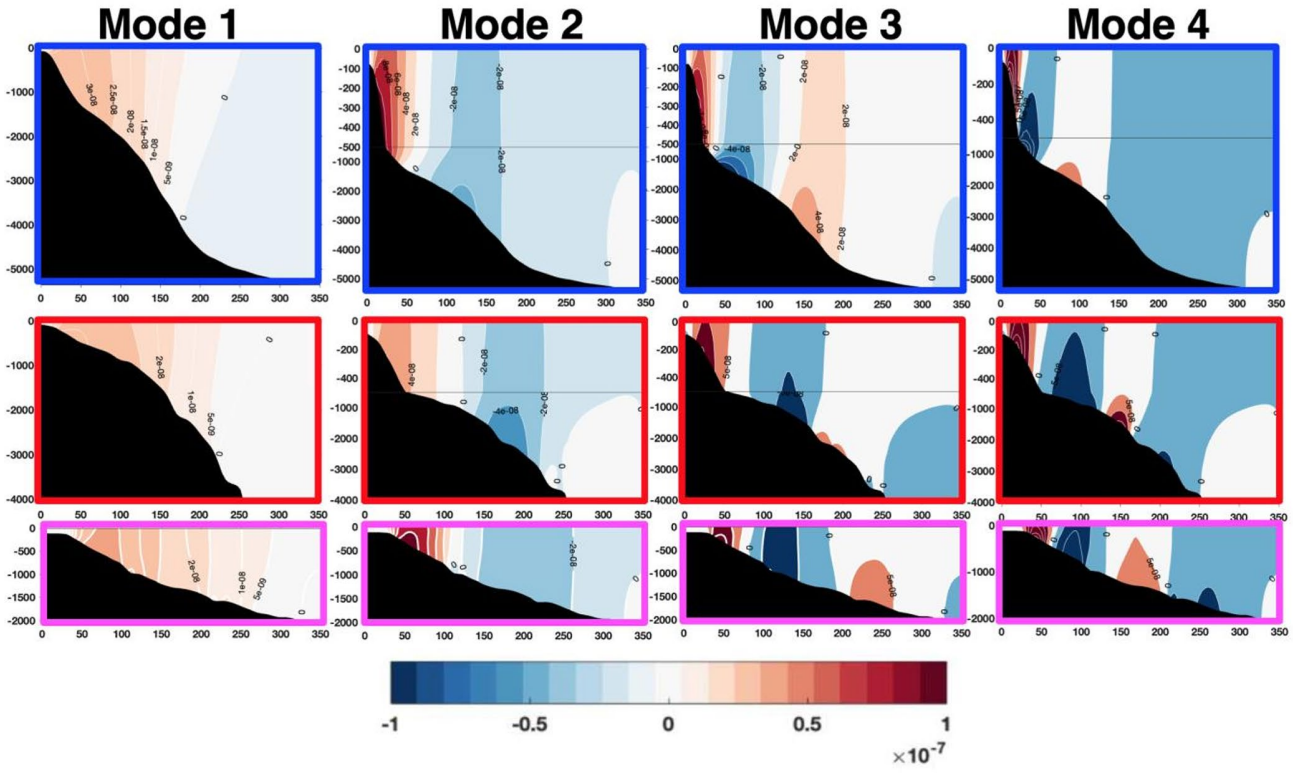

Figure A2. First four gravest modes of along-isobath velocity computed from Brink and Chapman (1987) toolbox at 51°S, 47°S, and 42°S (pink, red, and blue sections in Figure A1) (the velocities are normalized by an arbitrary factor – their units are consistent). x-axis is across-slope distance; y-axis is the depth.

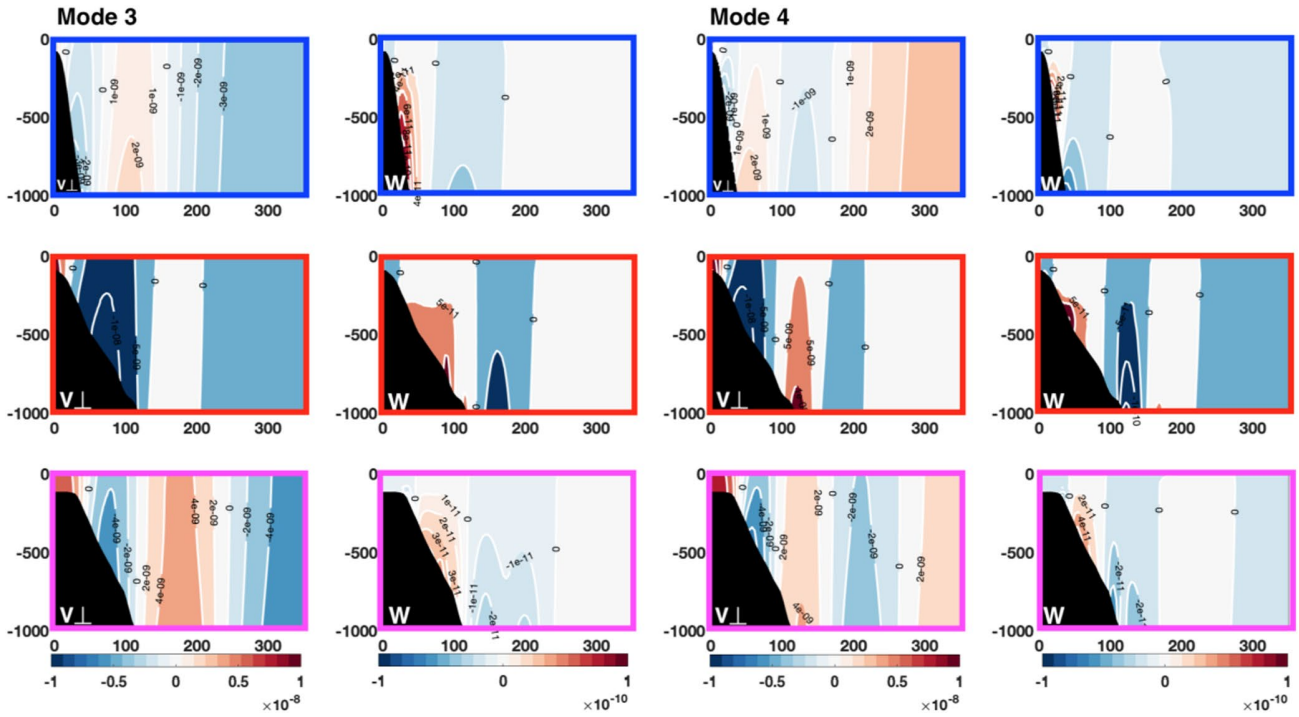

Figure A3. Across-isobath and vertical velocity components associated with modes 3 and 4 along section 51°S, 47°S, and 42°S (shown in Figure A1). Scaling as in Figure A2. Zoom on the upper 1,000 m. Positive across-slope velocity corresponds to velocity from the shelf to the open ocean and positive vertical velocity corresponds to upwards velocity.

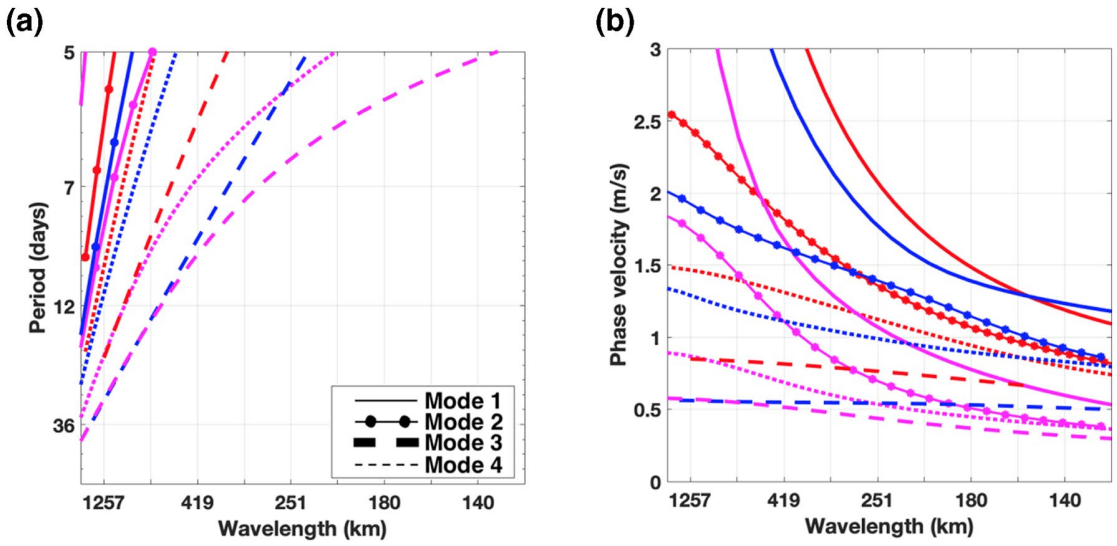

Figure A4. (a) Dispersion curves for the first four gravest modes of the 51°S section (pink), 47°S section (red), and for 42°S section (blue). *x*-axis is the wavelength in km, *y*-axis is the period in days. Thick lines correspond to mode 1, thick lines with dots to mode 2, thick dashed lines to mode 3, and dashed lines to mode 4. (b) Phase velocity computed for each mode (same color code as a). *x*-axis is wavelength in km and *y*-axis is the velocity in m/s.

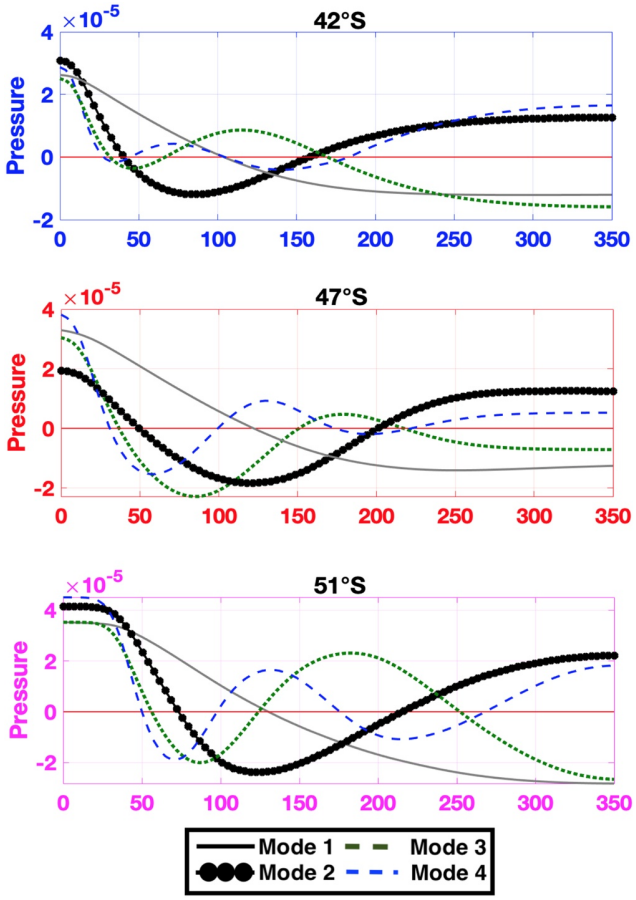

Figure A5. Surface pressure (SP) for modes 1–4 along sections at 51°S, 47°S, and 42°S. Units in dyn/cm^2 (1 dyn/cm^2 = 0.1 Pa).

Acknowledgments
We thank the editor, Don Chambers, an anonymous reviewer, and Josep Lluís Pelegrí for a number of constructive comments and suggestions. We are grateful to the CNES (Centre National d'Etudes Spatiales) for constant support. This study is a contribution to EUMETSAT/CNES DSP/OT/12-2118. Léa Poli acknowledges support from Sorbonne Université and Camila Artana from a CNES Postdoc Scholarship.

References

Archer, M. R., Li, Z., & Fu, L.-L. (2020). Increasing the space–time resolution of mapped sea surface height from altimetry. *Journal of Geophysical Research: Oceans*, *124*, e2019JC015878. https://doi.org/10.1029/2019JC015878

Artana, C., Ferrari, R., Koenig, Z., Saraceno, M., Piola, A. R., & Provost, C. (2016). Malvinas Current variability from Argo floats and satellite altimetry. *Journal of Geophysical Research: Oceans*, *121*, 4854–4872. https://doi.org/10.1002/2016JC011889

Artana, C., Lellouche, J.-M., Park, Y.-H., Garric, G., Koenig, Z., Sennéchael, N., et al. (2018). Fronts of the Malvinas Current system: Surface and subsurface expressions revealed by satellite altimetry, Argo floats, and Mercator operational model outputs. *Journal of Geophysical Research: Oceans*, *123*, 5261–5285. https://doi.org/10.1029/2018JC013887

Artana, C., Provost, C., Lellouche, J.-M., Rio, M.-H., Ferrari, R., & Sennéchael, N. (2019). The Malvinas current at the confluence with the Brazil current: Inferences from 25 Years of Mercator Ocean reanalysis. *Journal of Geophysical Research: Oceans*, *124*. https://doi.org/10.1029/2019JC015289

Ballarotta, M., Ubelmann, C., Pujol, M. I., Taburet, G., Fournier, F., Legeais, J. F., et al. (2019). On the resolutions of ocean altimetry maps. *Ocean Science*, *15*(4), 1091–1109. https://doi.org/10.5194/os-15-1091-2019

Barré, N., Provost, C., Renault, A., & Sennéchael, N. (2011). Fronts, meanders and eddies in Drake passage during the ANT-XXIII/3 cruise in January–February 2006: A satellite perspective. *Deep Sea Research Part II: Topical Studies in Oceanography*, *58*(25–26), 2533–2554. https://doi.org/10.1016/j.dsr2.2011.01.003

Brink, K. H. (1982). A comparison of long coastal trapped wave theory with observations off Peru. *Journal of Physical Oceanography*, *12*, 897–913.

Brink, K. H. (1989). Energy conservation in coastal-trapped wave calculations. *Journal of Physical Oceanography*, *19*, 1011–1016.

Brink, K. H., & Chapman, D. C. (1987). *Programs for computing properties of coastal-trapped waves and wind-driven motions over the continental shelf and slope* (Technical Report WHOI-87-24, p. 122). Woods Hole, MA: Woods Hole Institution.

Brunner, K., Rivas, D., & Lwiza, K. M. M. (2019). Application of classical coastal trapped wave theory to high scattering regions. *Journal of Physical Oceanography*, *49*, 2201–2216. https://doi.org/10.1175/JPO-D-18-0112.1

Cabanes, C., Grouazelm, A., von Schuckmann, K., Hamon, M., Turpin, V., Coatanoan, C., et al. (2013). The CORA dataset: Validation and diagnostics of in-situ ocean temperature and salinity measurements. *Ocean Science*, *9*(1), 1–18. https://doi.org/10.5194/os-9-1-2013

Ferrari, R., Artana, C., Saraceno, M., Piola, A. R., & Provost, C. (2017). Satellite altimetry and current-meter velocities in the Malvinas Current at 41°S: Comparisons and modes of variation. *Journal of Geophysical Research: Oceans*, *122*, 9572–9590. https://doi.org/10.1002/2017JC013340

Lebedev, I., & Nof, D. (1997). Collision of boundary currents: Beyond a steady state. *Deep Sea Research Part I: Oceanographic Research Papers*, *44*(5), 771–791. https://doi.org/10.1016/S0967-0637(96)00127-6

Lellouche, J.-M., Greiner, E., Le Galloudec, O., Garric, G., Regnier, C., Drevillon, M., et al. (2018). Recent updates on the Copernicus Marine Service global ocean monitoring and forecasting real-time 1/12° high resolution system. *Ocean Science*, *14*, 1093–1126. https://doi.org/10.5194/os-2018-15

Paniagua, G. F., Saraceno, M., Piola, A. R., Guerrero, R., Provost, C., Ferrari, R., et al. (2018). Malvinas Current at 40-41°S: First assessment of temperature and salinity variability. *Journal of Geophysical Research: Oceans*, *123*, 8. https://doi.org/10.1029/2017JC013666

Piola, A. R., Franco, B. C., Palma, E. D., & Saraceno, M. (2013). Multiple jets in the Malvinas Current. *Journal of Geophysical Research: Oceans*, *118*, 2107–2117. https://doi.org/10.1002/jgrc.20170

Pujol, M.-I., Faugère, Y., Taburet, G., Dupuy, S., Pelloquin, C., Ablain, M., & Picot, N. (2016). DUACS DT2014: The new multi-mission altimeter data set reprocessed over 20 years. *Ocean Science*, *12*(5), 1067–1090. https://doi.org/10.5194/os-12-1067-2016

Romero, S. I., Piola, A. R., Charo, M., & Garcia, C. A. E. (2006). Chlorophyll-a variability off Patagonia based on SeaWiFS data. *Journal Geophysical Research*, *111*, C05021. https://doi.org/10.1029/2005JC003244

Smith, W. H. F., & Sandwell, D. T. (1994). Bathymetric prediction from dense satellite altimetry and sparse shipboard bathymetry. *Journal of Geophysical Research*, *99*(B11), 21803–21824. https://doi.org/10.1029/94JB00988

Spadone, A., & Provost, C. (2009). Variations in the Malvinas Current volume transport since October 1992. *Journal of Geophysical Research*, *114*, C02002. https://doi.org/10.1029/2008JC004882

Szekely, T., Gourrion, J., Pouliquen, S., & Reverdin, G. (2016). *CORA, Coriolis, Ocean Dataset for Reanalysis*. SEANOE. https://doi.org/10.17882/46219

Taburet, G., Sanchez-Roman, A., Ballarotta, M., Pujol, M.-I., Legeais, J.-F., Fournier, F., et al. (2019). DUACS DT2018: 25 years of reprocessed sea level altimetry products. *Ocean Science*, *15*, 1207–1224. https://doi.org/10.5194/os-15-1207-2019

Valla, D., & Piola, A. R. (2015). Evidence of upwelling events at the northern Patagonian shelf break. *Journal of Geophysical Research: Oceans*, *120*, 7635–7656. https://doi.org/10.1002/2015JC011002

Vivier, F., & Provost, C. (1999). Direct velocity measurements in the Malvinas Current. *Journal of Geophysical Research*, *104*(C9), 21083–21103. https://doi.org/10.1029/1999JC900163

Vivier, F., Provost, C., & Meredith, M. (2001). Remote and local forcing in the Brazil Malvinas Region. *Journal of Physical Oceanography*, *31*, 892–913. https://doi.org/10.1175/1520-0485

Chapter 3

Topographically Trapped Waves around South America with periods between 40 and 130 days in a global ocean reanalysis : An Oceanic teleconnection between the equatorial Pacific and the tropical Atlantic.

In the previous study, we highlighted the existence of fast propagating trapped waves along the patagonian shelf break. The variance preserving spectra (Figure 2 in Poli et al.,2020) shows latitudinnally continuous peaks at periods between 40 and 130 days partly due to the waves described in Poli et al.,2020. Interestingly, some peaks around 50, 70 and 110 days seems to come from the Drake Passage. These results motivate us to investigate the propagation of fast waves at period ranging between 40 and 130 days. Following the same methodology , we extend our analysis to the entire South American coast from

the Pacific to the Atlantic .

JGR Oceans

RESEARCH ARTICLE
10.1029/2021JC018067

Key Points:

- Coherent Sea Level Anomalies indicate trapped waves propagation along the slope from the Equatorial Pacific to the Tropical Atlantic (22°S)
- The Madden-Julian Oscillation (MJO), through oceanic and atmospheric teleconnections, plays a key role in forcing the trapped waves
- Furthermore, local winds trigger waves in specific locations, such as the south-east Pacific and the Brazil-Malvinas Confluence

Correspondence to:
L. Poli,
lea.poli@locean.ipsl.fr

Citation:
Poli, L., Artana, C., & Provost, C. (2022). Topographically trapped waves around South America with periods between 40 and 130 days in a global ocean reanalysis. *Journal of Geophysical Research: Oceans*, *127*, e2021JC018067. https://doi.org/10.1029/2021JC018067

Received 29 SEP 2021
Accepted 2 FEB 2022

The copyright line for this article was changed on 7 JUL 2022 after original online publication.

Topographically Trapped Waves Around South America With Periods Between 40 and 130 Days in a Global Ocean Reanalysis

Léa Poli[1], Camila Artana[2], and Christine Provost[1]

[1]Laboratoire LOCEAN-IPSL, Sorbonne Université (UPMC, Univ. Paris 6), CNRS, IRD, MNHN, Paris, France, [2]Mercator Ocean, Toulouse, France

Abstract The South American continental slope hosts a variety of topographic waves. We use a 27-year-long global ocean reanalysis (1/12° Spatial resolution) to examine trapped waves (TWs) around South America at periods ranging from 40 to 130 days. The waves propagate from the Equatorial Pacific to the Tropical Atlantic (22°S) with phase velocities between 1.8 and 7 m/s according to the local background characteristics, such as stratification, slope steepness, latitude, mean flow and shelf width. The Madden-Julian Oscillation (MJO) plays a key role in forcing the TWs in two ways (a) through an oceanic connection implying equatorial Kelvin waves reaching the western American Coast and (b) through an atmospheric teleconnection enhancing southerly winds in the south-east Pacific. Furthermore, local winds, not necessarily linked with the MJO, modulate and trigger waves in specific locations, such as the Brazil-Malvinas Confluence. Trapped waves impact the along-shore currents: during the positive phase of the waves the near-surface flow is enhanced by about 0.1 m/s.

Plain Language Summary Several waves propagate around South America from the Equatorial Pacific to the Tropical Atlantic (22°S) along the continental slope. The waves propagate relatively fast with velocities varying between 1.8 and 7 m/s depending on the local background for example, the continental slope geometry. Two forcing mechanisms were identified: a Pacific Equatorial forcing associated with climatic indices and a local wind forcing at specific locations such as the south-east Pacific and the Brazil-Malvinas Confluence. The waves impact the along-shore currents: the flow is modulated by about 0.1 m/s.

1. Introduction

The South American continental slope hosts a variety of sub-inertial trapped waves (TWs) propagating with the coast to their left with periods ranging from few days to months (Clarke, 1992; Brink, 1982, Figure 1a). TWs have been documented both on the Pacific and Atlantic continental slope from in-situ data and model studies.

The Pacific Ocean equatorial dynamics, mainly modulated by the El Niño Southern Oscillation (ENSO) and the Madden-Julian Oscillation (MJO) impact the South American continental slope through atmospheric and oceanic teleconnections (e.g., Conejero et al., 2020; Madden & Julian, 1994; Sprintall et al., 2020). Equatorial Kelvin Waves, forced by large scale wind stress anomalies, travel eastward and reach the western American coast where part of their energy excites weakly dissipative TWs which propagate southward along the continental slope (Clarke & Shi, 1991; Kessler et al., 1995; Roundy & Kiladis, 2006; Sprintall et al.,2020). Indeed, propagation of sea level and along-shore velocity anomalies along the Pacific side at subseasonal periods (50, 70, and 120 days) have been documented (e.g., Clarke & Ahmed, 1999; Pizarro et al., 2001). The observed TWs had speeds comparable to the first and second mode of coastal Kelvin waves (order of 2 m/s) and spatial structures consistent with those predicted by linear theory (Brink, 1982; Illig et al., 2018).

On the Atlantic side, local wind anomalies over the southern Patagonian platform and around 40°S trigger northward propagating shelf-break and coastal TWs with rather short periods ranging between 5 and 30 days (Freitas et al., 2021; Poli et al., 2020). Waves depart at distinct sites corresponding to abrupt changes in the shelf-break orientation (Poli et al., 2020). North of the Abrolhos Plateau (AP; 22°S) the width of the shelf reduces dramatically which makes this region a hotspot for wave energy dissipation (Freitas et al., 2021).

Signatures of lower frequency TWs have also been observed from in situ and satellite data and model outputs on the Atlantic side. Vivier et al. (2001) observed energetic peaks at intraseasonal timescales (between 50 and 110 days) in velocity spectra from current meter mooring data, located at 41°S on the Atlantic continental slope.

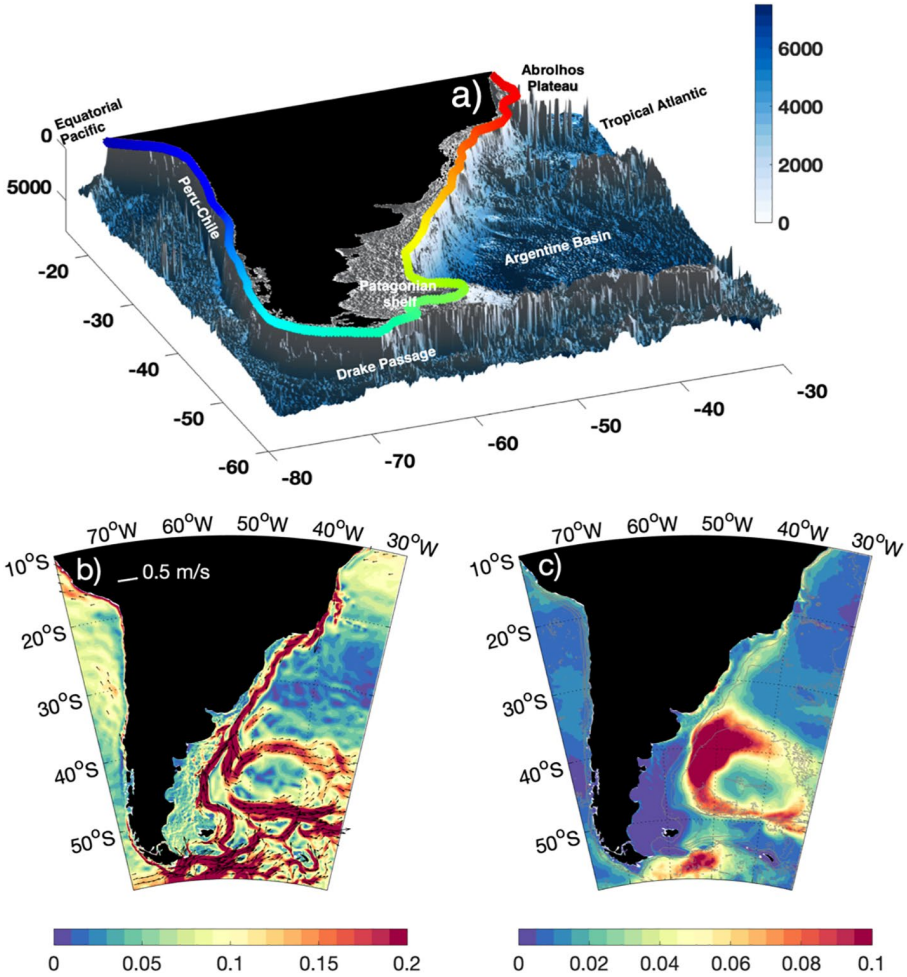

Figure 1. (a) Bathymetry (in m) used in GLORYS12. The colored track follows the 300 m isobath marking the shelf break. (b) Mean surface velocity (m/s) (arrows and amplitude in color). The arrows corresponding to velocities larger than 10 cm/s are from GLORYS12 over 1993–2019. (c) Mean eddy kinetic energy (m^2/s^2). Isobaths 6000, 5000, 3000, 2000, 300 are indicated in gray.

They suggested that those peaks could be related with TW propagating from the Pacific following the southern edge of South America and continuing their propagation in the Atlantic along the Patagonian slope. Hughes and Meredith (2006) identified strong coastal satellite sea level anomalies (SLA) correlations between the eastern and western side of South America resulting from the propagation of TWs from the Equatorial Pacific (EP) to the Patagonian shelf. Combes and Matano (2019) investigated the influence of remote wind forcing on low frequency (periods ≥60 days) SLA over the Patagonian platform with model experiments. They highlighted the influence of EP dynamics and winds along the southern Chilean coast in forcing SLA on the Patagonian Platform through TWs.

Modifications of the TW structures are expected along the propagation due to changing background. Indeed, the South American Pacific and Atlantic sides present contrasted characteristics regarding seafloor topography (Figure 1a) and ocean circulation (Figures 1b and 1c). The Pacific coast has a quasi-meridional orientation and the continental slope is steep (100 m/km) north of 38°S (subduction zone with a fault reaching 6,000 m depth) and more gentle (60 m/km) to the south. On the Atlantic side, the continental platform is wide in the south (1,000 km wide at 50°S) and very narrow to the north of 22°S. The shelf break is rather sinuous and the continental slope gentle in the southern part (20 m/km around the Malvinas Islands) and steeper (50 m/km) north of 46°S. Currents along the Pacific slope, the northward Humbolt Current north of 42°S and the poleward Cape Horn Current south of 45°S, are rather weak, seasonally varying with mean velocities of the order of few cm/s (e.g.,

Strub et al., 2019). In contrast, the western boundary currents on the Atlantic side are strong with the Malvinas Current (MC), an emanation of the Antarctic Circumpolar Current, flowing northward with surface velocities reaching 0.6 m/s and the poleward Brazil Current with surface velocities of 0.3 m/s (Figure 1b). The encounter of these two currents around 40°S generates strong eddy kinetic energy (≥0.1 m^2/s^2, Figure 1c) making the western Atlantic one of the most energetic region of the world's oceans. In contrast the eddy kinetic energy on the Pacific side is rather weak (≤0.01 m^2/s^2; Figure 1c).

We aim at revisiting TWs propagating around South America focusing on the propagation and evolution and investigating the forcing mechanisms. We take advantage of the 27 years global ocean reanalysis GLORYS12 which provides a tridimensional view of the ocean state. Previous works have assessed the performance of GLORYS12 in the MC system and in the Drake Passage (DP) and showed the skills of the reanalysis in reproducing the circulation and the hydrography of the region (Artana et al., 2018, 2019; Poli et al., 2020). In Section 2 we present the GLORYS12 reanalysis which we further validate comparing model SLA with observations from tide gauges located around South America. We present the linear theoretical model (Brink, 1982) which provided guidance for our study. In Section 3, we explore the sea level spectral content around South America and the propagation characteristics of the waves. Section 4 investigates the wave occurrences, the forcing mechanism, the vertical structure and the impact on along-shore velocities around South America. Section 5 summarizes and concludes.

2. Data and Method

2.1. GLORYS12 Reanalysis

The high-resolution (1/12°) global Mercator Ocean reanalysis (hereafter GLORYS12) has been developed in the framework of the Copernicus Marine Environment Monitoring Service (CMEMS, http://marine.copernicus.eu/) and covers the period from 1993 to 2019 (Lellouche et al., 2021). The ocean surface is forced by the global ERA-Interim atmospheric reanalysis from the European Center for Medium-Range Weather Forecasts. The model assimilates observations using a reduced-order Kalman filter with a 3-D multivariate modal decomposition of the background error and a 7-day assimilation cycle (Lellouche et al., 2021). The model assimilates jointly along track satellite altimetric data, satellite sea surface temperature, sea-ice concentration, and in situ temperature and salinity vertical profiles (Lellouche et al., 2021). Artana et al. (2018) evaluated the performance of the reanalysis GLORYS12 over the MC and found a good agreement with observations. We further examine GLORYS12 performance comparing GLORYS12 SLA with tide gauges and satellite altimetric data. Daily filtered tide gauges data were downloaded from the sea level center of the University of Hawaii (http://uhslc.soest.hawaii.edu/data/) and the daily satellite data is the delayed time multi-satellite gridded product (with a grid spacing of 1/4°) produced by Ssalto/Duacs and distributed by CMEMS (http://marine.copernicus.eu/). The maps are produced using an optimal interpolation method applied to altimeter observations (Pujol et al., 2016). Due to the filtering properties the effective temporal resolution is not 1 day, rather 20 days and the effective spatial resolution in mid-latitudes is 200 km (Ballarotta et al., 2019).

We show comparisons for the years 2015–2016 which feature the largest tide gauge data return. Those years correspond to a period of high ENSO activity. We computed the SLA standard deviations (stds), The correlation and root mean square error (corr and rmse) between tide gauges and GLORYS12 time series and between tide gauges and satellite altimetry time series (Table 1). Tide gauges data are not assimilated in GLORYS12. Collocalized GLORYS12 SLA are well correlated with tide gauge data (above 0.5 above 99% significance level, Table 1) and match tide gauge data better than collocalized satellite altimetry product does (larger correlation [corr] and smaller root-mean-square error [rmse], Table 1). GLORYS12 SLA time series feature smaller stds than the tide gauges suggesting that the signal amplitude is in general underestimated by about 20%–40% in GLORYS12 (Table 1).

As an example, GLORYS12 SLA provides a spectrum at Arica with similar peaks to the tide gauge data spectrum in the period range 10–50 days whereas satellite altimetry spectrum shows discrepancies in the energy peak locations (Figure 2b). Distance-time SLA diagram along a track following the 300 m isobath show coherent SLA patterns around South America (Figure 2c). Correlations between GLORYS12 SLA signal on the track and the nearest tide gauge are still significant above 99% on the Pacific side and decrease on the Atlantic side probably

Table 1
Statistics of the Comparison Between GLORYS12 SLA, Satellite Altimetry and Tide Gauge Data at the Tide Gauge Location

	GLORYS12			Altimetry		
Tide Gauges (std in m)	corr	rmse (m)	std (m)	corr	rmse (m)	std (m)
Arica (0.06)	0.88	0.03	0.05	0.46	0.05	0.04
Antofagasta (0.06)	0.80	0.04	0.04	0.6	0.05	0.03
Caldeira (0.05)	0.80	0.03	0.04	0.62	0.04	0.03
Valparaiso (0.06)	0.66	0.04	0.04	0.36	0.05	0.04
Puerto Mont (0.08)	0.37	0.07	0.04	0.13	0.08	0.04
Ushuaia (0.17)	0.60	0.13	0.06	0.41	0.15	0.06
Puerto Madryn (0.18)	0.50	0.17	0.17	0.26	0.19	0.12
Mar del Plata (0.23)	0.78	0.10	0.17	0.32	0.20	0.08

due to the large shelf width in the south (not shown). The coherent SLA patterns observed in GLORYS12 are somewhat blurred in the satellite SLA distance-time diagram (Figure 2d).

2.2. Modal Structures of Trapped Waves From Linear Theory

Trapped Waves under the long wave assumption (sub-inertial frequencies and along-shore scales larger than the shelf width), can be described as a sum of modes whose spatial structure, phase and group velocities depend upon the cross-shore topography, stratification and mean flow (Brink, 1982). The structure of the waves depends on the Burger Number Bu= $\frac{\alpha^2 N^2}{f^2}$, with α the bathymetry gradient, N^2 the mean Brunt-Väisälä frequency averaged in the vertical and f the Coriolis parameter (Huthnance, 1978). The Burger number expresses the ratio between density stratification in the vertical and earth's rotation in the horizontal. $Bu < 1$ indicates barotropic dynamics and $Bu > 1$ baroclinic dynamics. The phase speed and vertical characteristics of the waves depend upon the baroclinicity. Brink (2018) considered a linear, inviscid problem with constant rotation, horizontally uniform stratification (N(z)), and an along-shore non-varying bottom topography (h(x)). Brink and Chapman developed a toolbox that computes modal structures from bottom topography h(x), offshore stratification N^2(z), mean flow (V (x, z)), for a given frequency and wavenumber, by resolving the linearized primitive equations (available at: https://darchive.mblwhoilibrary.org/handle/1912/10527). The dispersion curves and the wave structures were examined at four sections: at PN located at 25°S and PS at 50°S on the Pacific side and AS at 47°S and AN at 31°S on the Atlantic side (Figure 3a). The three first gravest modes are shown in Appendix A.

2.3. Climate Indices: El Niño Southern Oscillation (ENSO) and Madden-Julian Oscillation (MJO)

We use the detrended ENSO index (Niño 3.4) available at https://psl.noaa.gov/data/correlation/nina34. data El Niño or La Niña events are defined when the Niño 3.4 SSTs exceed ±0.4°C for a period of 6 months or more.

We also use the Original OLR MJO Index (MJO OOMI) available at https://psl.noaa.gov/mjo/mjoindex/. The index is a projection of 30–96 days eastward-only filtered OLR onto the spatial EOF patterns of 30–96 days eastward filtered OLR. This index indicates the activity and the phase of the oscillation (Kiladis et al., 2014).

2.4. ERA-Interim

We use winds (U10m and V10m) from ERA-Interim global atmospheric reanalysis provided by the European Center for Medium Range Weather forecast available at https://www.ecmwf.int/en/forecasts/datasets/reanalysis-datasets/era-interim. The system includes a four-dimensional variational analysis (4D-Var) with a 12-hr analysis window for the assimilation. The spatial resolution is approximately 80 km with 60 vertical levels in from the surface to 0.1 hPa (Dee et al., 2011).

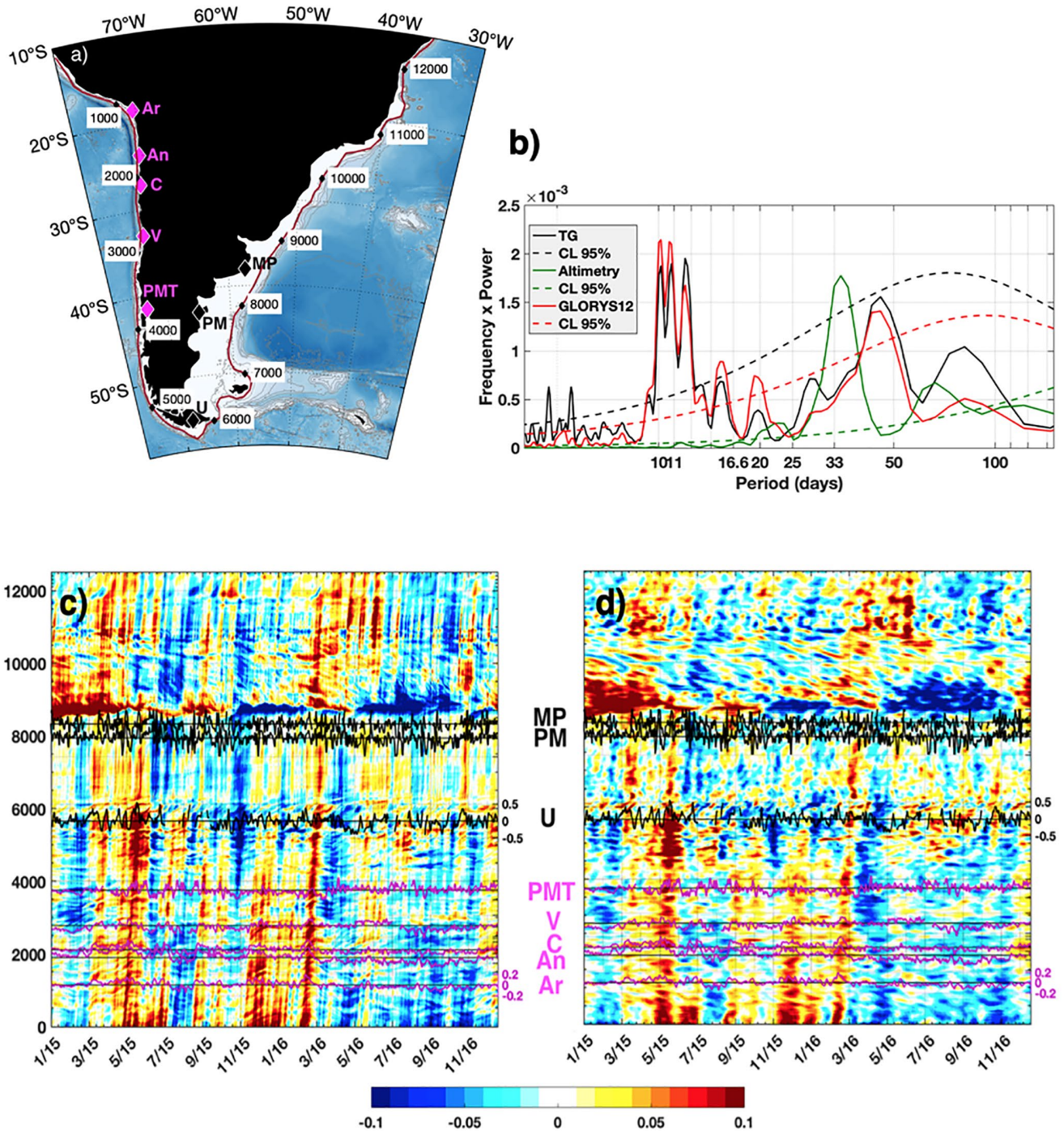

Figure 2. (a) Track along the 300 m isobath (brown curve) and tide gauge locations on the South American coastline. (b) Variance preserving spectra of SLA from GLORYS12, tide gauge (TG) and satellite altimetry at Arica. Dashed lines correspond to 95% confidence level (CL). Y-axis in m^2. (c) SLA distance-time diagram along the 300 m isobath from GLORYS12 for the period 2015–2016. X-axis is time (mm/yy) and Y-axis distance in kilometer along the track. Black (Atlantic side) and magenta (Pacific side) curves correspond to tide gauge data time-series with secondary y-axis (to the right) in meter. Magenta y-axis for Arica (Ar), Antofagasta (An), Caldeira (C), Valparaiso (V), Puerto Mont (PMT), and the black y-axis for Ushuaia (U), Puerto Madryn (PM), and Mar del Plata (MP). (d) Same as (c) for SLA satellite altimetry data.

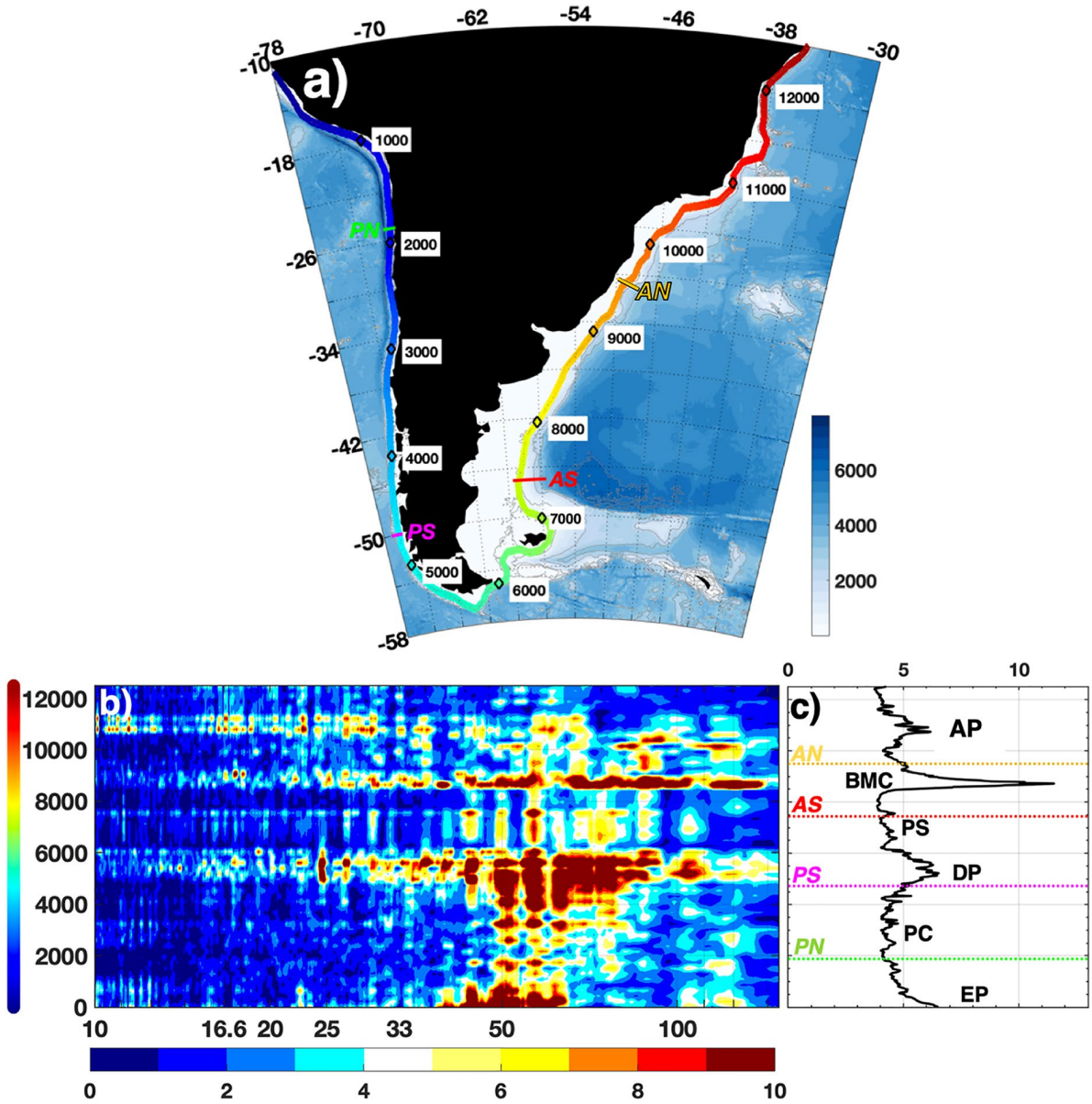

Figure 3. (a) Bathymetry (in m) and track following the South American shelf break (300 m isobath). Labels along the track indicate distance from 10°S to 78°W (off Peru). (b) Period – distance spectrum for SLA along the track around South America (bottom colorbar in cm^2). The colored line to the left of the y-axis indicates the position along the track (same colors as Figure 3a). Y-axis is distance along the track in kilometer and x-axis periods in days (log scale). (c) Standard deviation of sea level along the track (y-axis as in (b)) and x-axis in cm. PN, PS, AS, and AN correspond to the location of the four sections indicated in (a). EP, PC, DP, PS, BMC, and AB stand for Equatorial Pacific, Peru-Chile, Drake Passage, Brazil-Malvinas Confluence, and Abrolhos Plateau respectively.

3. Coherent SLA Propagation Around South America: 27 Years Overview and Statistics

3.1. Spectral Content

We examined the spectral content of SLA following the 300 m isobath (Figure 3a) and focused on the 10-150-day period range (Figure 3b). Four regions stand out in the spectrum: the EP (0 km), the DP (5,000–6000 km), the Brazil-Malvinas Confluence (BMC, 8,500–9,000 km), and the AP(11,000 km; Figures 3b and 3c).

The energy at periods shorter than 30 days between 6,000 and 8,000 km is associated with locally wind-forced TWs propagating northward along the Patagonian shelf documented by Poli et al. (2020) and between 10,000

and 13,000 km with those documented by Freitas et al. (2021). The SLA spectrum shows coherent energy peaks at periods ranging between 40 and 130 days all along the 300 m isobath. The energy is larger at DP and at the BMC where the SLA std along the 300 m isobath shows large peaks (Figures 3b and 3c). The coherent patterns between 40 and 130 days in Figure 3b suggest teleconnections between EP and Tropical Atlantic through TWs.

SLA wavelength-period spectra were produced considering the whole track following the 300 m isobath (Figure 4a). The spectrum indicates a cyclonic propagation of waves that is with the coast to the left (Figure 4a). The energy is particularly concentrated at periods between 40 and 130 days and wavelengths between 6,000 and 12,000 km. Energy peaks are consistent with theoretical modal dispersion curves computed with Brink's toolbox for the AS, AN, PS, and PN sections of Figure 3.

AS shows the largest phase speeds while the lowest ones are found on the Pacific side at PN. Therefore in Figure 4a we show the theoretical dispersion curves corresponding to the three gravest modes of these two extreme cases (AS in red and PN in green). The theoretical dispersion curves at PS and AN are located between those of PN and AS. Phase velocities range between 2 and 7 m/s for mode 1, between 1.4 and 3 m/s for mode 2, and between 1 and 1.5 m/s for mode three.

The difference in phase speeds reflects distinct background characteristics such as slope steepness and stratification. Indeed, the Burger number (Bu, Figure 4b) quantifies the impact of those parameters on the baroclinicity of the wave, when $Bu > 1$ the wave is expected to be baroclinic and when $Bu < 1$ barotropic. The theory predicts faster propagation for barotropic waves.

Figure 4b suggests a rather baroclinic structure on the Pacific side of South America and on the Atlantic side to the north of 38°S and a barotropic structure in the south of the Patagonian platform. This is consistent with theoretical phase speeds. The continuity of energy peaks between 40 and 130 days shown in Figure 3 and the contrasting phase velocities (Figure 4a) around South America could be indicative of an energy transfer between modes induced by the changing slope steepness and orientation, stratification and mean flow along the path (Figures 1 and 4b).

3.2. Coherent Propagative SLA Patterns and Their Phase Speeds

To isolate the low frequency waves propagating around South America we band-pass filtered model outputs between 40 and 130 days. Lagged correlations between a 27-year-long time series of filtered SLA at 60°W 47°S (300 m isobath at AS) and the SLA field show a coherent propagative signal coming from the EP (Figure 5). Lag 0 and lag −30 days show similar patterns with opposite signs suggesting a period of about 60–70 days and wavelength of about 12,000 km (Figure 5). The correlation reduces drastically at 22°S indicating a hotspot of wave energy loss probably associated with the abrupt change of the coast orientation near the AP.

We computed the Burger number (Bu) as well as the shelf width along the path (Figure 6a) and lagged correlations between 27-year-long time series of filtered SLA collocated along the track and SLA time series at PN (Figure 6b), PS (Figure 6c), AS (Figure 6d), and AN (Figure 6e). The lagged correlations show similar propagation patterns with a period of about 60/70 days. The wave periods are slightly shorter at the southern sections AS and PS (about 60 days) and larger at AN and PN (about 66 days) probably due to changes in the Coriolis parameter (Figure 6f). Propagation speed ranges from 1.8 m/s to 2.8 m/s between the EP (0 km) and DP (6,000 km). The wave then accelerates along the Patagonian shelf reaching speeds of about 4–7 m/s and then slows down to 1.8 m/s after the BMC. Interestingly Figures 6b–6d show a blurred signal and a decay in the correlation to the north of AN indicating that waves propagating from the Pacific strongly attenuate around 11,000 km. In contrast, correlations in panel d reflect a net northward propagating pattern with phase speed of 1.8 m/s to the north of AN. These correlations to the north of AN suggest a local wave forcing around AN (Figure 6e).

Bu is less than one (Figure 6a) along the Patagonian slope, where waves propagate faster, and exceeds one elsewhere where waves are slower, which is consistent with theory. Theory also predicts faster propagation speed over larger continental shelf as observed along the Patagonian platform where the width exceeds 500 km (Figure 6a).

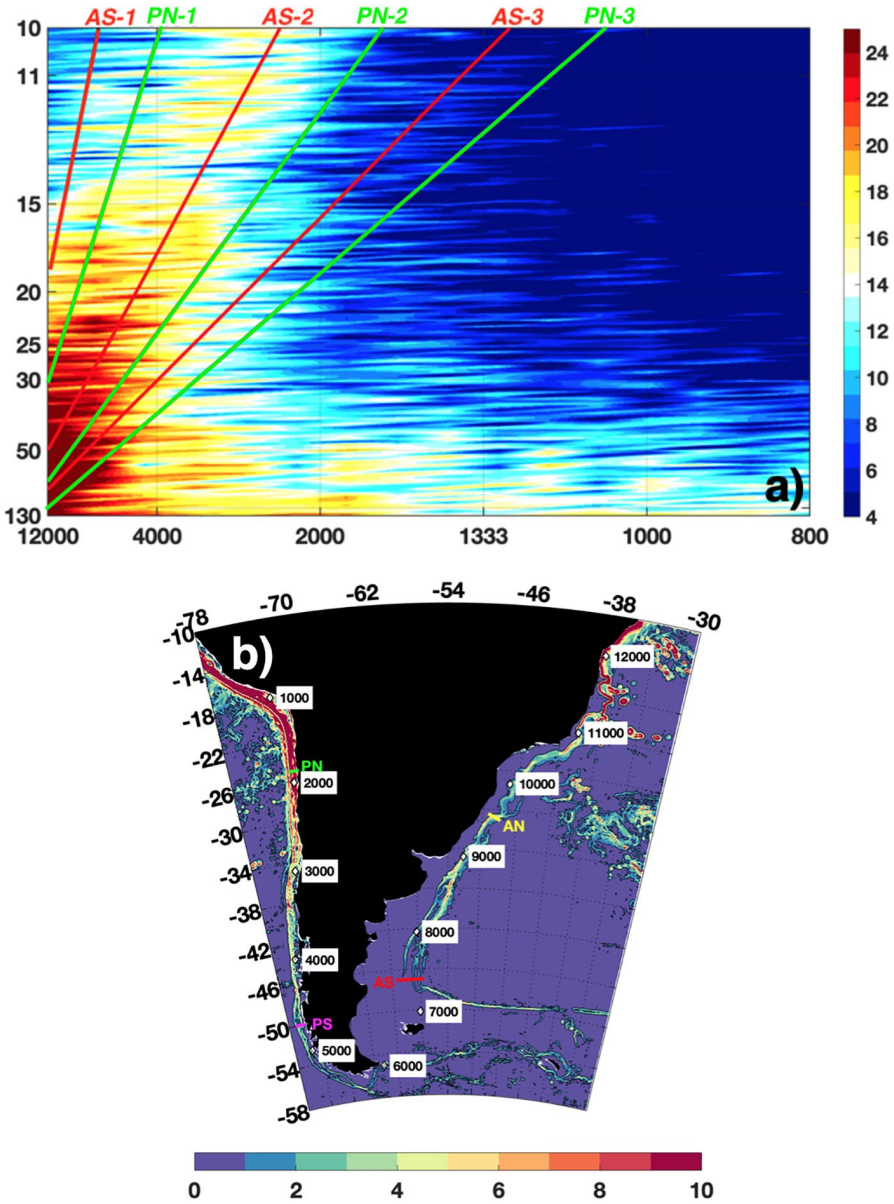

Figure 4. (a) SLA wavelength-period spectrum for the entire track over 27 years. X-axis is wavelength in kilometer and y-axis periods in days. The curves represent the theoretical dispersion relations for the first three gravest modes at PN (green) and AS (red) sections computed with Brink's toolbox (cf. Section 2.2). Colorbar units: SLA power spectral density. (b) Mean Burger number ($\frac{\alpha^2 N^2}{f^2}$ with α the slope, N the vertically averaged Brunt Väisälä frequency and f the Coriolis parameter) from GLORYS12 over the 1993–2019 period. Black contour is Bu = 1.

4. Trapped Waves Evolution Around South America

4.1. Waves Occurrences and Climate Indices

Figure 7a presents a distance-time diagram along the track following the 300 m isobath of filtered SLA from 1993 to 2019. Striking features are the intermittent coherent SLA propagative patterns from 0 to 12,000 km. Between 3,000 and 6000 km the SLA signal is more continuous in time suggesting a local reinforcement. The SLA signal associated with the BMC clearly appears at 9,000 km. Several propagative SLA signals seem to be generated intermittently at the Confluence (e.g., in 2010) possibly corresponding to the signal seen to the north of AN in Figure 6e.

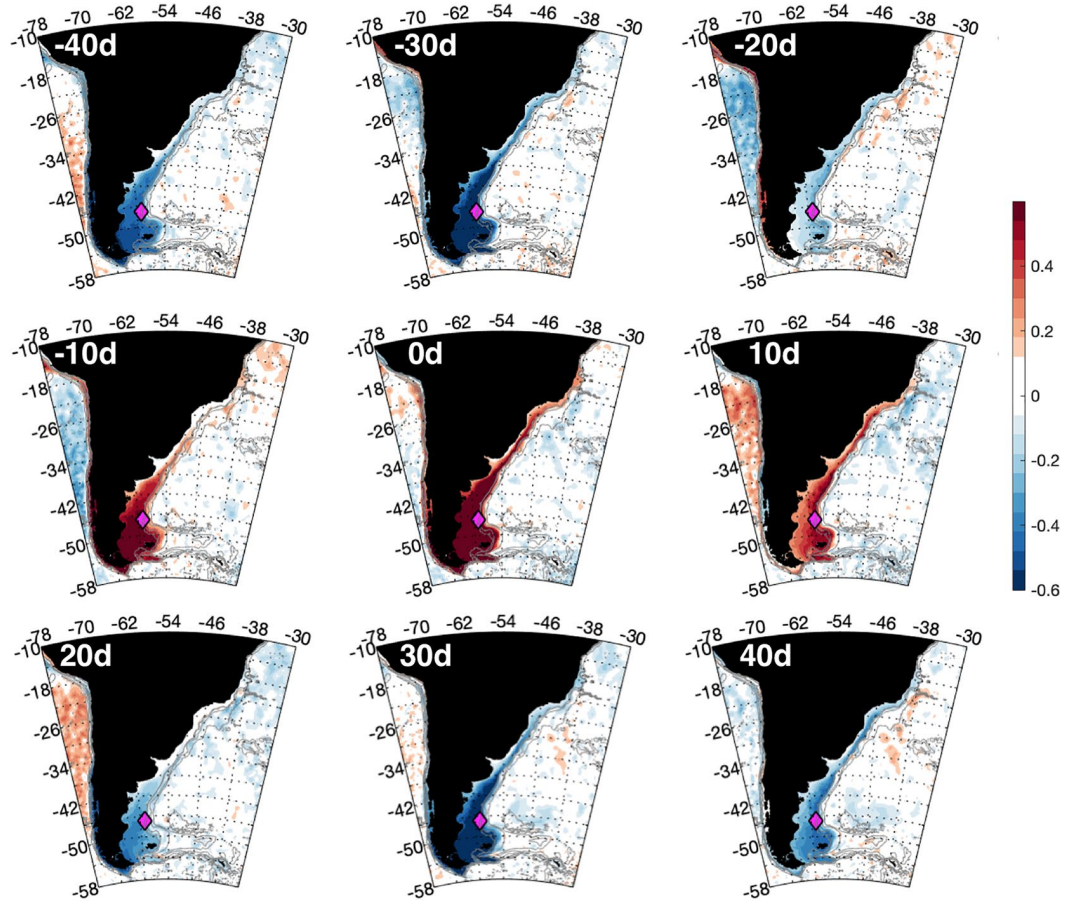

Figure 5. Lagged correlation of SLA with SLA time series at 47°S 60°W (magenta diamond on AS section) for the period 1993–2019. SLA was band-pass filtered between 40 and 130 days. Lags are indicated in white. Only significant correlations are colored.

We produced envelopes of filtered SLA intensity time series at the intersection of the sections and the 300 m isobath (Figure 7b). The envelopes were computed using smoothing a spline method. The envelopes can be considered as a proxy of the wave activity (Roundy & Kiladis, 2006). Most of the time the envelopes at PN, PS, AS, and AN are in phase. The amplitude at PS is generally larger (in pink in Figure 7b) corresponding to the intensified signal mentioned above. At times, the signal is larger at AN (in yellow in Figure 7b; e.g., in 2010) as observed in Figure 7a.

The envelope time series seem to be modulated over time featuring larger values during the following periods: 1997–1998, 2002–2005, 2009–2010, 2015–2016 and 2019, corresponding to El-Niño periods as illustrated with El Niño 3.4 index in Figure 7c.

The strong wave activity around South America starts before the El Niño episodes which is consistent with equatorial kelvin waves preceding (and generating) El Niño events (Hendon et al., 1998; Kessler & Kleeman, 2000; McPhaden, 1999; Roundy & Kiladis., 2006). The wave activity around South America lasts during each El Niño period. Therefore the El Niño phenomena seem to modulate the wave activity at low frequency (>3 years).

The MJO (Madden & Julian, 1994) with a characteristic periods of 50 days is an important mechanism in the generation of Equatorial Kelvin waves (Roundy & Kiladis, 2006). Indeed, the OOMI index Amplitude time series (see Section 2.3) seems to mimic the SLA envelope time series (Figure 7d).

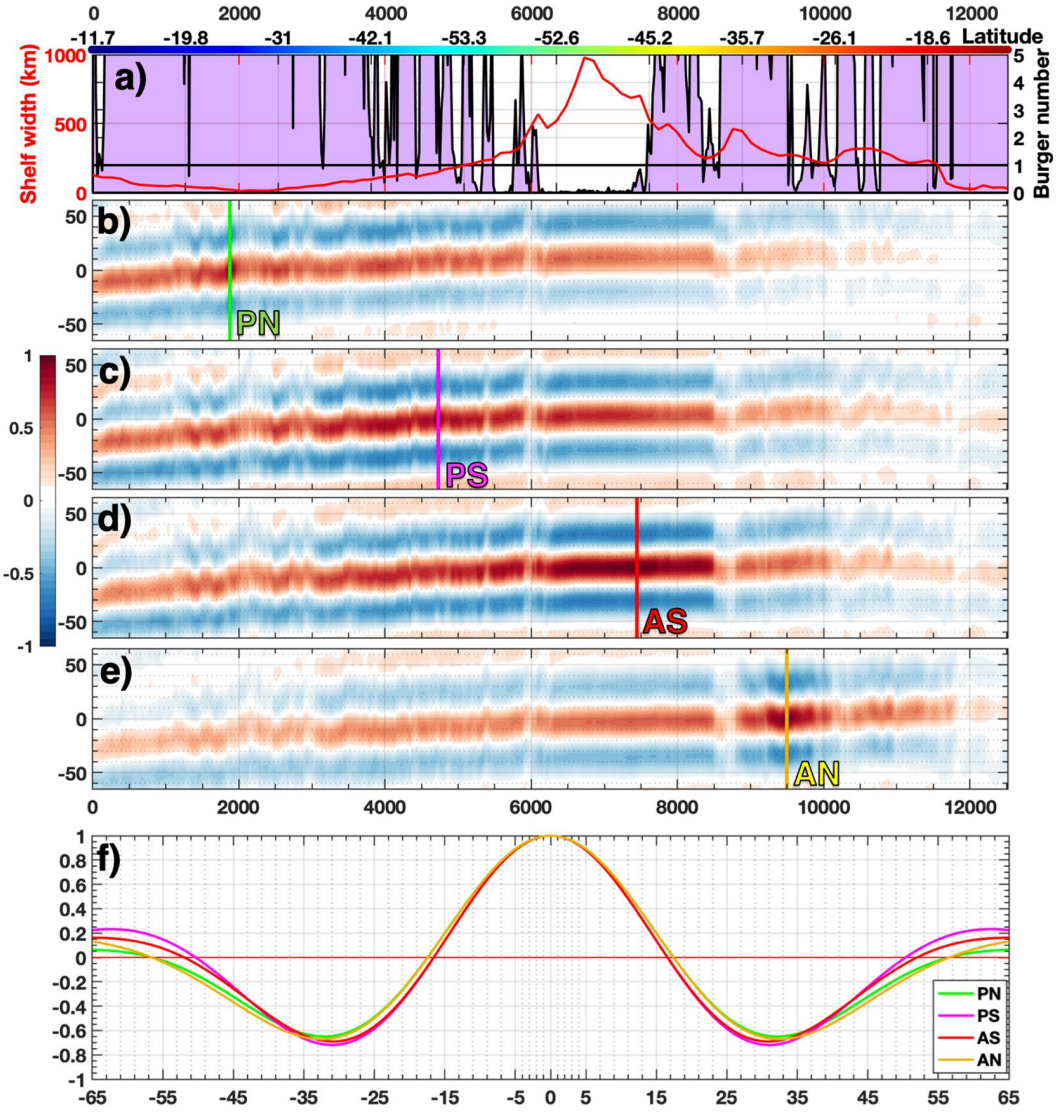

Figure 6. (a) Mean Burger number along the track in purple shade (black Y-axis on the right). Black line is Bu = 1. Red curve is shelf width in kilometer along the track (left red Y-axis). The colorbar indicates distance and latitude along the track as in Figure 3a. (b) Lag correlation diagram between SLA along the track and SLA at PN (27-year-long time series). (c) Same as b for SLA at PS. (d) Same as b for SLA at AS. (e) Same as b for SLA at AN. Only significant correlations are colored. A linear fit of maximum correlations provide estimates of the phase velocities. (f) Lagged correlations for each section (PN, PS, AS, and AN). X-axis is lag in days and y-axis correlation coefficient. 95% confidence level is 0.1. All SLA time series were band-pass filtered between 40 and 130 days.

We produce lagged correlation-distance diagram between 40 and 130 day filtered SLA along the track and MJO OOMI index (PC1; Section 2.3) over the 27 years (Figure 8).

The correlations are significant, large (absolute value of $r \geq 0.3$) and coherent with the propagative patterns observed in Figure 6 (same phase speeds and periods). The maximum correlations are obtained at lag 30 days at EP (−10°S), lag 43 days at PN, lag 56 days at PS and lag 60 days at AS and lag 63 days at AN. The lagged correlations suggest that the MJO plays a major role in forcing the waves propagating around South America. However, intensification and generation observed in particular at PS and AN (Figure 6), hint at local processes. We explore the role of local wind in the following section.

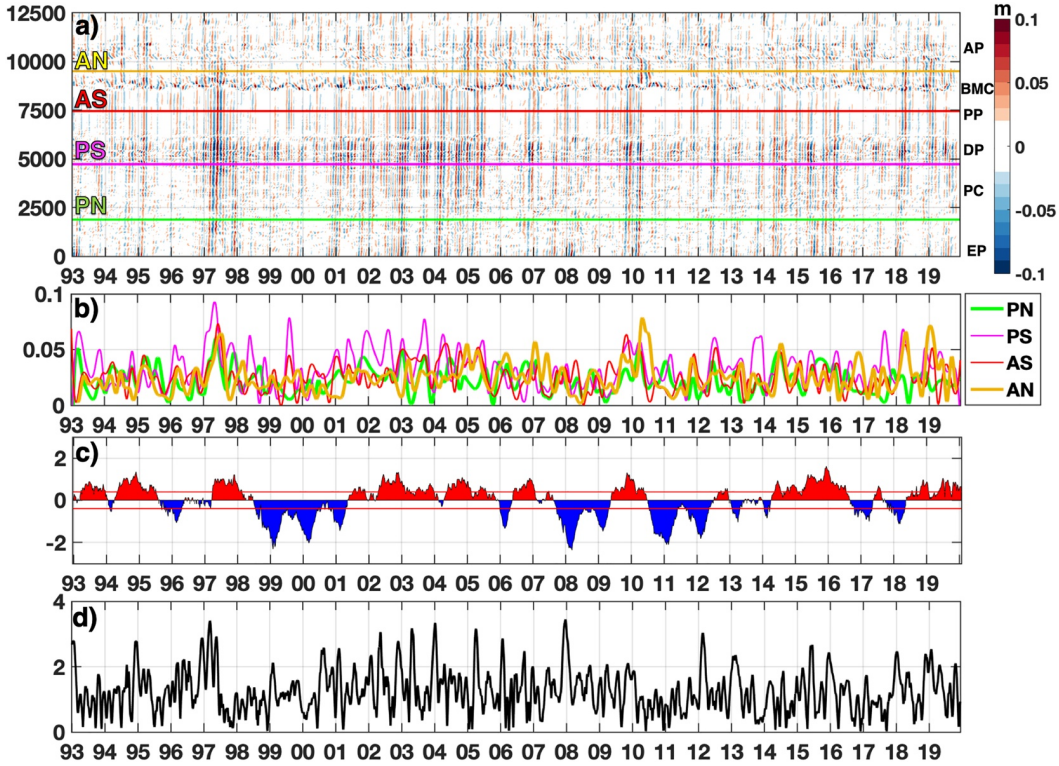

Figure 7. (a) Distance-time diagram of 40–130 days band-pass filtered sea level anomalies along the track following the 300 m isobath for the 1993–2019 period from GLORYS12. X-axis is time in years, Y-axis is distance along the track in kilometer. Color bar is SLA in meter. The four sections are indicated. (b) Envelope of filtered SLA amplitude at the location of the four sections in meter. (c) Detrended SST anomalies from El Niño 3.4 (in °C). (d) Original OLR Madden-Julian Index Amplitude (normalized – see Section 2.3).

4.2. Wind Forcing

Regression maps of the band-pass filtered SLA averaged around the southern tip of South America onto wind components were performed at many lags. Only regressions with the meridional component show conclusive results. Indeed, the regression maps of the band-pass filtered SLA averaged around the southern tip of South America onto the meridional component of the wind show a distinctive negative pattern (above 99% CL) around South America from lag −10 to 5 days. This pattern, maximum at lag −10 days (Figures 9a and 9b), moves westward and attenuates at lag 5 days (not shown).

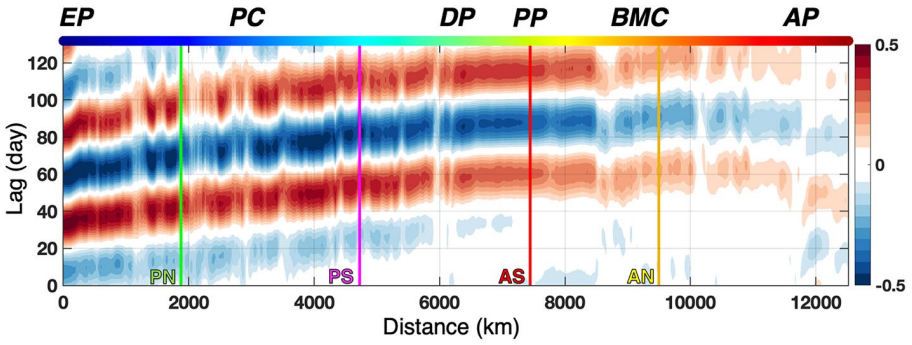

Figure 8. Lagged correlation-distance diagram between 40 and 130 day filtered SLA along the track following the 300 m isobath and MJO OOMI index (PC1) computed over 27 years (1993–2019). Y-axis is lag in days, X-axis is distance along the track in kilometer. The upper colorbar indicate the position along the track as in Figure 1a. PN, PS, AS, and AN locations are marked with vertical color lines.

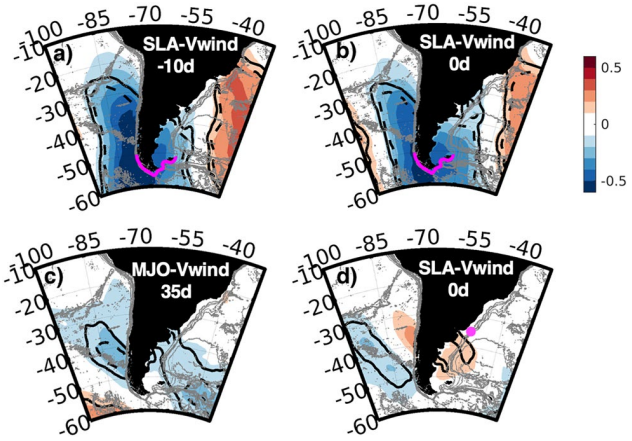

Figure 9. (a) Regression map of the band-pass filtered SLA averaged along the magenta line (around the southern tip of South America) onto the meridional component of the wind at lag −10 days. (b) Same as (a) for lag 0 days. (c) Regression map of MJO OOMI (PC1) index onto the meridional component of the wind for lag +35 days. (d) Regression map of the band-pass filtered SLA at the magenta dot (north of the BMC) onto the meridional component of the wind at lag 0 days. The thick (dashed) black lines are the 99 (95)% confidence level. Color scale in m/s.

This negative pattern corresponds to northerly winds which, through Ekman transport, increase the positive SLA signal along the Pacific coast and decrease the positive SLA on the Atlantic side. Thus the local meridional winds reinforce the wave amplitude on the Pacific side and reduce it on the Atlantic side. This explains why the observed SLA signal is stronger at PS than AS (Figure 7). Interestingly, the negative wind pattern shows up in the regression between the MJO and the meridional component of the wind at lag 35 days (Figure 9c). This suggests that the MJO forces TWs in two ways: through an oceanic connection implying equatorial Kelvin waves reaching PN at lag 43 days (Figure 8) and trough an atmospheric teleconnection enhancing northerly winds at lag 35 days and contributing to the reinforcement or generation of TWs along the southern Pacific coast. This implies that the atmospheric teleconnection reaches PS before the oceanic one. Most of TWs manage to cross the BMC and attenuate downstream (Figure 7a). As mentioned in the previous section, some waves seem to be locally generated at the confluence (Figure 6e). We therefore explore possible local wind forcing. The regression maps of the band-pass filtered SLA averaged north of the BMC (pink line at 35°S in Figure 9d) show a positive (southerly) wind pattern at lag 0 located at the confluence. This southerly wind could possibly force the TWs only observed north of the confluence in the Hovmöller diagram in Figure 7.

4.3. Wave Vertical Structure and Influence on the Mean Flow

The mean flow on the Pacific slope shows a rather baroclinic structure (PN and PS) with weak southward currents (core of 0.1 m/s; Figure 10, upper two panels of the first column). In contrast, the strong MC flows along the Patagonian slope with a barotropic equivalent structure and is organized in two jets with mean cores velocities of 0.2 m/s and 0.6 m/s at AS (Artana et al., 2021). Further North, at AN, the flow shows a baroclinic structure with mean southward surface velocities of 0.3 m/s of the Brazil Current above a northward flow at 700 m (Figure 10, lower two panels of the first column).

To explore the vertical structure of the waves, we produced composites of filtered along-shore velocity anomalies (40–130 days) at the four sections corresponding to the positive phase of the waves (Figure 10, second column). The events are selected from dates when the filtered SLA is larger than two standard deviation at the 300 m isobath of each section. We applied the same procedure to compute the composite of the along-shore velocity anomalies corresponding to the negative phase of the waves (not shown) selected from dates with SLA lower than minus two standard deviations. These criteria selected 22, 23, 19, and 29 positive events and 25, 25, 24, and 18 negative events for PN, PS, AS, and AN, respectively. The composites of along-shore velocity anomalies of positive events and negative events feature similar patterns of opposite sign (not shown), suggesting that the criteria selected positive and negative phase of the waves.

The along-shore velocity anomaly composites feature a rather baroclinic structure at PN, PS, and AN and a barotropic structure at AS (Figure 10 second column). The associated velocity anomalies reach 0.1 m/s on the Pacific slope, decrease at AS ($\leq$0.05 m/s) and intensify to the north at AN ($\geq$0.15 m/s).

In their positive phase, the waves strengthen the rather weak southward surface mean flow at PN and at PS (from 0.05 m/s to 0.2 m/s), intensify the onshore jet of the MC current (between 0 and 100 km, from) at AS, and enhance the subsurface northward jet (between 50 and 100 km) at AN (Figure 10, third column).

Although Brink's model is too idealistic (e.g., Brunner et al., 2019) and requires several assumptions such as a straight coastline with similar slope bathymetry, which are not fulfilled along the path, it provided guidance to the interpretation of those waves. The spatial structures of the velocity composites are reminiscent of the theoretical modes (obtained with the Brink and Chapman toolbox - appendix): modes 1–2 for the Pacific side, 2–3 at the AS and modes 1–2 at AN (Figure 10, second column). As mentioned before, dispersion curves for modes 1, 2, and 3 provided theoretical phase speed that match the observed ones (ranging between 1.2 m/s and 2.4 m/s on the Pacific slope and between 1 and 7 m/s on the Atlantic slope, Figure 4).

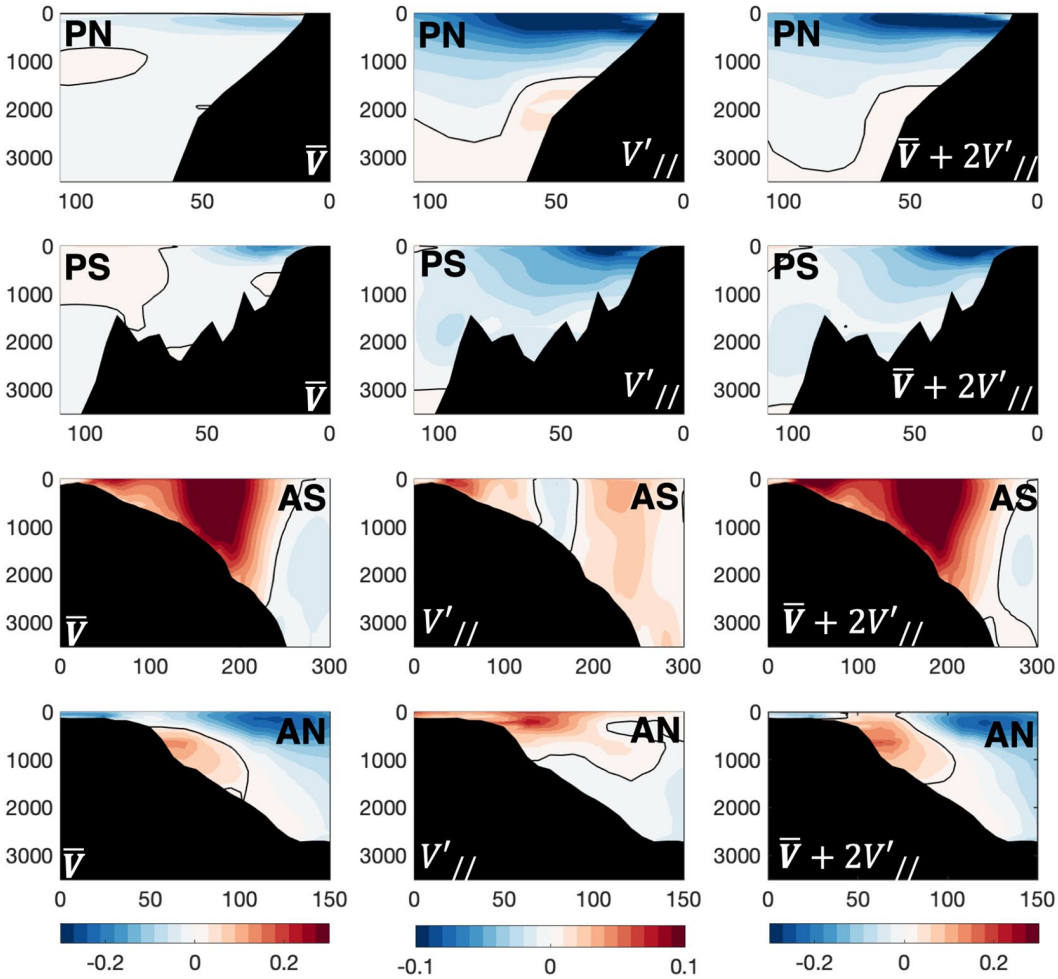

Figure 10. Left panels: 27-year mean along-shore velocities at the four sections. Central panels: composites of filtered along-shore velocity anomalies for the positive phase of the waves at the four sections PN, PS, AS, and AN. The composites are built from events selected when the SLA peak is larger than two standard deviations. Right panels: Along-shore velocities corresponding to positive phase of the waves (mean plus twice the anomalies). Scales in m/s.

5. Summary and Discussion

Sea level anomalies from GLORYS12 reanalysis reproduced well the signal measured by tide gauges around South America. The reanalysis better match the tide gauges signal than satellite altimetry data product which features blurred patterns (Figure 2). The 27-year-long global ocean reanalysis GLORYS12 documented waves with wavelengths between 8,000 and 12,000 km (Figure 5) and periods of 40, 50, 60, 70, and 110 days (Figure 3) propagating from the EP to the Tropical Atlantic (22°S) around South America (red arrows in Figure 11). The AP at 22°S is a hotspot for wave energy dissipation (Freitas et al., 2021).

Propagation speeds range from 1.8 to 2.8 m/s along the Pacific continental slope and from 1.8 to 7 m/s along the Atlantic slope. As predicted by theory, phase speeds are larger along the Patagonian Platform (5–7 m/s) as the shelf width is large and the Burger number small (Figures 4b and 6a). During their propagation, the waves encounter distinct background characteristics which affect their vertical structures. Indeed, on the Pacific side and off Brazil (PS, PN and AN) the waves have a baroclinic structure, whereas the structure is rather barotropic at AS. The phase speeds and the spatial structures across the slope at PN, PS, and AN correspond to theoretical modes 1–2 and to mode 2–3 at AS (Figures 10 and 4).

The MJO, through oceanic and atmospheric teleconnections, plays a key role in forcing the TWs. On one hand, the MJO forces Equatorial Kelvin waves that propagate to the east and reach the coast after 35 days. They trig-

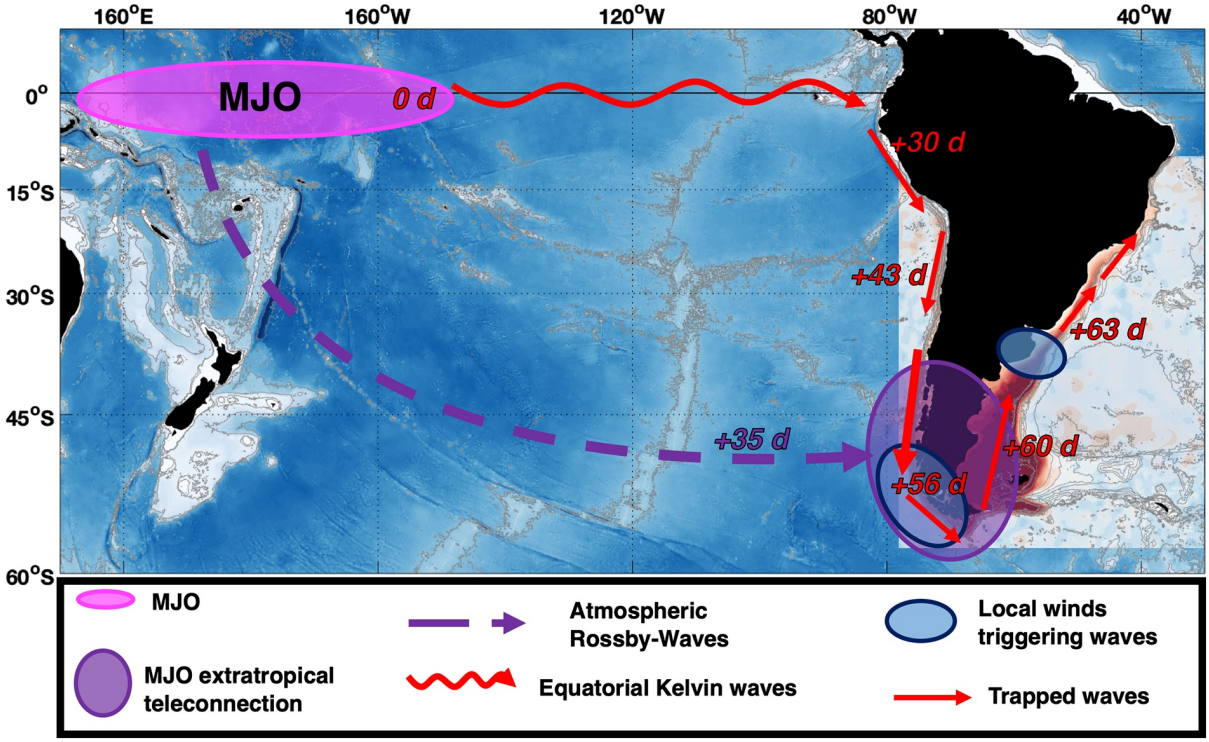

Figure 11. Schematics of mechanisms forcing trapped waves around South America. MJO is a key player in triggering trapped waves around South America through equatorial oceanic Kelvin waves (red) and atmospheric Rossby waves (dashed purple line). Lags (red) in days are deduced from the correlation between the MJO and the SLA over the track following the 300 m isobath. Lag in days (purple) are deduced from the regression between meridional winds and the MJO index, the associated wind signal is represented with the purple circle. Moreover, local wind forcing (in blue), not linked with the MJO, reinforce and/or generate trapped waves. For sake of illustration we superimposed the correlation at lag 0 days shown in Figure 5.

ger TWs that propagates poleward reaching PN 8 days later (lag 43 days with respect to MJO) and PS 21 days later (lag 56 days; Figure 8, red lines in Figure 11). This result is consistent with previous studies (e.g., Cravatte et al., 2003; Hendon et al., 1998; Illig et al., 2018; Roundy & Kiladis, 2006). On the other hand, the MJO also modulates TWs through an atmospheric teleconnection that reaches PS at lag 35 days (before the arrival of the oceanic teleconnection). Indeed the MJO trigger atmospheric Rossby waves that generate local wind anomalies over the southern tip of South America (purple dashed line in Figure 11; Berbery & Nogues-Paegle, 1993). The local wind anomaly pattern increases the wave amplitude at PS and decreases it at AS. The increasing in wave amplitude at PS could also be the consequence of topographic effects or wave reflection on the bottom.

The MJO amplitude is enhanced before El-Niño episodes. Trapped wave activity is larger before and during positive ENSO phases and ENSO seems to modulate the wave activity at low frequency (Figure 7). However, the linkage between MJO and ENSO is still controversial (e.g., Dewitte et al., 2007, 2008) and is out of the scope of this paper.

Trapped waves are also intermittently forced by local winds not necessarily related with the MJO, at specific locations such as Southern Chile and the BMC (blue circles in Figure 11).

Trapped waves impact the along-shore currents: during the positive phase of the waves the flow is enhanced by about 0.1 m/s at PN, PS, AS, and AN. The waves modulate the intensity of the MC inner jet at AS as discussed in Poli et al. (2020). At AN the mean flow exhibits a subsurface equatorward counter current, which is intensified and reaches the surface during the positive phase of the wave. The subsurface current deserves further study. The impact of the TWs on cross-shore, vertical velocities and other fields such as temperature or Chlorophyll-a are under investigation.

Appendix A: Trapped Waves Along Cross-Sections Around South America From Linear Theory

We compute TWs properties at the four sections located at 25°S (PN) and 50°S (PS) along the Pacific side and at 47°S (AS) and 31°S (AN) along the Atlantic side (Figure 3) using Brink's and Chapman toolbox (Brink, 2018). Following Poli et al. (2020), we used GLORYS12 outputs to estimate mean Brunt-Vaïsälä frequency and mean flow along the sections. Mean flows are shown in Figure 10. The mean flow along the Pacific side was small and neglected, while the "idealized" Brazil Current at AN comprised a southward jet and the Malvinas Current at AS comprised two jets (cf. figure A1 in Poli et al., 2020). The first three gravest modes shows structures highly dependent on Burger number (Section 3.1) and the slope steepness plays a major role (Figure A1). PN, PS, and AN modal structures present baroclinic characteristics, while AS modal structures are more barotropic. The dispersion curves are presented in Figure 4 of Section 3 and show faster velocities for barotropic-like modal structures than for the baroclinic ones.

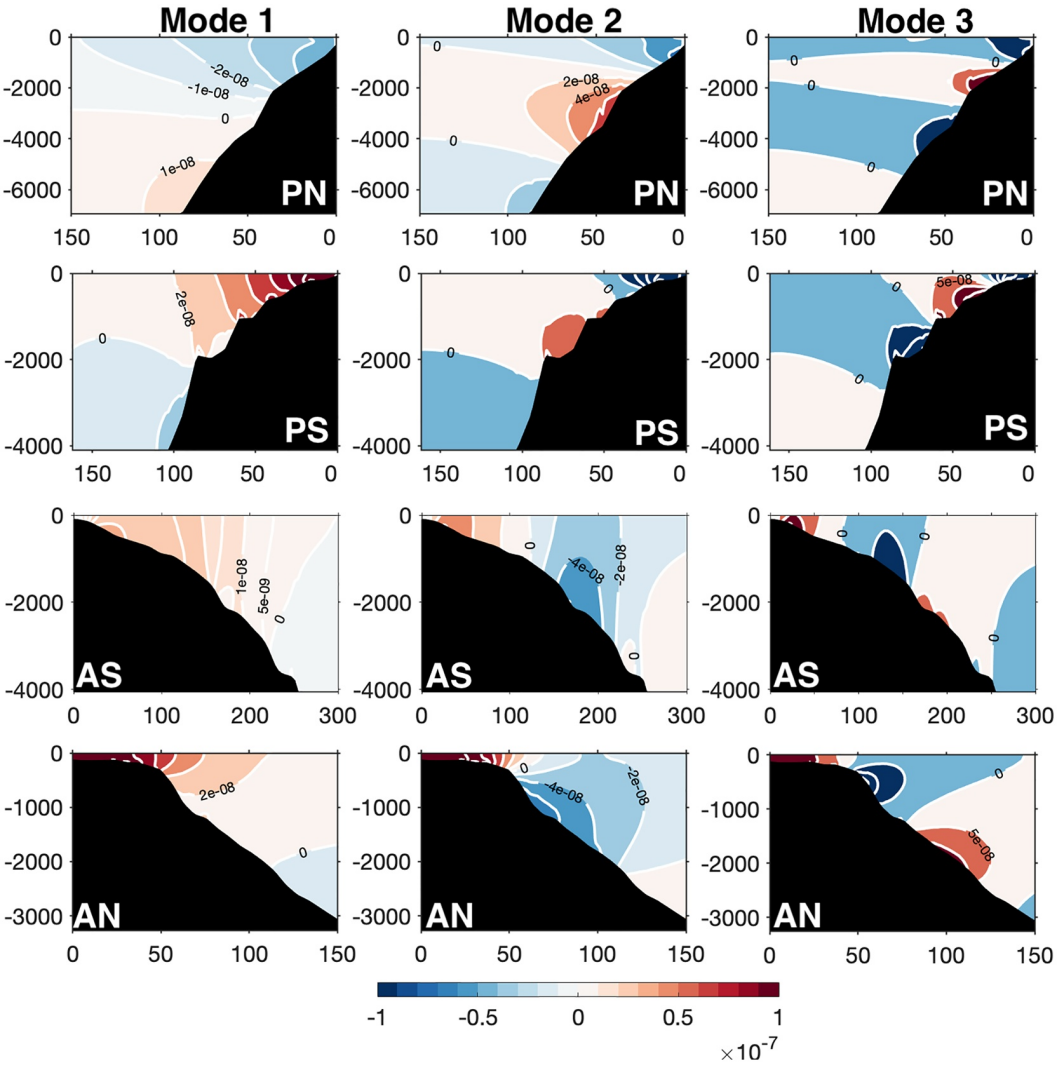

Figure A1. First three gravest mode computed with Brink and Chapman toolbox along the four sections.

Conflict of Interest

The authors declare no conflicts of interest relevant to this study.

Data Availability Statement

The satellite data and model outputs are available at Copernicus Marine Environment Monitoring Service (CMEMS; https://marine.copernicus.eu). ERA-Interim outputs are available at https://www.ecmwf.int/en/forecasts/datasets/reanalysis-datasets/era-interim. The climatic index are available at https://psl.noaa.gov/data/correlation/nina34. data for ENSO and at https://psl.noaa.gov/mjo/mjoindex/ for the MJO. Tide gauge data are available at http://uhslc.soest.hawaii.edu/data/.

Acknowledgments
We thank Jean-Michel Lellouche for his advice and help. We are grateful to CNES (Centre National d'Etudes Spatiales) for constant support. This study is a contribution to the CNES-funded BACI project. Léa Poli acknowledges support from Sorbonne Université and Camila Artana a CNES Postdoc Scholarship.

References

Artana, C., Lellouche, J.-M., Park, Y.-H., Garric, G., Koenig, Z., Sennéchael, N., et al. (2018). Fronts of the Malvinas current system: Surface and subsurface expressions revealed by satellite altimetry, Argo floats, and Mercator operational model outputs. *Journal of Geophysical Research: Oceans*, *123*, 5261–5285. https://doi.org/10.1029/2018JC013887

Artana, C., Provost, C., Lellouche, J.-M., Rio, M.-H., Ferrari, R., & Sennéchael, N. (2019). The Malvinas Current at the confluence with the Brazil Current: Inferences from 25 years of Mercator Ocean reanalysis. *Journal of Geophysical Research: Oceans*, *124*, 7178–7200. https://doi.org/10.1029/2019JC015289

Artana, C., Provost, C., Poli, L., Ferrari, R., & Lellouche, J.-M. (2021). Revisiting the Malvinas Current upper circulation and water masses using a high-resolution ocean reanalysis. *Journal of Geophysical Research: Oceans*, *126*, e2021JC017271. https://doi.org/10.1029/2021JC017271

Ballarotta, M., Ubelmann, C., Pujol, M. I., Taburet, G., Fournier, F., Legeais, J. F., et al. (2019). On the resolutions of ocean altimetry maps. *Ocean Science*, *15*(4), 1091–1109. https://doi.org/10.5194/os-15-1091-2019

Berbery, E. H., & Nogues-Paegle, J. (1993). Intraseasonal interactions between the tropics and extratropics in the southern hemisphere. *Journal of Atmospheric Science*, *50*, 1950–1965. https://doi.org/10.1175/1520-0469(1993)050<1950:IIBTTA>2.0.CO;2

Brink, K. H. (1982). A comparison of long coastal trapped wave theory with observations off Peru. *Journal of Physical Oceanography*, *12*, 897–913.

Brink, K. H. (2018). *Stable coastal-trapped waves with stratification, topography and mean flow*. https://hdl.handle.net/1912/10527

Brunner, K., Rivas, D., & Lwiza, K. M. M. (2019). Application of classical coastal trapped wave theory to high scattering regions. *Journal of Physical Oceanography*, *49*, 2201–2216. https://doi.org/10.1175/JPO-D-18-0112.1

Clarke, A. (1992). Low-frequency reflection from a non-meridional eastern ocean boundary and the use of coastal sea level to monitor eastern Pacific equatorial Kelvin waves. *Journal of Physical Oceanography*, *22*(2), 163–183.

Clarke, A., & Ahmed, R. (1999). Dynamics of remotely forced intraseasonal oscillations off the western coast of South America. *Journal of Physical Oceanography*, *29*(2), 240–258.

Clarke, A. J., & Shi, C. (1991). Critical frequencies at ocean boundaries. *Journal of Geophysical Research*, *96*(C6), 10731–10738. https://doi.org/10.1029/91JC00933

Combes, V., & Matano, R. P. (2019). On the origins of the low-frequency sea surface height variability of the Patagonia shelf region. *Ocean Modelling*, *142*, 101454. https://doi.org/10.1016/j.ocemod.2019.101454

Conejero, C., Dewitte, B., Garçon, V., Sudre, J. & Montes, I. (2020). ENSO diversity driving low-frequency change in mesoscale activity off Peru and Chile. *Scientific Reports*, *10*, 17902.

Cravatte, S., Picaut, J., & Eldin, G. (2003). Second and first baroclinic Kelvin modes in the equatorial Pacific at intraseasonal time scales. *Journal of Geophysical Research*, *108*, 3266. https://doi.org/10.1029/2002JC001511

Dee, D. P., Uppala, S. M., Simmons, A. J., Berrisford, P., Poli, P., Kobayashi, S., et al. (2011). The ERA-interim reanalysis: Configuration and performance of the data assimilation system. *Quaterly Journal of the Royal Meteorological Society*, *137*, 553–597. https://doi.org/10.1002/qj.828

Dewitte, B., Cibot, C., Périgaud, C., An, S. I., & Terray, L. (2007). Interaction between near-annual and ENSO modes in a CGCM simulation: Role of the equatorial background mean state. *Journal of Climate*, *20*(6), 1035–1052. https://doi.org/10.1175/JCLI4060.1

Dewitte, B., Purca, S., Illig, S., Renault, L., & Giese, B. (2008). Low frequency modulation of the intraseasonal equatorial Kelvin wave activity in the Pacific Ocean from SODA: 1958-2001. *Journal of Climate*, *21*, 6060–6069.

Freitas, P. P., Paiva, A. M., Cirano, M., Mill, G. N., Costa, V. S., Gabioux, M., & França, B. R. L. (2021). Coastal trapped waves propagation along the Southwestern Atlantic Continental Shelf. *Continental Shelf Research*. https://doi.org/10.1016/j.csr.2021.104496

Hendon, H. H., Liebmann, B., & Glick, J. D. (1998). Oceanic Kelvin waves and the Madden–Julian oscillation. *Journal of Atmospheric Science*, *55*, 88–101.

Hughes, C. W., & Meredith, M. P. (2006). Coherent sea-level fluctuations along the global continental slope. *Philosophical Transactions of the Royal Society A*, *364*, 885–901. https://doi.org/10.1098/rsta.2006.1744

Huthnance, J. M. (1978). On coastal trapped waves: Analysis and numerical calculation by inverse iteration. *Journal of Physical Oceanography*, *8*, 74–92.

Illig, S., Bachelery, M.-L., & Cadier, E. (2018). Subseasonal coastal-trapped wave propagations in the southeastern Pacific and Atlantic Oceans: 2. Wave characteristics and connection with the equatorial variability. *Journal of Geophysical Research: Oceans*, *123*, 3942–3961. https://doi.org/10.1029/2017JC013540

Kessler, W., McPhaden, M., & Weickmann, K. (1995). Forcing of intra-seasonal Kelvin waves in the equatorial Pacific. *Journal of Geophysical Research*, *100*(C6), 10613–10631.

Kessler, W. S., & Kleeman, R. (2000). Rectification of the Madden–Julian oscillation into the ENSO cycle. *Journal of Climate*, *13*, 3560–3575.

Kiladis, G. N., Dias, J., Straub, K. H., Wheeler, M. C., Tulich, S. N., Kikuchi, K., et al. (2014). A comparison of OLR and circulation based indices for tracking the MJO. *Monthly Weather Review*, *142*, 1697–1715.

Lellouche, J.-M., Greiner, E., Bourdallé-Badie, R., Garric, G., Melet, A., Drévillon, M., et al. (2021). The Copernicus global 1/12° Oceanic and sea ice GLORYS12 Reanalysis. *Frontiers of Earth Science*. https://doi.org/10.3389/feart.2021.698876

Madden, R. A., & Julian, P. R. (1994). Observations of the 40–50-day tropical oscillation—A review. *Monthly Weather Review*, *122*, 814–837.

McPhaden, M. J. F. (1999). Genesis and evolution of the 1997-98 El Niño. *Science*. https://doi.org/10.1126/science.283.5404.950

Pizarro, O., Clarke, A. J., & Van Gorder, S. (2001). El Niño sea level and currents along the South American coast: Comparison of observations with theory. *Journal of Physical Oceanography*, *31*(7), 1891–1903.

Poli, L., Artana, C., Provost, C., Sirven, J., Sennéchael, N., Cuypers, Y., & Lellouche, J.-M. (2020). Anatomy of subinertial waves along the Patagonian shelf break in a 1/12 global operational model. *Journal of Geophysical Research: Oceans*. https://doi.org/10.1029/2020JC016549

Pujol, M.-I., Fauge're, Y., Taburet, G., Dupuy, S., Pelloquin, C., Ablain, M., & Picot, N. (2016). Duacs DT2014: The new multi-mission altimeter data set reprocessed over 20 years. *Ocean Science*, *12*, 1067–1090. https://doi.org/10.5194/os-12-1067-2016

Roundy, P. E., & Kiladis, G. N. (2006). Observed relationship between oceanic Kelvin waves and atmospheric forcing. *Journal of Climate*, *19*, 5253–5272. https://doi.org/10.1175/JCLI3893.1

Sprintall, J., Cravatte, S., Dewitte, B., Du, Y., & Sen Gupta, A. (2020). Oceanic teleconnections. In M. J. McPhaden, A. Santoso, & W. Cai (Eds.), *El Niño in a changing climate*. Wiley. Chapter 15.

Strub, P. T., James, C., Montecino, V., Rutllant, J. A., & Blanco, J. L. (2019). Ocean circulation along the Southern Chile transition region (38°–46°S): Mean, seasonal and interannual variability, with a focus on 2014–2016, 2019. *Progress in Oceaongraphy*, *172*, 159–198. https://doi.org/10.1016/j.pocean.2019.01.004

Vivier, F., Provost, C., & Meredith, M. (2001). Remote and local forcing in the Brazil Malvinas Region. *Journal of Physical Oceanography*, *31*, 892–913. https://doi.org/10.1175/1520-0485

Chapter 4

Collapses, maxima, multi-year modulation and trends of the Zapiola anticyclone: insights from Mercator Reanalysis.

Collapses, maxima, multi-year modulation and trends of the Zapiola Anticyclonic Circulation: insights from Mercator Reanalysis.

Lea Poli[1], Camila Artana[2], Christine Provost[1], Jérôme Sirven[1], and Ruben Le Blanc-Pressenda[1]

[1]LOCEAN-IPSL, Sorbonne Université (UPMC), Paris, France

[2]Institut de Ciences del Mar, Barcelona, Spain

Key Points:

- The Zapiola circulation is bottom intensified and its volume transport ranges from −18.5 Sv to 268 Sv with a mean of 122 Sv.
- We analyse collapses, maxima, multi-year modulation and trends in the Zapiola transport and associated water characteristics variations.
- In the last 27 years trends in the Zapiola region include transport reduction and increase in temperature and salinity in the upper 2000 m.

Corresponding author: Lea Poli, lea.poli@locean.ipsl.fr

Abstract

The Argentine Basin hosts a unique oceanic feature: the Zapiola Anticyclonic Circulation (ZAC) located above a sedimentary deposit. Taking advantage of a high-resolution ($1/12^{o}$) global ocean reanalysis (GLORYS12) we examine the ZAC over 27 years (1993-2019). The mean ZAC is bottom-intensified with bottom currents reaching $0.10ms^{-1}$. The ZAC volume transport ranges from -18.5 Sv to 268 Sv with a mean of 122 Sv. The strong negative peaks correspond to occasional ZAC collapses. During large transport events (>195.4 Sv) the ZAC shows a well defined coherent gyre. Strong transport events are associated with high eddy kinetic energy (EKE) at the periphery of the ZAC (especially to the west and south). In contrast, during weak transport events (<49.8 Sv), EKE increases at the center of the ZAC and decreases at the ZAC periphery. A weak ZAC is more permeable to external mesoscale structures. Each weak event features a cyclonic eddy at the center of the ZAC carrying subantarctic cold and fresh waters. The ZAC exhibits a multi-year modulation, with periods of 4-5 years (1993-1997, 1998-2003 and 2004-2009) of low salinity corresponding to low transport, and high salinity to high transport. Over the last 27 years, transport time series exhibit a significant negative trend of -15 Sv.$decade^{-1}$ associated with a negative trend in EKE (-0.015 (m/s)^2.$decade^{-1}$) to the north west of the ZAC. Waters in the Zapiola region become warmer and saltier in the first 2000 m of the water column because of the southward migration of the subtropical front.

Plain Language Summary

In the southwest Atlantic, the Argentine Basin hosts a unique oceanic feature: the Zapiola Anticyclonic Circulation located above a sedimentary deposit. The Zapiola Anticyclonic Circulation rotates counter-clockwise and has a mean transport comparable to those of the strongest ocean currents (122 million cubic meters per second). The Zapiola Anticyclonic Circulation undergoes extreme variations with collapses and intensifications reaching 300 million cubic meters per second. Episodes of weak Zapiola transport tend to occur in

austral winter and episodes of strong transport in austral summer. The Zapiola Anticyclonic Circulation exhibits a multi-year modulation, with periods of 4-5 years (1993-1997, 1998-2003 and 2004-2009) of low salinity corresponding to low transport, and high salinity to high transport. Over the last 27 years, the Zapiola Anticyclonic Circulation transport diminished and waters in the region became warmer and saltier in the upper 2000 m of the water column.

1 Introduction

The Argentine Basin is one of the most energetic regions of the world ocean in terms of mean flow and mesoscale activity (Mason et al., 2017). The spatial distribution of surface Eddy Kinetic Energy (hereafter EKE) maxima form a C-shape around a relative minimum (values lower than 0.01 m^2s^{-2}) in the center of the basin (Figure 1). This minimum is associated with a particular oceanic feature, the Zapiola Anticyclonic Circulation (hereafter ZAC). The ZAC is located above a sedimentary deposit (the Zapiola Rise, centered at 45°W, 45°S).

The ZAC existence was first suggested from photographed mud waves (Flood and Shor, 1988). The current measurements that followed (Whitworth et al., 1991; Weatherly, 1993) supported the concept of an anticyclonic circulation. Subsequently, Saunders and King (1995) made the first measurements in the ZAC from a shipborne ADCP system and hydrographic measurements. They measured a synoptic intensified flow at depth and suggested the presence of a barotropic anticyclonic circulation with a transport equivalent to that of the strongest ocean currents (> 100 Sv). Mean transport estimates were then produced and cover a wide range of values. A mean transport of 50 Sv was obtained using altimetry-derived surface geostrophic velocities over the period 1993-2007 under batotropic flow assumption (Saraceno et al., 2009). Colin de Verdière and Ollitrault, (2016) used an ocean climatology combined with 1000-m Argo velocities to estimate the full-depth streamfunction over the period 2004-2010 which led to a larger mean transport of 124 Sv. Recently, Johnson and King (2023) estimated a mean ZAC transport of 110 Sv by referencing geostrophic shear from mean climatology (World Ocean Atlas 2018) to mean 1000-dbar velocities that they estimated from Argo float displacements and highlighted the bottom-intensified nature of the ZAC.

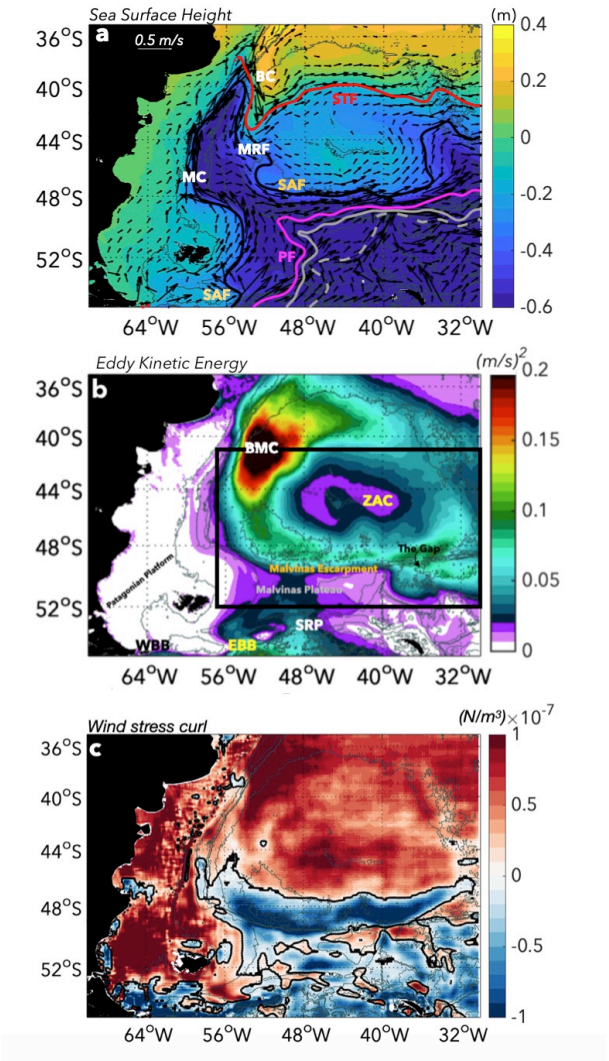

Figure 1: a) Mean sea surface height (in m) and mean surface velocities (arrows).b) Mean surface eddy kinetic energy. The fields from GLORYS12 reanalysis are averaged over 1993-2019 period. Sea surface height contours indicate the front positions in panel a: Subantarctic Front (SAF, black isoline −0.38 m), Northern Polar Front (PF-N, magenta isoline −0.77 m), Main Polar Front (PF-M, thick grey isoline −0.91 m), Southern Polar Front (PF-S, dashed grey isoline −1.05 m) and Subtropical Front (STF, red isoline −0.13 m).In b, EBB stands for East of Burdwood Bank, WBB for West of Burdwood Bank, SRP for Shag Rock Passage, Zapiola Anticyclonic Circulation (ZAC) and the Brazil-Malvinas Confluence (BMC). The black rectangle shows the region plotted in c-d in figure 2. c) Mean Wind Stress Curl from ERA-interim reanalysis averaged over the period 1993-2019.

According to theoretical models, the eddy-rich region surrounding the Zapiola Rise (Figure 1b) leads to downslope transport of potential vorticity, associated with an upslope mass transport. This convergence generates a high pressure dome which induces a geostrophic

circulation (Dewar, 1998). Bottom drag controls the flow. The convergent mass transport is compensated by a divergent Ekman transport in the bottom boundary layer (de Miranda et al., 1999; Volkov and Fu., 2008). Using numerical simulations, Weijer et al. [2015; 2020] showed that this secondary circulation leads to a strong downward vertical transport (of about 4 Sv) above the rise and they estimated a time of water mass retention of 1.5 years within the ZAC . Using satellite altimetry data, several studies pointed out the high variability of the ZAC at different time scales; intraseasonal modes of variability with periods of 20-25 days have been described by Fu et al. [2001], Weijer et al. [2007], Hughes et al. [2007] and Yu et al. [2018]. Strong interannual variability has been evidenced by Fu et al. [2001], Volkov and Fu. [2008], Saraceno et al. [2009] and Venaille et al., [2011]. Occasional collapses of the ZAC circulation have been suggested (Saraceno et al., 2009, Bigorre, 2005). To the west of the Basin, a maximum of EKE centered at 40°S (with values exceeding 0.2 m^2s^{-2}, Figure 1b) is associated with the confluence of two strong western boundary currents: the Malvinas Current (MC) and the Brazil Current (BC) (Figure 1a). The MC which is associated with the Antarctic Circumpolar Current (ACC), flows northward following the Subantarctic Front (SAF) with surface velocities reaching 60 cm/s and a mean volume transport peaking at 37 Sv at 41°S (Artana et al., 2021). At 38°S the MC encounters the BC that flows southward (23 Sv at 36°S, Artana et al., 2021) forming the Brazil-Malvinas confluence (BMC). Those currents transport highly contrasted waters – fresh and cold for the MC, salty and warm for the BC. The BC bounded by the the Subtropical Front (STF) leaves the continental slope at about 38°S, that is nearly 15° north of the zero isoline in the mean Wind Stress Curl (Figure 1c). After the collision of the two currents, a part of the BC overshoots southward to about 45°S (known as BC overshoot, BCO) before bending back to the north (Figure 1a). The MC retroflects cyclonically toward the south, flowing side by side with the BC overshoot as the Malvinas Return Flow (MRF)(Figure 1a).

Measurements being still scarce in the Argentine Basin and particularly in the Zapiola region, we take advantage of a 27-year global reanalysis simulation from Mercator to further investigate ZAC circulation from surface to bottom and the water characteristics. After

presenting the data and methods in section 2, we examine long-term trends, multi-year modulations and extreme events of the ZAC transport (section 3) and associated hydrographic properties (section 4). In section 5 we discuss the role of EKE and Wind Stress Curl in shaping those variations. In section 6, we summarize and conclude.

2 Operational model and data

2.1 Mercator Models

We used the high-resolution global Mercator Ocean reanalysis (hereafter GLORYS12) and the real-time global high-resolution forecasting system (hereafter PSY4) from Copernicus Marine Environment Monitoring Service (CMEMS, `http://marine.copernicus.eu/` ; see Lellouche et al., 2021 for GLORYS12, and Lellouche et al., 2018 for PSY4). GLORYS12 covers the period from 1993 to 2019 and PSY4 from 2007 to present. The dynamical core of GLORYS12 and PSY4 is the NEMO (Nucleus for European Modelling of the Ocean) platform (Madec, 2008). The models provide daily outputs, with a horizontal resolution of 1/12° and 50 vertical levels, with the spacing increasing with depth (22 levels are within the first 100 m leading to a vertical resolution of 1 m in the upper levels and 450 m at 5,000 m depth). Both models are forced by surface atmospheric fields from the European Center for Medium-Range Weather Forecasts (by ERA-Interim reanalysis for GLORYS12 and by the Integrated Forecasting System (IFS) for PSY4). The models assimilate along-track satellite altimetry data, satellite sea surface temperature, sea-ice concentration, and in-situ temperature and salinity profiles using a reduced-order Kalman filter with a 3-D multivariate modal decomposition of the background error and a 7-day assimilation cycle (Lellouche et al., 2021; Lellouche et al., 2018). One important impact of data assimilation is to counter the tendency of ocean models to drift away from reality. Reanalyses provide a dynamically coherent four dimensional physical state of the ocean (temperature, salinity, velocities).

2.2 Argo Floats

The Argo program was launched in the early 2000 to provide temperature and salinity profiles in the first 2000 m of the World Ocean using free drifting profilers (Argo float data and metadata from Global Data Assembly Centre (GDAC)). Between 2002 and present, 36536 quality-checked profiles were obtained in the Argentine Basin (Figure 2a). After 2020, a few deep Argo floats provided data from 4000 m up to the surface (570 profiles, Figure 2b).

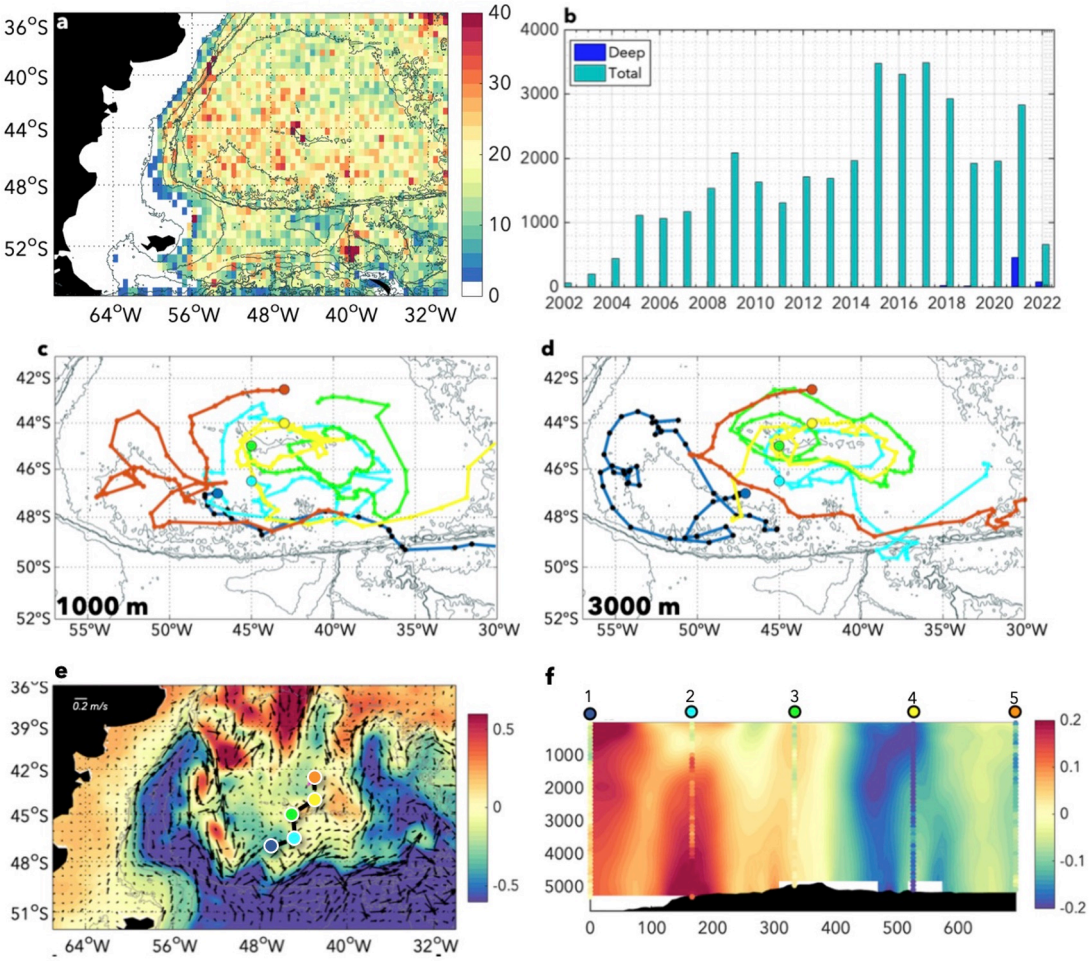

Figure 2: a) Number of profiles per 0.5° × 0.5° longitude-latitude bins during the period 2002-2022. b) Total number of profiles per year in the region (cyan bars) and number of deep profiles per year in dark blue.c) Trajectories of Argo classic floats drifting at 1000 m (deployed in 2021, from March 12 to September 17). d) Same as c) for deep floats drifting at 3000 m.e) SSH and surface velocities from PSY4 averaged over the 12, 13 and 14 March 2021. The coloured circles show the deployment locations of CTD and LADCP.f) PSY4 zonal velocity along the dashed line in e). LADCP zonal velocities measured at the 5 stations are represented with colored circles.

Five pairs of Argo floats were deployed within the ZAC during the SAGA10W cruise on board of the Spanish R/V Sarmiento de Gamboa between the 12 and 14 of March 2021. Each pair comprised a classic float drifting at 1000 m and a deep float drifting at 3000 m and sampling down to 4000 m. The Argo floats profiled to the surface every 5 days during 6 months (period of the trajectories shown in Figures 2c and 2d). CTD and LADCP

measurements were performed at the deployment locations (stations shown in Figures 2c-e-f).

Mercator models assimilate observations from the Argo array in the first 2000 m of the water column. Deep Argo floats are independent data as they are not at all assimilated in the model, which makes possible further model assessment at depth.

2.3 Further model validation

Previous works have already assessed the skills of global reanalysis in the first 2000 m of the Argentine Basin with a focus on the Malvinas Current region (e.g. Artana et al., 2018, 2019; Poli et al., 2020). Here, we expand the area to 30°W and we extend in time until the end of 2021. To assess models performances at depth, we compared PSY4 model fields to data from the cruise SAGA10W and deep Argo floats deployed in 2021 (period not covered in GLORYS12) (Supplementary S1). The mean temperature and salinity (vertically averaged over bins of 400 m) and the standard deviation from model and Argo float data are close (Figures S1, b and c). The differences between in-situ and modeled mean salinity remain lower than 0.01 PSS-78, while below 1200 m the modeled temperatures are slightly colder than measured ones by about 0.1°C (standard deviation of about 0.3°C) (Figures S1, d and e, Table S1).

We compared PSY4 velocities to those estimated from Argo floats drifting at parking depth using the ANDRO method (Ollitrault et al., 2013) which assumes that the trajectory between two successive float positions is linear (Figures 2c and 2d, see Figure S2a). Model velocities were interpolated at the mid position between two successive Argo profiles and averaged over the elapsed time (5 days, Figure S2b).

Within the ZAC, differences at 1000 and 3000 m between the modelled and "Argo" velocities do not exceed 0.1 m/s. Outside, differences can reach 0.2 m/s, because of the strong mesoscale activity which probably limits the validity of the linear interpolation (Figures 1b, c and d, Supplementary S3). Zonal velocities from PSY4 and LADCP data at the floats

deployment show common patterns. For instance, both feature strong eastward velocities at depth (> 0.2 m/s) above the Zapiola Rise at station 2 and strong westward velocities at station 4 (Figure 2f). Overall, the comparisons show that the model correctly reproduces hydrography and circulation of the Zapiola Anticyclone at depth.

3 Circulation in the Argentine Basin

3.1 Mean depth-integrated large scale circulation

The vertically integrated mean transport stream function (Figure 3a) computed from the 27 years reanalysis GLORYS12 highlights structures with virtually no signature in mean surface velocities (Figure 1a). In particular the ZAC, with small surface velocities compared

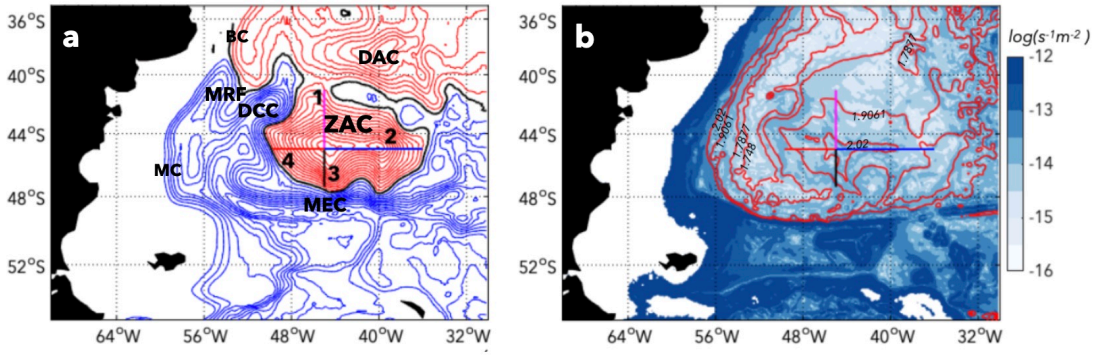

Figure 3: a) Vertically integrated mean transport stream function computed from GLORYS12 reanalysis for the period 1993-2019 (contours every 10 Sv). lue contours represent cyclonic and red anticyclonic circulation.The zero contour is in black. b) $\log_{10}$ of the modulus of f/h gradient (blue shading) and f/h contours (1.748×10^{-8}, 1.7877×10^{-8}, 1.9061×10^{-8}, 2.020×10^{-8} $\mathrm{m^{-1}s^{-1}}$) in red. The meridional (1 and 3) and zonal (4 and 2) sections used to compute volume transports are indicated with magenta, black, red and blue lines. Acronyms in panel a stands for : MC: Malvinas Current. MRF: Malvinas Return Flow. DCC: Deep Cyclonic Circulation. ZAC: Zapiola Anticyclonic Circulation. BC: Brazil Current. DAC: Deep Anticyclonic Circulation. MEC: Malvinas Escarpment Current.

to other currents (Figure 4a), stands out with a mean volume transport of 120 Sv (Figure

3a). The transport stream function closely follows f/h contours around the Zapiola Rise (Figure 3b). The two closed contours in the transport stream function around 45°S-45°W and 45°S-39°W correspond to two summits of the Zapiola Rise.

The ZAC is intensified at depth with bottom speeds of the order of 0.10 m/s (Figure 4b). The mean cross-section speeds increase in the upper layers with a positive shear above 1000 m (1×10^{-5} s^{-1}, 10 cm/s every 1000 m, positive meaning increasing speeds with depth) while they are rather homogeneous below (small shear) (Figure 4 c, d, e, f and g).

Saraceno et al., [2009] estimated a mean ZAC transport of 48 Sv over the period 1993-2007 whereas we obtain 122.6 Sv over the same period. They assumed that the flow was barotropic (zero vertical shear) and used the surface geostrophic velocities derived from altimetry to compute the total transport. This method led to an underestimation of the transport as the ZAC is bottom-intensified. Colin de Verdière and Ollitrault [2016] evaluated the transport from Argo float drift velocities at 1000 m combined with a mean oceanic climatology to compute geostrophic velocities and obtained a mean value of 124 Sv over the period 2004-2010. This value is in agreement with our estimate of 127 Sv over the same period. The reanalysis-derived value corresponds to the one estimated by Johnson and King [2023].

The total transport stream function also shows a strong cyclonic circulation centered at 42°S-50°W, northwest of the ZAC and just east of the BC overshoot (labelled DCC for Deep Cyclonic Circulation, Figure 3a). This cyclonic circulation has almost no surface signature (Figure 1a). It transports approximately 60 Sv and follows f/h contours (see contour 1.748×10^{-8} $m^{-1}s^{-1}$ in Figure 4). Close to the bottom, velocities in the DCC reach ~ 0.2 m/s (Figure 4b). The DCC is a deep western boundary current which carries waters entering the basin through a gap located at 40°W-48.5°S to the north east of the Malvinas Plateau (the gap is indicated in Figure 4b). These waters flow westward within a narrow current reaching 1200 m, the Malvinas Escarpment Counter Current (hereafter MECC), which follows the Malvinas Escarpment with a mean speed around 0.2 m/s (Figures 4b-

d). Those values are consistent with direct measurements (Whitworth et al., 1991). The currents forming the DCC are in opposite direction to the surface Malvinas Escarpment Current (MEC, Figures 4a-c at 50°S) and to the Malvinas Return Flow (MRF, Figures 4a-c at 55°W). The mean vertical shear along the Malvinas Escarpment changes sign with depth: it is negative in the upper 2000 m indicating a surface intensified flow and positive below with a bottom intensified flow around 50°S (Figures 4e-f). The differences between the upper 2000m and below 2000m could be partially related to the lack of assimilated data below 2000m. Model-derived vertically integrated transports of the western boundary currents (40 Sv for the northward barotropic equivalent MC at 38°S and 30 Sv for the southward BC at 36°S) agree with the estimates from observations (Spadone and Provost, 2009; Maamatuaiahutaipu et al., 1998; Schmid Majumder, 2018; Artana et al., 2018). The closed contours centered at 38°S-38°W (Figure 3a) indicate a deep anticyclonic circulation of about 50 Sv (hereafter DAC) which follows closed f/h contours (Figure 3b) with bottom velocities of about 0.1 m/s (Figure 4b). The deep circulation patterns reproduced by the reanalysis are consistent with the existing literature (e.g. Whitworth et al., 1991; Peterson, 1992; Coles et al., 1994).

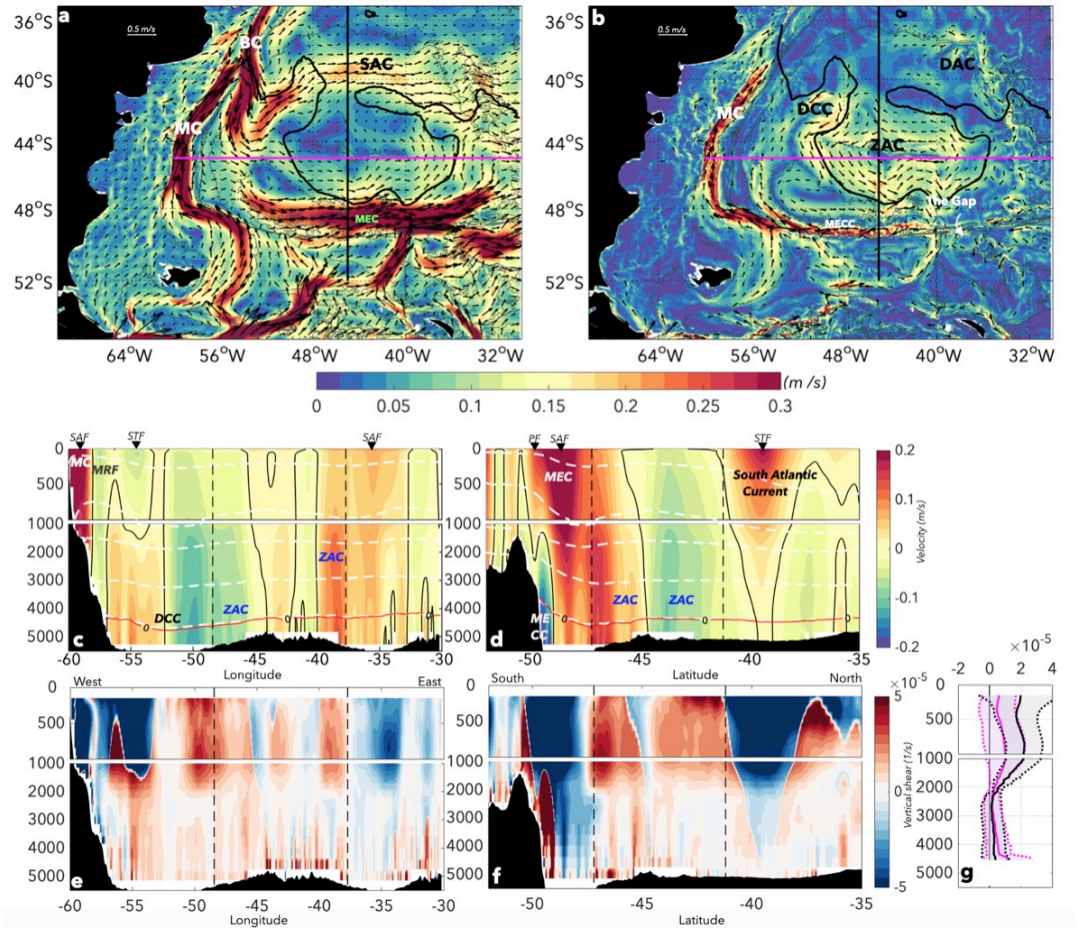

Figure 4: a) Mean surface velocities (amplitude in color) from GLORYS12 reanalysis (1993-2019). Only velocities exceeding 0.05 m/s are plotted. The thick black isoline corresponds to the zero of the mean vertically integrated transport in figure 3a). b) Same as a) for the mean velocity near the bottom, thus variable depths. c-d) Mean velocities along 45°S and 45°W sections indicated in Figure 1a. White dashed lines are γ^n water masses limits (see table S2). The black line corresponds to the zero velocity isoline. ZAC: Zapiola Anticyclone Circulation. MEC : Malvinas Escarpment Current. MC: Malvinas Current. MRF : Malvinas Return Flow. MECC : Malvinas Escarpment Counter Current. The mean locations of the fronts are indicated. PF: Polar Front. SAF: Subantarctic Front. STF: Subtropical Front. DCC: deep cyclonic circulation. DAC: Deep Anticyclonic Circulation. e-f) Mean vertical shear of velocities interpolated every 100 m depth. g) Mean vertical shear of velocities averaged within the ZAC and associated spatial standard deviation (shaded) along the zonal (in magenta) and meridional (in black) sections. The two vertical dashed lines correspond to the ZAC boundaries. Vertical scale is expanded in the upper 1000 m.

3.2 Variations of low-passed (> 90 days) ZAC transport

Four sections with a common origin at 45°S-45°W (sections 1, 2, 3 and 4 in Figure 3) were selected to compute a time series of the ZAC volume transport. Sections 2, 3 and 4 extend to the zero contour obtained from the mean total transport stream function around the Zapiola Rise and section 1 extends to the local minimum at 41.2°S-45°W (see Figure 3a). The volume transport across zonal sections 2 and 4 (meridional sections 1 and 3) is defined as: $\int_0^L \int_0^H V dx dz$ ($\int_0^L \int_0^H U dy dz$) where V is the meridional component and U the zonal component of the velocity, L the section length and H the oceanic depth. A fourth-order Butterworth low-pass filter (with a cut-off frequency of 1/90 days) is applied to the transport time series corresponding to the four sections and the correlations between the four low-passed time series always exceed 0.8 (at lag 0). The four low-passed time series were averaged to obtain a unique series. We used GLORYS12 outputs for the period 1993-2019 and PSY4 outputs for 2007-2021. Transports computed from PSY4 and GLORYS12 over the overlapping period (2007-2019) show close means (115.7 and 122.6 Sv, respectively) and similar fluctuations (standard deviations of 48 and 48.5 Sv, respectively) with a correlation coefficient of 0.81 (Figure 5a).

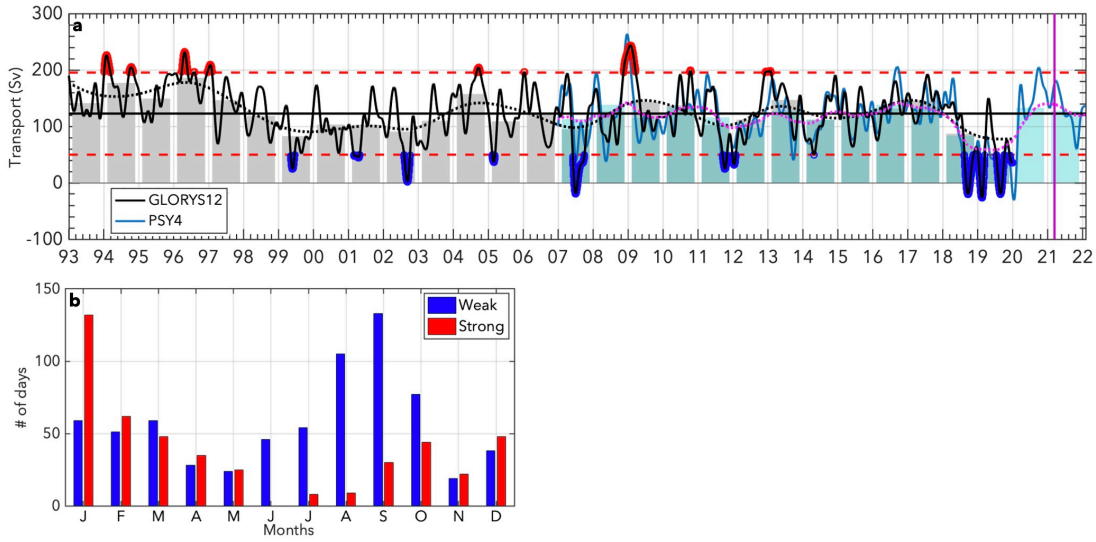

Figure 5: a) Mean transport time series computed as explained in section 3.2. The black horizontal line represents the mean, the red dashed lines are mean ±1.5 standard deviation. The dashed black line shows the low-pass filtered transport (3-year cut-off period). Strong and weak events are highlighted in red and blue. The purple vertical line indicates the date of the SAGA 10W cruise. Bar plot in the background shows the annual mean of transport in grey for GLORYS12 and in blue for PSY4. b) Monthly distribution of extreme events in number of days.

The low-pass volume transport time series includes extreme events exceeding 1.5 standard deviation (highlighted in red and blue in Figure 5) with 494 days (5% of the time series)of strong extreme events (transport exceeding 195.4 Sv, Figures 5a and 6d) and 689 days (7% of the time series) of weak extreme events (transport less than 49.8 Sv, Figures 5a and 6e). The total transport exhibits negative peaks in 2007, 2018 and 2019. The mean duration of extreme events, regardless of whether strong or weak, is approximately 65 days except for the extreme weak event of 2018-2019 which lasts 285 days. The extreme events show a seasonal distribution: weak events tend to occur in austral winter while strong events are more frequent in summer (Figure 5b).

The transport time series also features milder fluctuations over a wide range of periods between 100 and 730 days (see supplementary Figure S4). The annual means (grey bars) show a low frequency modulation with alternating periods of large (1993-1996, 2003-2017,

2021-2022) and low transport (1997-2003, 2018-2020) as illustrated with the black dashed line corresponding to the 3 year low passed filtered transport (Figure 5). The transport time series exhibits a robust trend of -15 Sv.$decade^{-1}$ whatever the chosen end-point (end of 2019 or 2017 to avoid any bias due to the outstanding 2018-2019 event). The negative transport trend results from the cyclonic velocity trend pattern in the whole water column observed in the ZAC (see supplementary S5).

3.3 The Argentine Basin during extreme events.

To investigate the ZAC circulation and structure associated with extreme events, we computed cross-section velocities (Figure 7) and composites of the total transport stream function (Figure 6). Two specific synoptic events, the strongest event in January 2009 (with a transport reaching 268 Sv, Figure 6c) and the weak event in June 2007 (with a negative transport of -12 Sv, Figure 6d) are presented as examples.

The composites suggest that there is a little variation in the lateral extension of the ZAC during extreme events, which is consistent with a topographic influence on the circulation (Figures 6a-b). However, the circulation in the ZAC interior is modified. During strong events (mean transport of 211 Sv, Figure 6a), the ZAC exhibits a near solid-body rotation. The composite of weak events (mean transport of 22 Sv) shows that the ZAC includes secondary anticyclonic circulations (Figure 6b). In some occasions, like during the extreme event in January 2009 (268 Sv), the ZAC boundary is distorted (Figure 6c), while in June 2007 (-12 Sv), the ZAC is totally disaggregated and the overall anticyclonic circulation is disrupted (Figure 6d).

During strong events, velocities increase in the whole water column in the ZAC (Figures 7a-b). The velocity shear is increased between 0 and 2000 m (compare to Figure 4g). It nearly vanishes between 2000 m and 4500 m. This illustrates that the velocity increase is more pronounced below 2000 m than in the upper layers. During weak events, the anticyclonic secondary circulations mentioned above are observed in the first 1000 m of

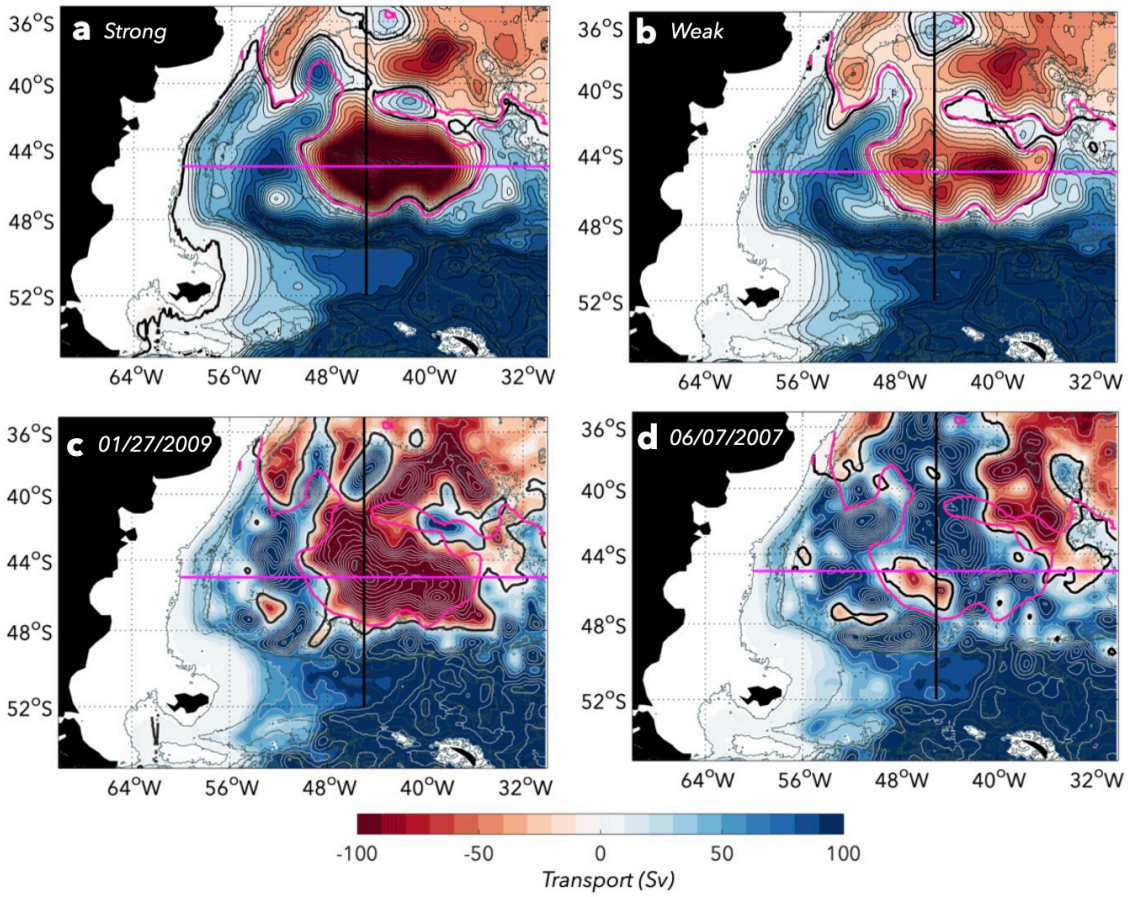

Figure 6: a) Total transport stream function composite for strong events. Contours are plotted every 10 Sv; the 0 Sv contour is a thick black contour. The mean 0 Sv contour is in magenta from Figure 3a. b) same as (a) for weak events. c-d) Total transport stream function the 01/27/2009 (c) and the 06/07/2007 (d). Contours every 20 Sv. Black thick contours correspond to 0 Sv.

the zonal section at 45° S (Figure 7d). Below 1500 m, outer branches of the ZAC are strongly reduced with bottom velocities less than 0.05 m/s. A cyclonic circulation with velocities reaching 0.1 m/s at the center of the ZAC is located over a depression between the two summits of the Zapiola rise (Figures 7d-e). The currents decrease with depth and the vertical shear becomes negative in the whole water column (Figure 7f).

The circulation is also modified in the whole Argentine Basin during extreme events (Figure 6). The DCC is reinforced with bottom velocities reaching 0.15 m/s during strong

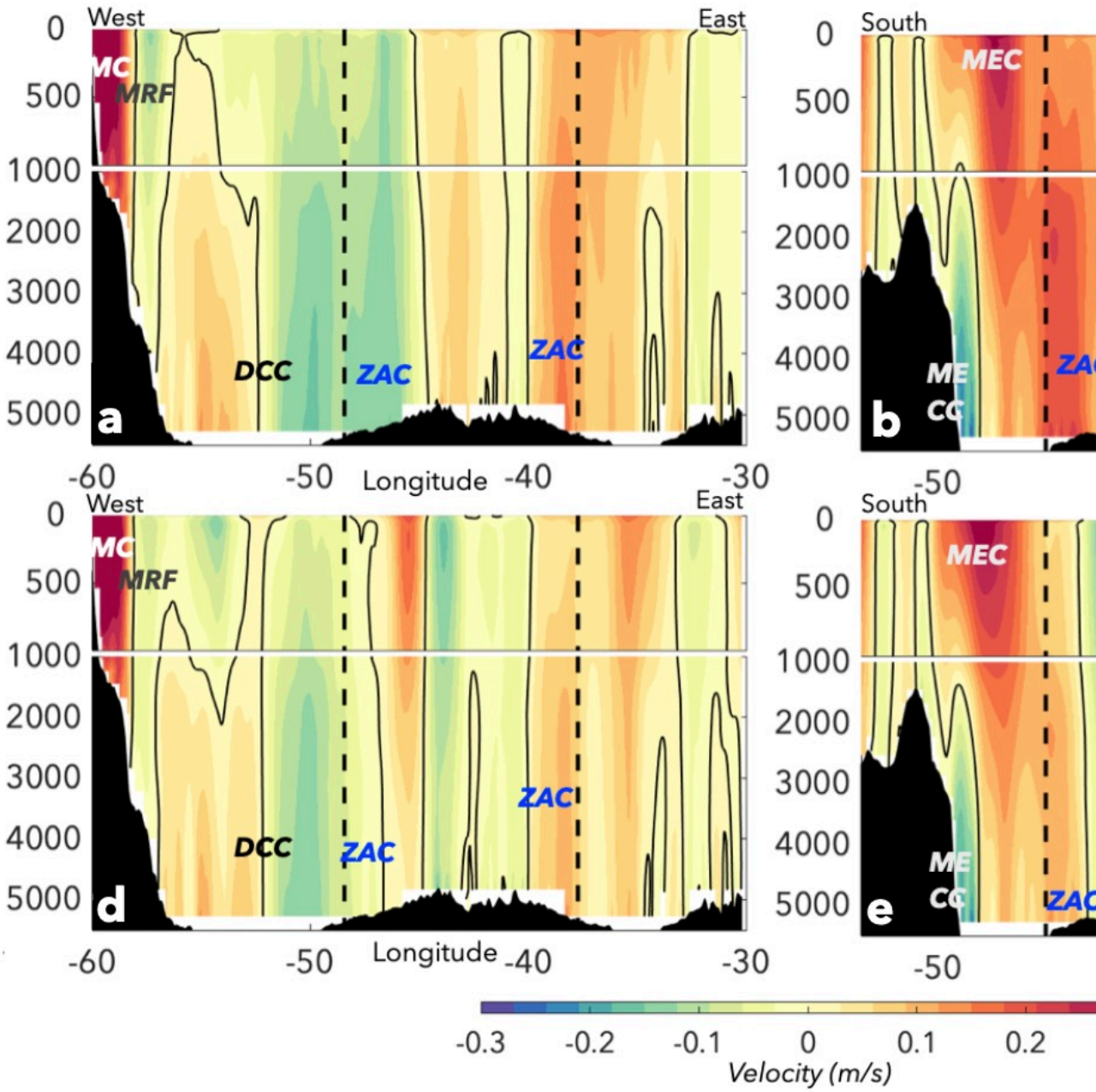

Figure 7: a-b) Cross-section velocities composites along the sections 45°S and 45°W for strong events. The 45°S section is in magenta and the 45°W in black. The mean ZAC limits are indicated in black dashed lines. c) Vertical velocity shear averaged within the ZAC limits for strong events. d-e-f) Same as (a-b-c) for weak events.

events and weakened during weak events (Figures 7a-c). Westward velocities associated with the MECC are above their mean values (0.2 m/s compared to 0.1 m/s) during strong events and below during weak events (−0.05 m/s). The MECC extends from the bottom up to 1000 m depth during weak events instead of 1300 m during strong events (1200 m corresponds to the mean field, see figures 6c-g in comparison with figure 4d).

The overall intensification or weakening of the circulation during strong and weak events suggests a large scale forcing (Figures 6 and 3a).

4 Hydrographic properties in the Argentine Basin

4.1 Mean and trends in hydrographic properties

Water masses were identified using neutral density and salinity criteria, following Preu et al. [2013], Valla et al. [2018] and Emery and Meincke, [1986] (Table S2, supplementary material). Mean hydrographic properties are illustrated along the meridional section at 45°W (Figure 8). Surface waters comprise Subantarctic Surface Waters (SASW; $\gamma^n <$ 27.1 g/kg) in the first 100 m of the water column to the south of 48°S, South Atlantic Central Waters (SACW; $\gamma^n <$ 27.1 g/kg) between 48°S and 42°S and Tropical Waters (TW; $\gamma^n <$ 26.35 g/kg) in the upper 250 m to the north of 42°S (Figures 8a, b and c). Underneath, waters are stacked as follows: Antarctic Intermediate Waters (AAIW; 27.1 $<$ $\gamma^n <$ 27.6 g/kg; 33.9 $<$ salinity $<$ 34.25 PSS-78), Upper Circumpolar Deep Waters (UCDW; 27.6 $< \gamma^n <$ 27.9 g/kg), Lower Circumpolar Deep Water (LCDW; 28.1 $< \gamma^n <$ 28.27 g/kg; salinity $<$ 34.8 PSS-78) and at the bottom the Antarctic Bottom Waters (AABW; $\gamma^n >$ 28.27 g/kg and negative potential temperature) (Figure 8 a, b and c). In the northern part of the basin, the North Atlantic Deep Waters (NADW: 27.9 $< \gamma^n <$ 28.1 g/kg; salinity $>$ 34.8) lie between the UCDW and the Lower Circumpolar Deep Water (Figures 8a, b and c). The Zapiola circulation induces a doming of isopycnals which are tilted at the boundaries of the ZAC (Figures 8b and c). Hydrographic properties exhibit trends over the 27 year-long reanalysis. We consider the trend to be significant when it is statistically significant (t-test)

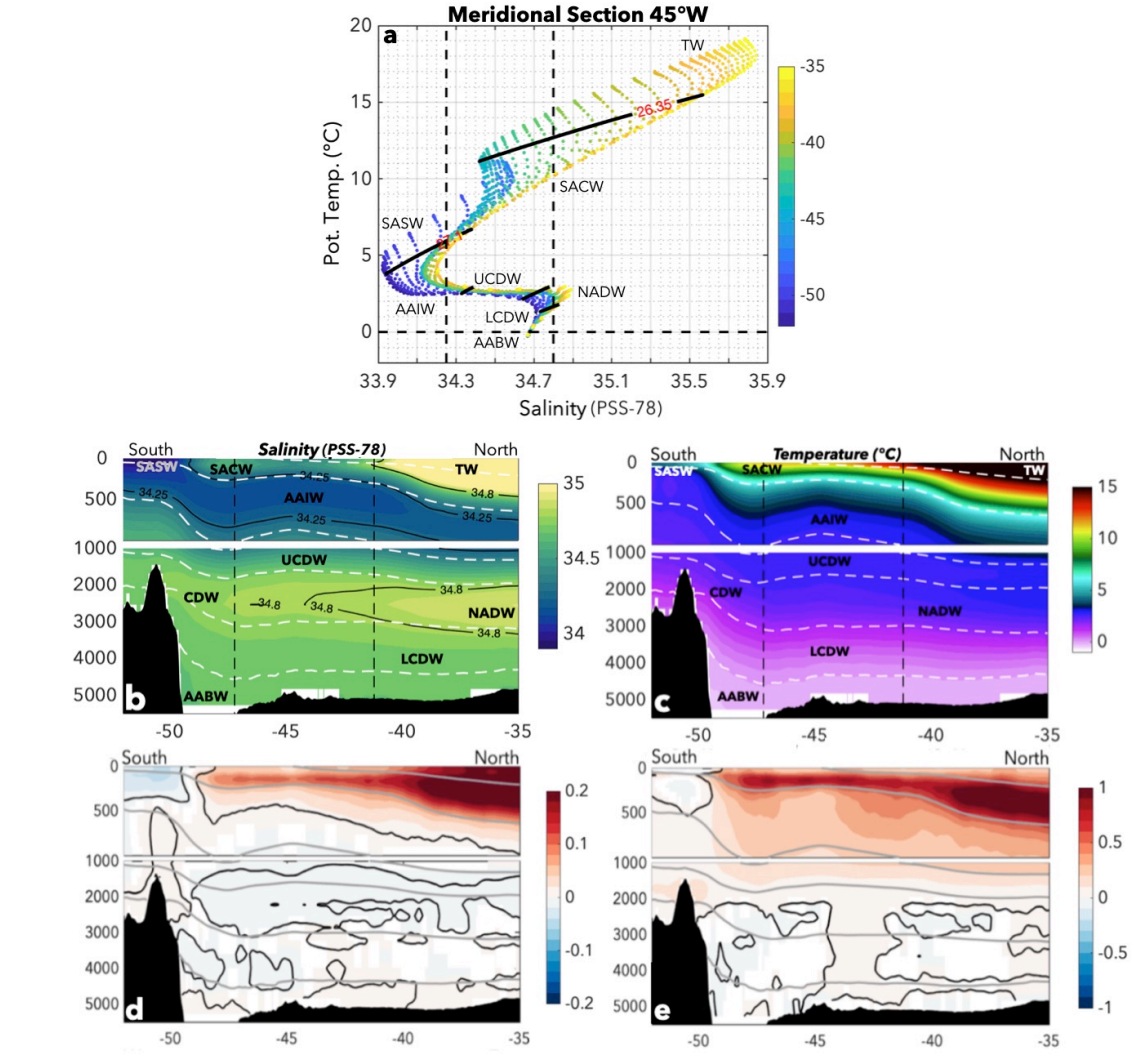

Figure 8: a) Mean θ/S diagram along the 45°W section (black line in Figure 1a). Colors indicate latitude. γ^n contours in black mark the limits between water masses and dotted black lines the θ and S criteria of 0°C and 34.8, 34.25 PSS-78. Main water masses are labelled. b-c) Mean salinity (b) and mean temperature (c) along the 45°W section as a function of latitude and depth. γ^n limits are plotted in white dashed lines, salinity criteria in black. d) Salinity linear trends in PSS-78.$decade^{-1}$ along the 45°W section. Shaded values are statistically significant. e) Same as (d) for temperature in $°C.decade^{-1}$. γ^n limits are plotted in thick grey lines. Thick black lines indicate regions where the absolute value of the trend exceeds the interannual standard deviation.

and when it exceeds the interannual standard deviation. Negative salinity trends close to the surface in the south of the section (-0.03 PSS-78.$decade^{-1}$, Figure 8d) are consistent with

the overall freshening of subantarctic waters reported in several studies (e.g. Böning et al., 2008; Naveira Garabato et al., 2009; Purich, 2018). This freshening is significant in the MC and to the south of the ZAC (Figure S6b). Large positive trends are observed down to 500 m in salinity (+0.2 PSS-78.$decade^{-1}$) and down to 1000 m in temperature (+1° C.$decade^{-1}$) to the north of the 45°W section (Figures 8d-e). These positive trends are significant in the whole Argentine Basin (Figure S6c) and are probably associated with the temperature and salinity increases observed in the tropical waters in latitudes dominated by evaporation (Durack et al., 2012; Yu et al., 2020). In the ZAC the positive trend in temperature extends down to 5000 m, which is consistent with several studies that documented bottom water warming in the Argentine Basin (e.g. Coles et al., 1996, Johnson, 2022). On top of these linear trends, water properties experienced interannual variations which are investigated in the next section.

4.2 Hydrographic multi-year modulation

Linear trends were removed to investigate the interannual variability of the hydrographic characteristics. Large multi-year modulation of salinity stands out until 2010 while fluctuations of higher frequency and smaller amplitude are later observed (Figure 9a and b). Salinity anomalies are positive (between $\simeq 0.05$ and $\simeq 0.1$ PSS-78) and larger than the annual trend (< 0.02 PSS-78/year) during periods 1993-1997 and 2003-2009; while they are negative (between -0.05 and -0.1 PSS-78) during period 1998-2003 and extend down to 2000 m (Figures 9a-b). Salinity anomalies averaged over each period along the meridional section are large to the north of 40°S in the upper 500 m (Figures 9d and f). Maps of averaged salinity anomalies at 541 m show a consistent large-scale signal all over the basin for each period, with the largest anomalies located within the Subtropical Gyre (Figures 9g-h-i).

These distinct periods of negative (1998-2003) and positive (1993-1997 and 2004-2009) salinity anomalies coincide with weak and strong ZAC transports respectively (160 Sv for 1993-1997, 126 Sv for 2004-2009 and 101.3 Sv for 1998-2003, Figure 9 c). During 1998-2003,

the subtropical front (red line in Figure 9h) is shifted northward (as the transport of the Subtropical Gyre is smaller), reducing the southward advection of salty subtropical waters which could partly contribute to the salinity reduction.

The annual distribution of extreme events is not homogeneous over time. The first period accounts for a total of 240 days of strong events and no weak events, the second host a great majority of weak events (166 days of weak and only 39 of strong transport events). The number of weak and strong events in the third period is relatively well balanced (192 days of strong and 151 days of weak events). The last period, 2010-2019 is dominated by weak events (371 days) compared to strong events (62 days).

In the following section, we analyze the hydrographic characteristics of the ZAC during extreme events, keeping in mind their uneven temporal distribution.

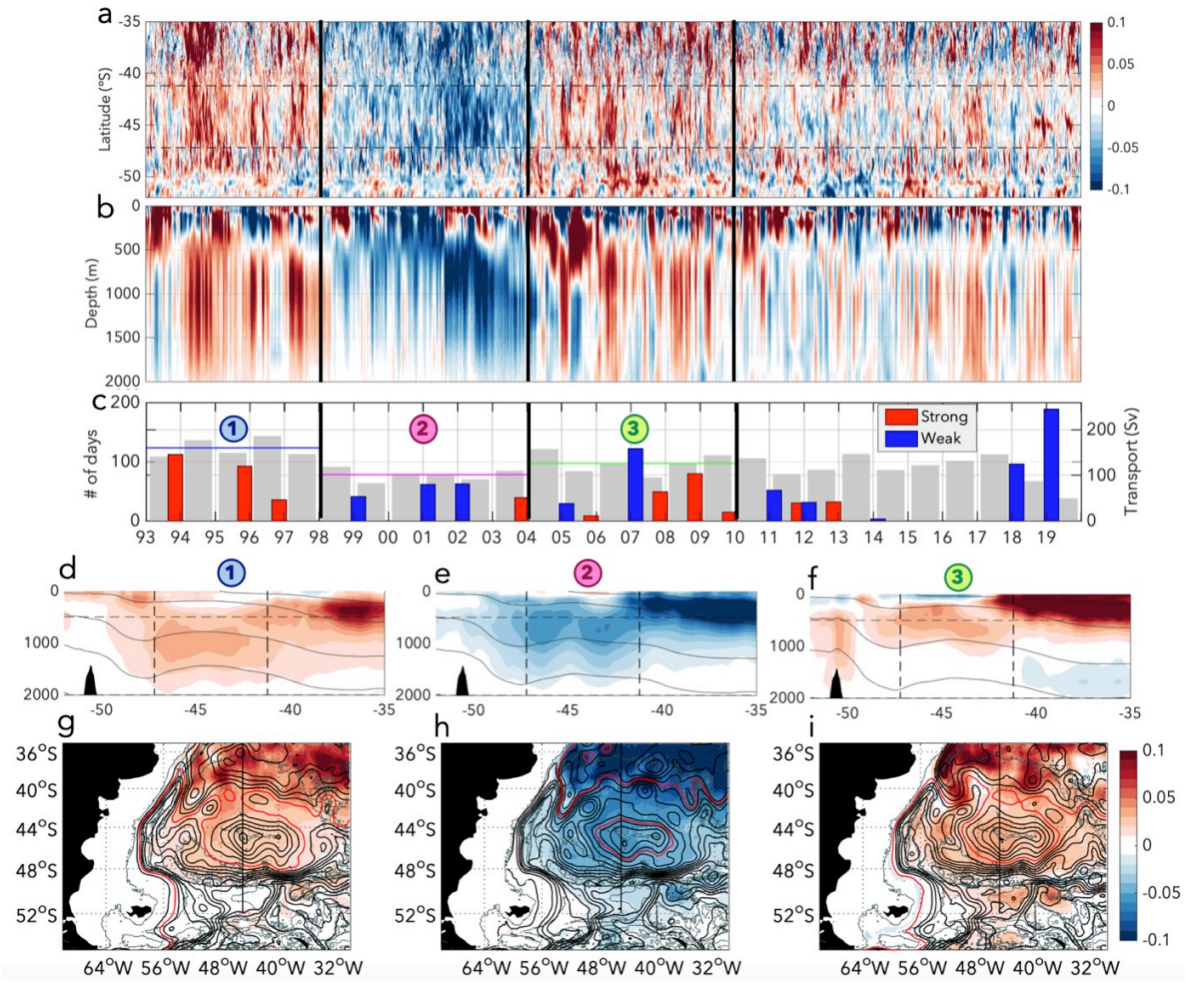

Figure 9: a) Time-latitude diagram of detrended salinity anomalies along the 45°W section. Anomalies have been averaged between 500 m and 2000 m. Black dashed lines at 41.2° and 47.2° S correspond to the ZAC limits. b) Time-depth diagram of detrended salinity anomalies within the ZAC. Anomalies have been averaged within the ZAC limits in the zonal and meridional direction at each depth. c) Annual mean transport (grey bars) and yearly distribution of extreme events (red: strong events; blue: weak events). The vertical black lines separate the periods 1993-1997, 1998-2003 and 2004-2009. d-e-f) Detrended salinity anomalies along the meridional section averaged over the periods 1993-1997 (d) 1998-2003 (e) 2004-2009 (f). Black contours correspond to neutral density limits, vertical dashed lines to the ZAC limits and horizontal black dashed lines to the 541 m depth. g-h-i) Detrended salinity anomalies at 541 m for the three periods. Contours correspond to the transport (in Sv) integrated between 0 and 2000 m. The red contour corresponds to the 0 Sv contour of the transport stream function and contours are every 10 Sv.

4.3 Hydrographic properties during extreme events :

Composites of temperature and salinity anomalies for weak and strong events were compared along the 45°W section (Figure 10). Main hydrographic differences between

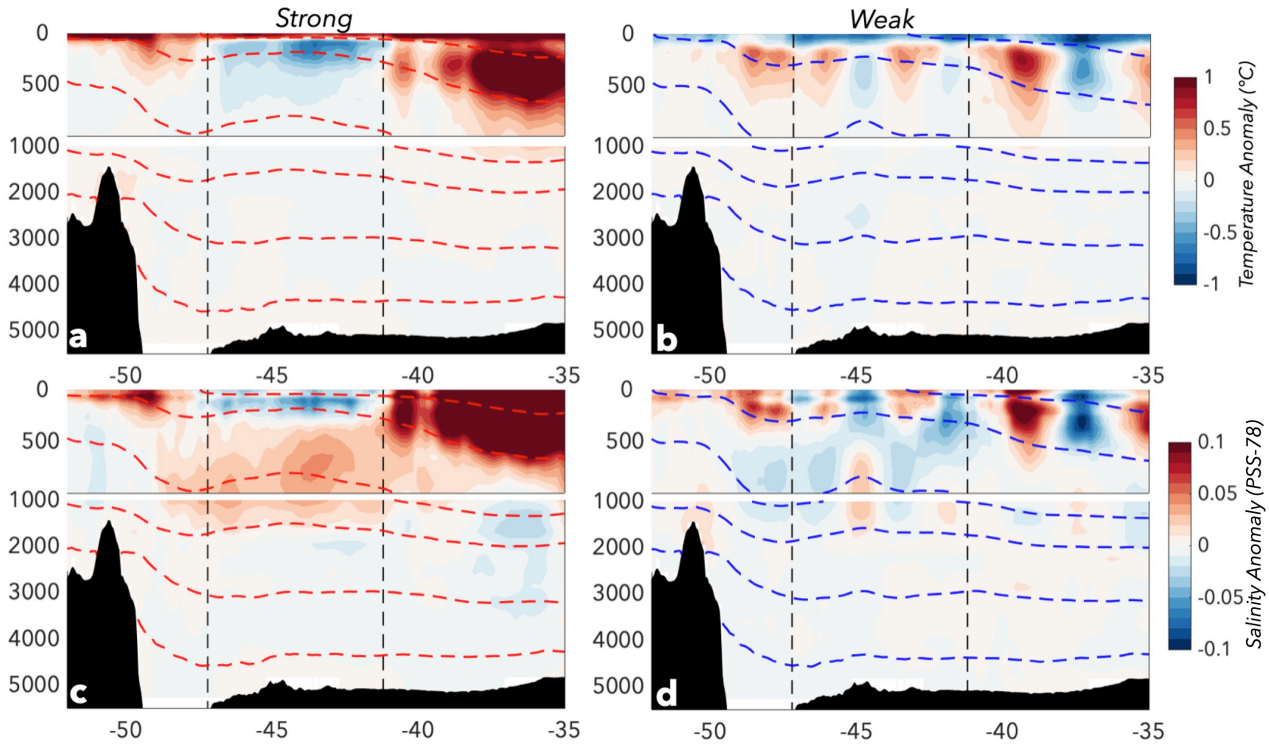

Figure 10: a-b) Composite of detrended temperature anomalies for strong (a) and weak (b) events. c-d) Composite of detrended salinity anomalies for strong (c) and weak (d) events. Red and blue dashed lines correspond to neutral densities and black vertical dashed lines to the ZAC limits.

strong and weak events are located between the surface and the UCDW (Figure 10). The signal observed in the upper 50m reflects the seasonal distribution of weak and strong events. Weak events tend to occur in austral winter and are associated to a cold surface signal while strong events are more frequent in austral summer and are associated to a warm surface signal (Figure 5b).

During strong events the Subtropical Gyre and the MEC are intensified (cf section 3.2) which probably leads to the positive salinity anomalies observed to the south and north of the ZAC (Figures 10a-c). During strong events temperature and salinity anomalies are homogeneous within the ZAC and their vertical distribution reflects the effect of the isopycnal doming (related to the ZAC intensification) on the vertical stacking of water masses. Thus there is a cold signal in the upper 700 m, a fresh signal in the upper 300 m and a salty

signal between 300 and 1500 m (Figures 10a-c). In contrast, during weak events, the ZAC is more permeable to mesoscale structures coming from the basin, leading to temperature and salinity anomalies of opposite sign within the ZAC. The positive temperature anomalies observed between 42° S and 47° S in the 50-250 m layer (Figure 10b-d) correspond to warm and salty waters in the secondary circulations visible in Figure 7d-e. These secondary anticyclonic recirculations induce a downwelling and deepening of isopycnals. A distinct isopycnal shoaling at 45°S (of about 300 m at 1000 m, blue dashed lines in Figures 10b-d) associated with cold (−0.3°C) and salty (+0.03 PSS-78) anomalies below 500 m correspond to the cyclonic circulation present during weak events. Every single selected weak event features a cyclonic eddy at the center of the ZAC (not shown). One of them was documented by the Argo float #3901515, which got trapped within a cyclonic eddy (C1) from October 2018 until January 2019 at the time of a drastic transport reduction (−18.5 Sv, the minimum of the transport time series) (Figures 11b). C1 lasted for more than 285 days and was tracked back in satellite maps. C1 was shed at 33°W-44°S by a meander of the SAF and the PF (on May 12 2018) and penetrated the ZAC through the northeast boundary where the f/h gradient is relatively weak (Figure 3b). It reached the center of the ZAC on the fifth August 2018 (Figures 11a-b). The Argo float sampled relatively cold and fresh waters within the cyclonic eddy (Figure 11c).

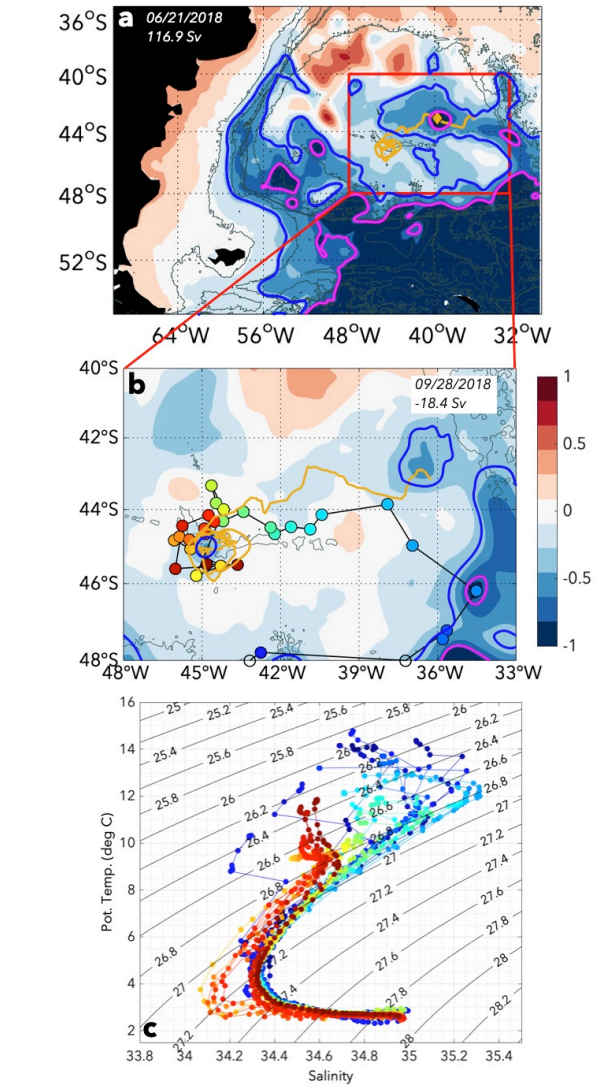

Figure 11: a-b) SSH snapshots during the detachment of C1 from the SAF meander a) the 06/21/2018 and b) a zoom on the 09/28/2018. The eddy trajectory computed from the eddy atlas is indicated in yellow. The eddy position at the date is indicated by a yellow diamond in a and by a blue circle in b. Trajectory of the Argo float #3901515 (colored dots) and C1 trajectory from the eddy atlas (yellow line). c) θ/S diagram from Argo float #3901515 measurements. The colors correspond to the dots in panel b).

5 Discussion

Theoretical studies based on realistic and idealized simulations without data assimilation (e.g. de Miranda et al., 1999; Bigorre and Dewar, 2009; Venaille et al., 2011) and observational studies (e.g. Fu, 2007) suggested that the ZAC variability is driven by kinetic

energy transfers and wind stress curl. GLORYS12 tends to reproduce the EKE at the right time and location probably due to data assimilation . However, the precise distinction between the role of data assimilation and model dynamics is challenging. We computed the EKE as follows : $EKE = \frac{U'^2+V'^2}{2}$ with $U' = U - \overline{U}$ and $V' = V - \overline{V}$, the overbar indicated the velocities time average over the entire period.

EKE and WSC exhibit trends over 27 years that emerge from interannual variability (Figure 12).

The linear trend of surface EKE is negative to the north of 40°S (-0.015 (m/s)^2.$decade^{-1}$s) and positive to the south ($+0.015$ (m/s)^2.$decade^{-1}$s), reflecting the southward shift of the BC (strong anticyclonic trend in the surface velocities of the BCO, see supplementary S5) and the entire Subtropical Gyre. This EKE trend is consistent with the global increase in mesoscale activity documented at the poleward boundaries of the Subtropical Gyres over the satellite altimetry record (e.g. Martinez-Moreno et al., 2021 and Li et al., 2023). The WSC linear trends are positive over the central Argentine Basin and negative along the Malvinas Escarpment and of the same sign of the mean WSC (Figure 1c), depicting an overall intensification of the atmospheric circulation (Figure 12b). The trends are consistent with the intensification and expansion, towards the West and the South, of the South Atlantic anticyclone that has been documented over the last decades (e.g Leyba et al., 2019, Li et al., 2023).

We opted for a composite analysis to examine EKE and WSC signals associated to extreme events as correlations between the EKE and the transport (WSC and the transport) were non conclusive as the system is strongly non linear.

Composites of detrended EKE anomalies for weak and strong events exhibit similar patterns but of opposite sign. Overall, the basin exhibits an increase of EKE during strong events except at the center of the ZAC while the opposite occurs during weak events. The EKE increase at the center of the ZAC during weak events reflects the cyclonic circulation previously described (see sections 3 and 4.3). Conversely, the EKE is enhanced at the

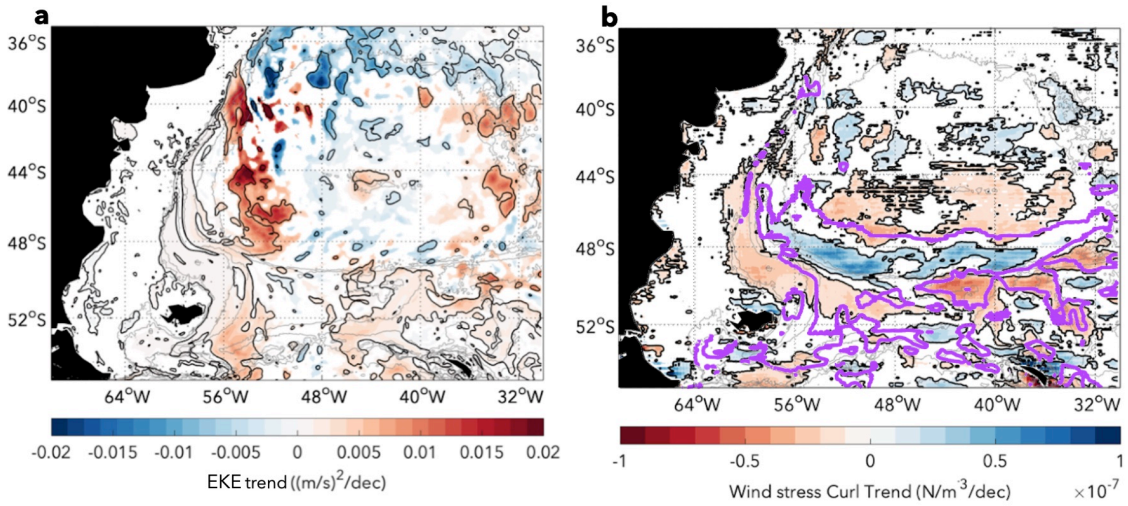

Figure 12: Linear trend over the period 1993-2019 from GLORYS12 and ERA-interim. Statistically significant values are shaded. a) Surface EKE trend. b) WSC trend. The thick black lines indicate regions where the absolute value of the trend exceeds the interannual standard deviation. The purple contour corresponds to the mean zero wind stress curl.

boundaries of the ZAC and reduced close to the center during strong events: the inward penetration of eddies is inhibited.

During strong events the WSC is enhanced over the ZAC and the southern part of the Subtropical Gyre, reinforcing the negative Ekman suction while the opposite occurs during weak events. This is consistent with the large-scale current intensification described in section 3.3 (Figure 6). The mean position of the zero WSC line in the western part of the basin is located southward around 48°S during strong events and northward around 41°S during weak events. As extreme events present a seasonal distribution (Figure 5b), we explore the seasonal means of EKE and WSC (Figure 14). The seasonal means resemble the composite of strong and weak events. Seasonal distribution of EKE features more energy to the north of the confluence in summer than in winter, which is probably associated with the southward shift of the subtropical front (Figure 13 a and b). The WSC is reinforced during austral summer and weakened in winter (Figure 13 c and d). Seasonal variability plays an important role in preconditioning the development of extreme transport events and their persistence.

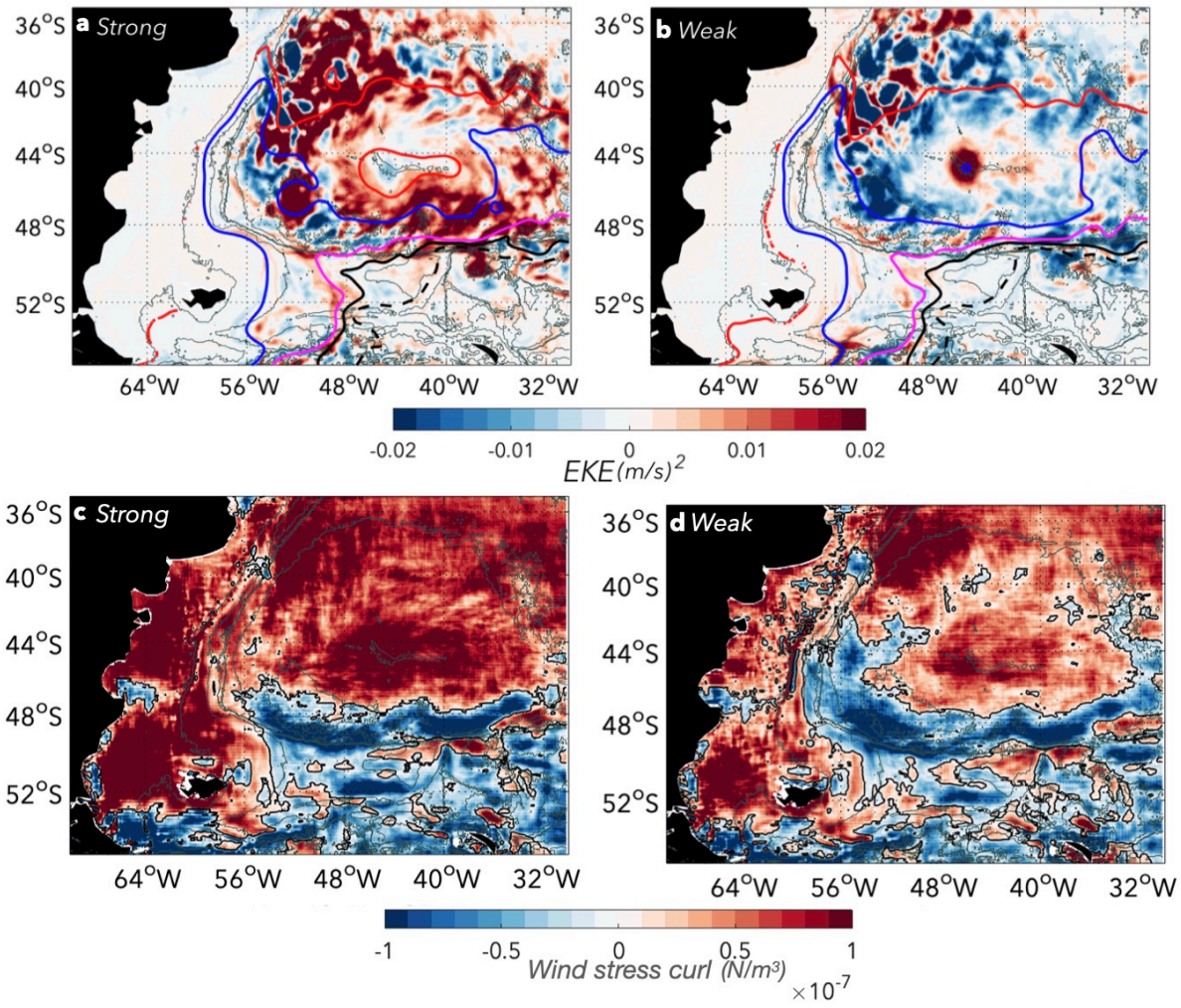

Figure 13: a-b) Composite of surface EKE for strong (a) and weak (b) events. Corresponding front positions are indicated with colored contours as in figure 1. c-d) Wind Stress Curl composites for (c) strong and (d) weak events. The zero Wind Stress Curl line is in black. Thick coloured contours in panels a and b indicate the position of the fronts (STF in red, SAF in blue and PF in magenta and black).

6 Summary and concluding remarks

We used a global ocean reanalysis (GLORYS12) over the period 1993-2019 to investigate the ZAC. The ZAC is bottom intensified with velocities reaching 0.1 m/s which is in agreement with a recent study based on in situ observations (Johnson and King, 2023). We constructed a 27 year-long ZAC transport time series which ranges between 268 Sv and -18.4 Sv with a mean value of 122.6 Sv (standard deviation of 48.5 Sv). The transport

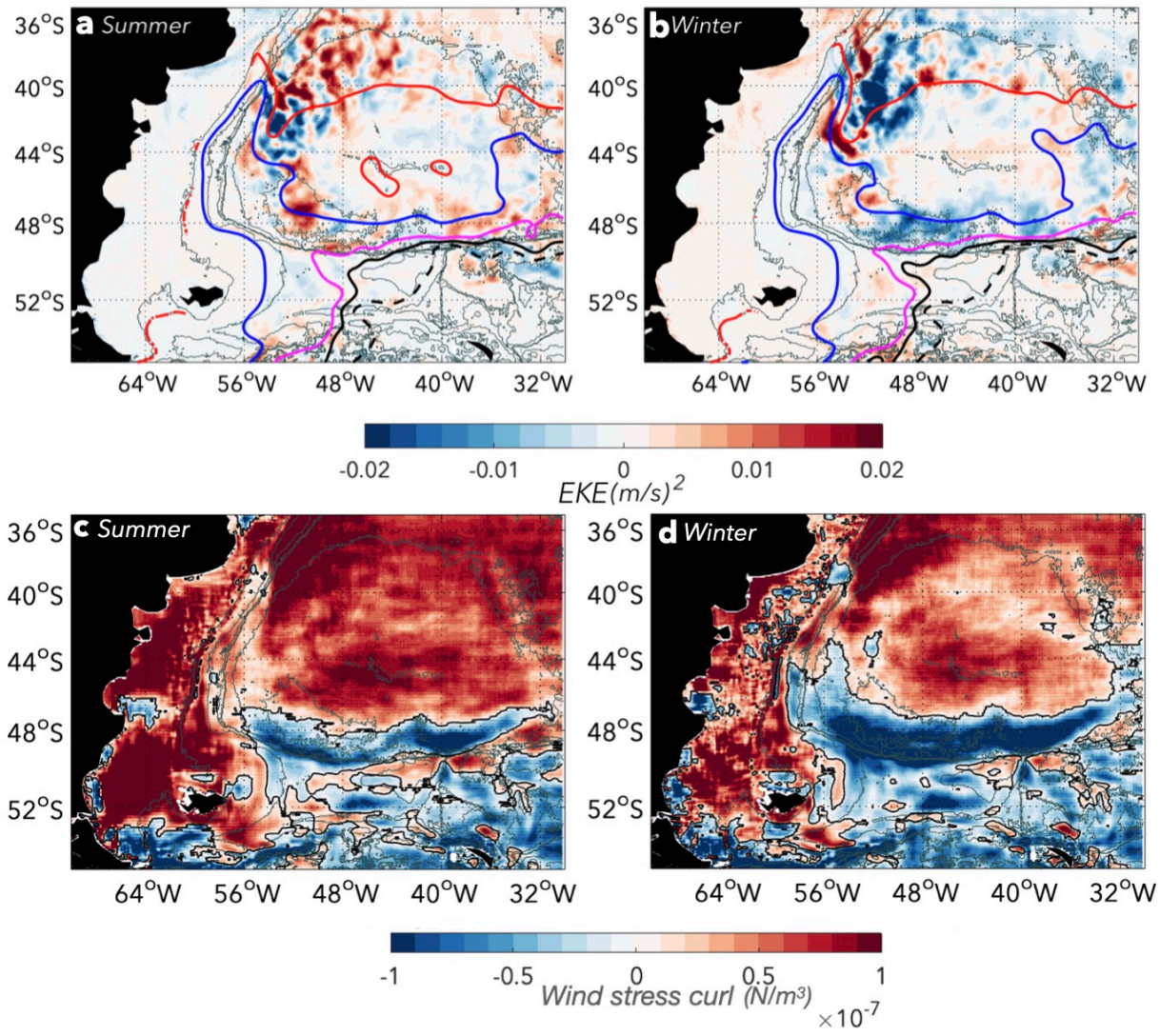

Figure 14: a-b) Seasonal detrended surface EKE anomalies averaged for DJF (a) and JJA (b). c) Mean summer (DJF) detrended Wind Stress Curl. d) Mean winter detrended (JJA) Wind Stress Curl.

presents extreme events (exceeding 1.5 standard deviation, 494 days of strong events and 689 days of weak events), a strong multi-year modulation and a robust negative trend (-15 Sv.$decade^{-1}$).

During strong events (transport $>$ 195.4 Sv), the ZAC shows a well defined coherent gyre. In contrast, during weak events (transport $<$ 49.8 Sv) secondary anticyclonic circulations develop within the ZAC and a cyclonic eddy is located at the center of the ZAC.

During weak events, the ZAC is more permeable to external mesoscale structures. Each weak event features a cyclonic eddy at the center of the ZAC carrying cold and fresh waters. These eddies detach from a SAF meander to the east of the ZAC and enter through the north-east boundary where the planetary vorticity gradient is relatively weak. Strong events are associated with an increase of EKE around the ZAC while weak events are associated with a decrease. As suggested in theoretical studies (e.g Bigorre et al., 2009) the increase of EKE could lead to an enhanced transfer of energy between the mesoscale field and the mean flow. The large-scale WSC seems to modulate the ZAC intensity: the zero isoline of the WSC shifts southward during strong events and northward during weak events. The WSC intensifies over the whole Argentine Basin and above the southern tip of the Subtropical Gyre during strong events while it reduces during weak events (Figure 14 b-c). Interestingly, the mean seasonal patterns of WSC resemble those of the composites of extrema showing a reinforcement during summer and a decrease during winter (Figure 14). This suggests a seasonal preconditioning for the development of extreme events. More strong events occurred in austral summer while more weak events in austral winter (Figure 14a). However, the number of extreme events is rather limited (only 9 strong extreme events and weak events) to perform reliable statistics.

We documented a multi-year modulation of the water masses characteristics in the ZAC. Waters in the ZAC are fresher (-0.75 PSS-78 at 1000 m) and colder ($-0.5°$C at 1000 m) in the period 1998-2003 than in periods 1993-1997 and 2004-2009. The period 1998-2003 corresponds to a reduced mean transport of 101.3 Sv compared to the other periods (160 Sv over 1993-1997 and 126 Sv over 2004-2009). The weak transport period corresponds to a reduction of the large scale circulation (including the Subtropical Gyre) associated to weaker winds and EKE. This period (1998-2003) includes only weak events.

Over the last 27 years, transport time series exhibits a significant negative trend of -15 Sv.$decade^{-1}$ associated with a cyclonic velocity trend pattern in the ZAC coherent in the vertical (see supplementary S5). The ZAC shows a positive temperature trend ($+0.5°$

C.$decade^{-1}$ at 500 m) in the whole water column, a positive salinity trend (+0.1.$decade^{-1}$ at 500 m) in the upper 2000 m and a negative salinity trend between 3000 and 4000 m. The WSC exhibits no change over the ZAC and a positive trend at the periphery. The WSC over the South Atlantic has been shown to contribute to the southward displacement of the STF (Leyba et al., 2019). The southward migration of the Subtropical Gyre induces a negative EKE trend to the northwest of the ZAC and a positive trend to the south of 40° S close to the MC. The negative EKE trend could be a factor leading to the ZAC transport reduction. Anticyclones detaching from the BCO and transporting relatively warm and salty waters could contribute to the positive trends in salinity and temperature within the ZAC in the first 2000 m. Indeed, the ZAC gets more permeable to the surrounding mesoscale features as it weakens (positive trend of EKE at the center of the ZAC).

Climate models project a continuous southward migration of the Subtropical Gyre (e.g. Hewitt et al., 2020) which will increase temperature and salinity in the Argentine Basin. Associated EKE changes could contribute to a reduction of the ZAC transport and a multiplication of collapses episodes.

7 Acknowledgement

We thank to the crews and science parties of the R/V Sarmiento de Gamboa for measurements and Deep Argo float deployment assistance in the Argentine Basin. We are grateful to CNES (Centre National d'Etudes Spatiales) for constant support. This study is a contribution to the CNES-funded BACI project and to the LEFE GMMC BACI project. Léa Poli acknowledges Ph.D support from Sorbonne Université and Camila Artana funding from the Spanish government (AEI) through the 'Severo Ochoa Centre of Excellence' accreditation (CEX2019-000928-S). We thank the editor, Léon Chafik, an anonymous reviewer, and Wilbert Weijer for a number of constructive comments and suggestions.

8 Conflict of Interest

The authors declare no conflicts of interest relevant to this study.

9 Data Availability Statement

Model outputs are available at Copernicus Marine Environment Monitoring Service (CMEMS; https://marine.copernicus.eu). ERA-Interim outputs are available at https://www.ecmwf.int/en/forecasts/datasets/reanalysis-datasets/era-interim. The Argo data used in this study were download from an Argo Global Data Assembly Center in May 2023 (Argo, 2023).

10 References

Argo (2023). Argo float data and metadata from Global Data Assembly Centre (Argo GDAC) [Dataset]. SEANOE. https://doi.org/10.17882/42182

Artana, C., Provost, C., Poli, L., Ferrari, R., Lellouche, J.-M. (2021). Revisiting the Malvinas Current upper circulation and water masses using a high-resolution ocean reanalysis. Journal of Geophysical Research: Oceans, 126, e2021JC017271. https://doi.org/10.1029/2021JC017271

Artana, C., Provost, C., Lellouche, J.-M., Rio, M.-H., Ferrari, R., Sennéchael, N. (2019). The Malvinas Current at the Confluence with the Brazil Current: Inferences from 25 years of Mercator Ocean reanalysis. Journal of Geophysical Research: Oceans, 124, 7178– 7200. https://doi.org/10.1029/2019JC015289

Artana, C., Lellouche, J.-M., Park, Y.-H., Garric, G., Koenig, Z., Sennéchael, N., et al. (2018). Fronts of the Malvinas Current System: Surface and subsurface expressions revealed by satellite altimetry, Argo floats, and Mercator operational model outputs. Journal of Geophysical Research: Oceans, 123, 5261– 5285. https://doi.org/10.1029/2018JC013887

Bigorre, S., 2005. Topographic effects on wind driven oceanic circulation. Ph.D. Thesis, Florida State University, 100pp. Available on line at ⟨http://etd.lib.fsu.edu/theses/available/etd-07052005-163825/unrestricted/pro-dis2E.pdf⟩.

Bigorre, S., & Dewar, W. K. (2009). Oceanic time variability near a large scale topographic circulation. Ocean Modelling, 29(3), 176–188. https://doi.org/10.1016/j.ocemod.2009.04.004

Böning, C., Dispert, A., Visbeck, M. et al. The response of the Antarctic Circumpolar Current to recent climate change. Nature Geosci 1, 864–869 (2008). https://doi.org/10.1038/ngeo362

Coles, V. J., McCartney, M. S., Olson, D. B., Smethie, W. M. (1996). Changes in Antarctic bottom water properties in the western South Atlantic in the late 1980s. Journal of Geophysical Research: Oceans, 101(C4), 8957–8970. https://doi.org/10.1029/95jc03721

Colin de Verdière, A. C., & Ollitrault, M. (2016). A direct determination of the World Ocean barotropic circulation. Journal of Physical Oceanography, 46(1), 255–273. https://doi.org/10.1175/JPO-D-15-0046.1

Dewar, W. K. (1998). Topography and barotropic transport control by bottom friction. Journal of Marine Research, 56(2), 295-328

de Miranda, A. P., Barnier, B., Dewar, W. K. (1999). On the dynamics of the Zapiola Anticyclone. Journal of Geophysical Research: Oceans, 104(C9), 21137-21149.

Durack, P. J., Wijffels, S. E., Matear, R. J. (2012). Ocean salinities reveal strong global water cycle intensification during 1950 to 2000. science, 336(6080), 455-458.

Emery, W. J., & Meincke, J. (1986). Global water masses-summary and review. Oceanologica acta, 9(4), 383-391.

Flood, R.D and Shor A.N, (1988) Mud waves in the Argentine Basin and their relationship to regional bottom circulation patterns, Deep Sea Research Part A. Oceanographic Research https://doi.org/10.1016/0198-0149(88)90070-2.

Fu, L. L. (2007). Interaction of mesoscale variability with large-scale waves in the Argentine Basin. Journal of Physical Oceanography, 37(3), 787-793.

Fu, L.-L., Cheng, B., & Qiu, B. (2001). 25-Day Period Large-Scale Oscillations in the Argentine Basin Revealed by the TOPEX/Poseidon Altimeter. Journal of Physical Oceanography, 31(2), 506–517. https://doi.org/10.1175/1520-0485(2001)031¡0506:DPLSOI¿2.0.CO;2

Hewitt, H.T., Roberts, M., Mathiot, P., et al., (2020).Resolving and Parameterising the Ocean Mesoscale in Earth System Models. Curr. Clim. Change Rep 6, 137–152. https://doi.org/10.1007/s40641-020-00164-w

Hughes, C. W., Stepanov, V. N., Fu, L. L., Barnier, B., Hargreaves, G. W. (2007). Three forms of variability in Argentine Basin ocean bottom pressure. Journal of Geophysi-

cal Research: Oceans, 112(C1).

Johnson, G. C., King, B. A. (2023). Zapiola Gyre, velocities and mixing, new Argo insights. Journal of Geophysical Research: Oceans, 128(6), e2023JC019893. doi: 10.1029/2023JC019893.

Johnson, G. C. (2022). Antarctic Bottom Water Warming and Circulation Slowdown in the Argentine Basin From Analyses of Deep Argo and Historical Shipboard Temperature Data. Geophysical Research Letters, 49(18), e2022GL100526. doi: 10.1029/2022GL100526.

Lellouche, J.-M., Greiner, E., Romain B-B, Gilles G, Angélique M, Marie D, Clément B, Mathieu H, Olivier LG, Charly R, Tony C, Charles-Emmanuel T, Florent G, Giovanni R, Mounir B, Yann D and Pierre-Yves LT (2021) The Copernicus Global 1/12° Oceanic and Sea Ice GLORYS12 Reanalysis. Frontiers in Earth Science. 9:698876. doi: 10.3389/feart.2021.698876

Lellouche, J.-M., Greiner, E., Le Galloudec, O., Garric, G., Regnier, C., Drevillon, M., Benkiran, M., Testut, C.-E., Bourdalle-Badie, R., Gasparin, F., Hernandez, O., Levier, B., Drillet, Y., Remy, E., and Le Traon, P.-Y., (2018).Recent updates to the Copernicus Marine Service global ocean monitoring and forecasting real-time 112° high-resolution system, Ocean Science, 14, 1093–1126, https://doi.org/10.5194/os-14-1093-2018.

Leyba, I. M., Solman, S. A., Saraceno, M. (2019). Trends in sea surface temperature and air–sea heat fluxes over the South Atlantic Ocean. Climate Dynamics, 53, 4141-4153. https://doi.org/10.1007/s00382-019-04777-2

Li, Q., England, M. H., Hogg, A. M., Rintoul, S. R., & Morrison, A. K. (2023). Abyssal ocean overturning slowdown and warming driven by Antarctic meltwater. Nature, 615(7954), 841-847.

Maamaatuaiahutapu, K., Garçon, V., Provost, C., & Mercier, H. (1998). Transports of the Brazil and Malvinas Currents at their Confluence. Journal of Marine Research, 56(2), 417-438

Madec, G. (2008). NEMO reference manual, ocean dynamic component: NEMO–OPA, Note du Pôle de modélisation, Institut Pierre Simon Laplace (No. 27). Technical Report 27, Note du pôle de modélisation, Institut Pierre Simmon Laplace, France.

Martínez-Moreno, J., Hogg, A.M., England, M.H. et al. Global changes in oceanic mesoscale currents over the satellite altimetry record. Nature Climate Change 11, 397–403 (2021). https://doi.org/10.1038/s41558-021-01006-9

Mason, E., Pascual, A., Gaube, P., Ruiz, S., Pelegrí, J. L., and Delepoulle, A. (2017), Subregional characterization of mesoscale eddies across the Brazil-Malvinas Confluence, Journal of Geophysical Research: Oceans, 122, 3329– 3357, doi:10.1002/2016JC012611.

Naveira Garabato, A. C., L. Jullion, D. P. Stevens, K. J. Heywood, and B. A. King, 2009: Variability of Subantarctic Mode Water and Antarctic Intermediate Water in the Drake Passage during the Late-Twentieth and Early-Twenty-First Centuries. Journal of Climate, 22, 3661–3688, https://doi.org/10.1175/2009JCLI2621.1.

Ollitrault, M., & Rannou, J.-P. (2013). ANDRO: An Argo-Based Deep Displacement Dataset. Journal of Atmospheric and Oceanic Technology, 30(4), 759–788. https://doi.org/10.1175/JTECH-D-12-00073.1

Peterson, R. G., (1992) The boundary currents in the western Argentine Basin, Deep Sea Research, 39, 623-644.

Poli, L., Artana, C., Provost, C., Sirven, J., Sennéchael, N., Cuypers, Y., Lellouche, J.-M. (2020). Anatomy of subinertial waves along the Patagonian shelf break in a 1/12° global operational model. Journal of Geophysical Research: Oceans, https:// doi.org/10.1029/2020JC016549

Preu, B., Hernández-Molina, F. J., Violante, R., Piola, A. R., Paterlini, C. M., Schwenk, T., et al. (2013). Morphosedimentary and hydrographic features of the northern Argentine margin: The interplay between erosive, depositional and gravitational processes and its conceptual implications. Deep Sea Research Part I: Oceanographic Research Papers, 75, 157– 174. https://doi.org/10.1016/j.dsr.2012.12.013

Purich, A. (2018). Understanding the drivers of recent Southern Ocean sea ice and surface temperature trends (Doctoral dissertation, UNSW Sydney).

Saraceno, M., Provost, C., & Zajaczkovski, U. (2009). Long-term variation in the anti-cyclonic ocean circulation over the Zapiola Rise as observed by satellite altimetry: Evidence of possible collapses. Deep Sea Research Part I: Oceanographic Research Papers, 56(7), 1077–1092. https://doi.org/10.1016/j.dsr.2009.03.005

Saunders, P.M., and King, B.A. ,(1995). Bottom currents derived from a shipborne ADCP on WOCE cruise A11 in the South Atlantic, Journal of Physical Oceanography, 25, 329-347.

Schmid, C., & Majumder, S. (2018). Transport variability of the Brazil Current from observations and a data assimilation model. Ocean Science, 14(3), 417-436.

Spadone, A., and Provost, C. (2009). Variations in the Malvinas Current volume transport since October 1992, Journal Geophysical Research., 114, C02002, doi:10.1029/2008JC004882.

Valla, D., Piola, A. R., Meinen, C. S., Campos, E. (2018). Strong mixing and recirculation in the northwestern Argentine Basin. Journal of Geophysical Research: Oceans, 123(7), 4624-4648.

Venaille, A., Le Sommer, J., Molines, J.-M., and Barnier, B. (2011). Stochastic variability of oceanic flows above topography anomalies, Geophysical Research Letters, 38, L16611, doi:10.1029/2011GL048401.

Volkov, D. L., and Fu,L.-L (2008). The role of vorticity fluxes in the dynamics of the Zapiola Anticyclone, Journal Geophysical Research, 113, C11015, doi:10.1029/2008JC004841.

Weatherly, G., (1993). On deep-current and hydrographic observations from a mudwave region and elsewhere in the Argentine Basin, Deep Sea Research, Part II, 40, 939-961.

Weijer, W., Barthel, A., Veneziani, M., & Steiner, H. (2020). The Zapiola Anticyclone: A Lagrangian study of its kinematics in an eddy-permitting ocean model. Deep Sea Research Part I: Oceanographic Research Papers, 164, 103308.
https://doi.org/https://doi.org/10.1016/j.dsr.2020.103308

Weijer, W., Maltrud, M.E., Homoky, W.B., Polzin, K.L., Maas, L.R., (2015). Eddy-driven sediment transport in the Argentine Basin: is the height of the Zapiola Rise hydrodynamically controlled? Journal of Geophysical Research.: Oceans 120, 2096–2111.
https://doi.org/10.1002/2014JC010573.

Weijer, W., Vivier, F., Gille, S. T., Dijkstra, H. A. (2007). Multiple oscillatory modes of the Argentine Basin. Part I: Statistical analysis. Journal of Physical Oceanography, 37(12), 2855-2868.

Whitworth T., III, W. D. Nowlin Jr., R. D. Pillsbury, M. I. Moore, and R. F. Weiss, (1991). Observations of the Antarctic Circumpolar Current and deep boundary current in the southwest Atlantic, Journal of Geophysical Research, 96, 15,105-15,118.

Yu, L., Josey, S. A., Bingham, F. M., Lee, T. (2020). Intensification of the global water cycle and evidence from ocean salinity: A synthesis review. Annals of the New York Academy of Sciences, 1472(1), 76-94. https://doi.org/10.1111/nyas.14354

Yu, Y., Chao, B. F., García-García, D., Luo, Z. (2018). Variations of the Argentine Gyre observed in the GRACE time-variable gravity and ocean altimetry measurements. Journal of Geophysical Research: Oceans, 123(8), 5375-5387.

Collapses, maxima, multi-year modulation and trends of the Zapiola anticyclone: insights from Mercator Reanalysis.

Lea Poli[1], Camila Artana[2], Christine Provost[1], Jérôme Sirven[1] and Ruben Le Blanc-Pressenda[1]

[1]LOCEAN-IPSL, Sorbonne Université (UPMC), Paris, France

[2]Institut de ciences del Mar, Barcelona, Spain

Additional Supporting Information (Files uploaded separately)

1. Further Model Assessment.
2. Volume transport of the Zapiola anticyclonic circulation: spectral content.
3. Water masses definition.
4. Trends in the Argentine Basin: Velocities, Temperature and Salinity.

1. Further model assessment

We compare PSY4 Temperature, Salinity and velocities with data from the SAGA10W cruise (CTD/LADCP) and deep Argo float data.

Figure S1 and Table S1 feature hydrographic comparison. Figure S2 explains how velocities are estimated and Figure S3 compares velocities. Overall, we find good agreement between model fields and data.

:

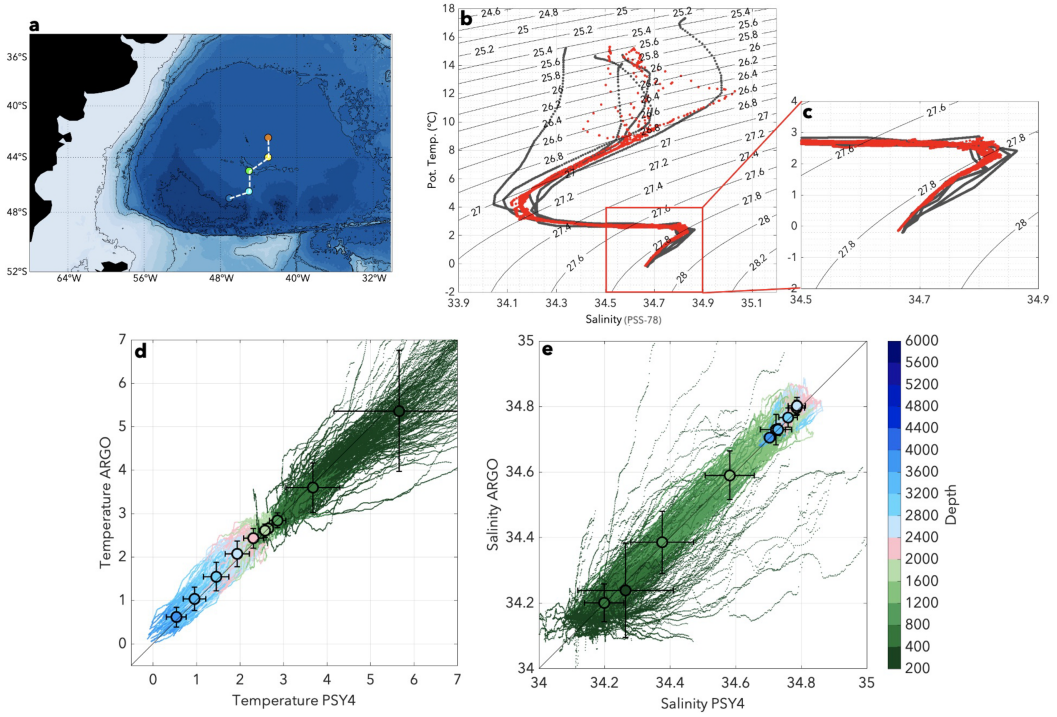

Figure S1: a) Location of the 5 SAGA10W CTD stations in the ZAC b) Potential Temperature/Salinity diagram for the 5 CTD stations in red and colocated model variables in grey. c) Zoom on deep waters. d-e) Scatter plots of the T (d)/S (e) profiles for the 5 deep floats first 6 months after deployment (5 days sampling, 185 profiles) after deployment and colocated PSY4 fields. Means and standard deviations computed every 400 m are reported in the table below. Means are represented with colored dots and horizontal (vertical) bars represent the standard deviation of model fields (measurements).

:

Table S1:

depth	Argo		PSY4		Argo-PSY4	
	T	S	T	S	T	S
400-800m	3.59/1.40	34.20/0.058	3.68/0.62	34.20/0.059	-0.09	0.00
800-1200m	2.84/0.17	34.39/0.095	2.87/0.19	34.38/0.096	-0.03	0.01
1200m-1600m	2.66/0.10	34.59/0.074	2.65/0.10	34.58/0.075	0.01	0.01
1600m-2000m	2.61/0.15	34.73/0.047	2.58/0.15	34.72/0.048	0.03	0.01
2000m-2400m	2.43/0.23	34.80/0.023	2.31/0.23	34.79/0.024	0.12	0.01
2400m-2800m	2.07/0.30	34.80/0.025	1.94/0.28	34.79/0.026	0.13	0.01
2800m-3200m	1.55/0.33	34.76/0.029	1.46/0.29	34.76/0.028	0.09	0.00
3200m-3600m	1.03/0.27	34.73/0.018	0.96/0.26	34.73/0.022	0.07	0.00
3600m-4000 m	0.61/0.23	34.71/0.012	0.54/0.23	34.7/0.015	0.07	0.01

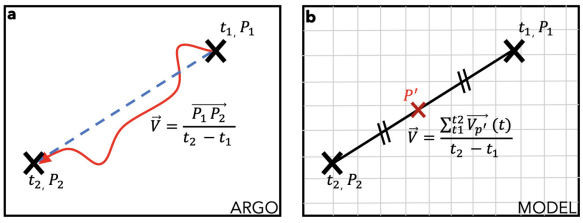

Figure S2: Schematics of the velocity computation methods. a) Estimation from Argo floats. We assume that the trajectory is straight (blue dashed line) between two profiles (indicated with black crosses). The red line illustrates the unknown drift trajectory. b) Estimation from model. We consider the velocity at the midposition between the two profiles and we average it over 5 days (time between 2 profiles).

:

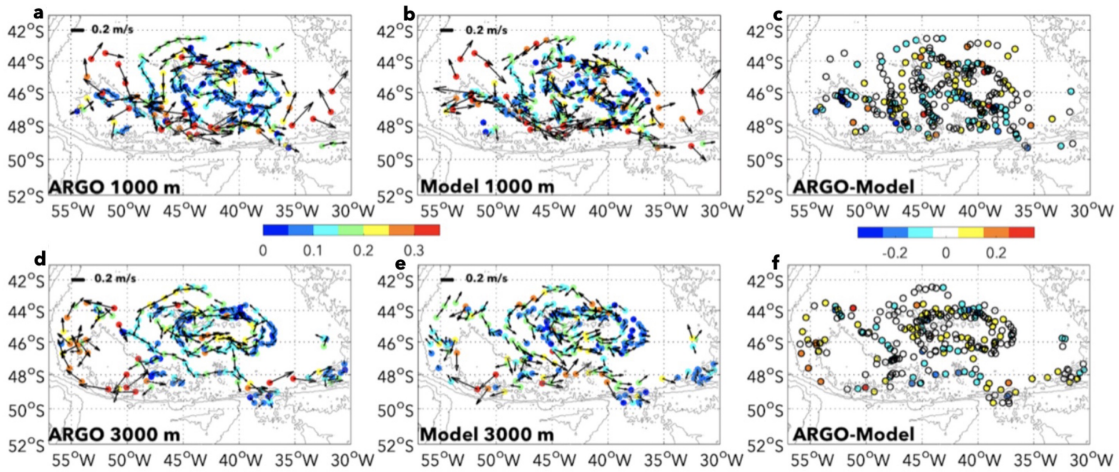

Figure S3: a) 1000 m velocities (arrows) estimated from the Argo floats and velocity norms (colour in m/s). b) Corresponding model velocities and their norm. c) Differences between estimated and modelled velocity norms. d-e-f) Same as a-b-c) but from the deep Argo trajectories (3000 m).

2. Volume transport of the ZAC: spectral content

The volume transport time series with a daily resolution is shown in figure S4a). The time series is dominated by peaks with periods around 20 days, between 40 and 60 days and at 70, 100, 220 and 333, and 750 (Figure S4b). Peaks at periods smaller that 90 days have been examined in Fu et al.,[2001], Weijer et al., [2007]. Peaks at 220 and 333 days correspond to the semi-annual and annual cycles respectively.

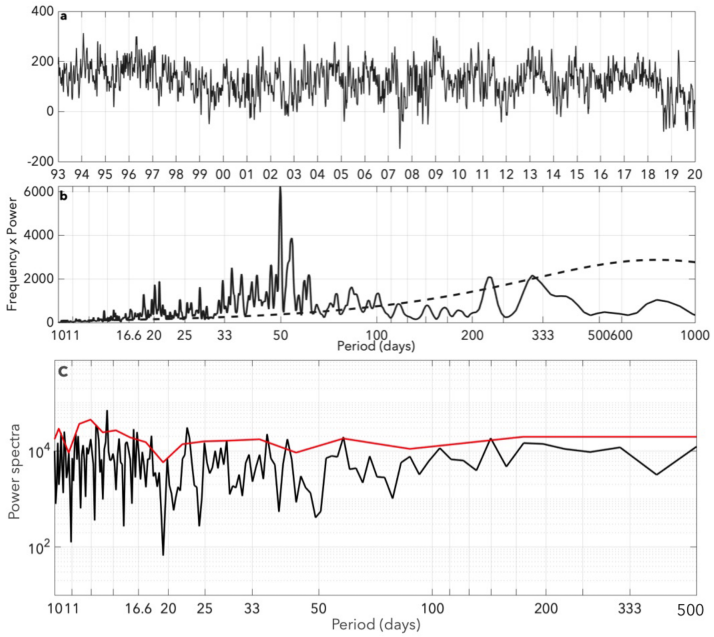

Figure S4: a) Daily resolution ZAC transport time series in Sv computed as described in section 3.2. b) Variance preserving spectrum for the ZAC transport averaging over a group of five adjacent frequencies. The dashed line shows the 95% confidence level against the red noise background from a first-order autoregressive (AR-1) process.c) Multitaper spectrum for the full transport time series in black. The red line corresponds to the 95 percentile of 5 spectra computed over 5 years periods. Two spectra computations are shown since variance preserving spectrum enhances the energy of the high frequency peaks.

3. Water mass definition

:

Table S2: Water mass definition and references. Tropical Water (TW). South Atlantic Central Water (SACW). Antarctic Intermediate Water (AAIW). Upper Circumpolar Deep Water (UCDW). Circumpolar Deep Water (CDW). North Atlantic Deep Water (NADW). Lower Circumpolar Deep Water (LCDW). Antarctic Bottom Water (AABW).

Water Mass	γ^n (g/kg)	S (PSS-78)	θ (°C)	References
TW	<26.35	>34.8		Valla et al. 2018
SACW	<27.1	34.25-34.8	>8	Preu et al. 2013; Valla et al. 2018
SASW	<27.1	<34.25	3-10	Emery & Meincke, 1986
AAIW	27.1-27.6	33.9-34.25		Preu et al. 2013; Valla et al 2018
UCDW	27.6-27.9			Valla et al 2018
CDW/NADW	27.9-28.1	NADW >34.8	2-3.5	Preu et al. 2013; Valla et al. 2018
LCDW	28.1-28.27	<34.8	2-3.5	Preu et al. 2013; Valla et al. 2018
AABW	>28.27	>34.68	<0	Preu et al. 2013

:

4. Velocity, temperature and salinity trends over 27 years

Trends are considered significant when their absolute value exceeds the interannual standard deviation. A strong positive trend (+0.1 (m/s).$decade^{-1}$s, Figure S5a) at 56°W along the slope corresponds to the southward shift of the BC. It is associated with a cyclonic pattern at the confluence (+0.1 (m/s).$decade^{-1}$s, Figure S5a) correponding to the southward migration of the overshoot. Jets along the Malvinas escarpment exhibit a positive trend (+0.05 (m/s).$decade^{-1}$s). A cyclonic trend signs at the surface and near the bottom in the core of the ZAC (Figure S5 a and b) and corresponds to a weakening of the circulation.

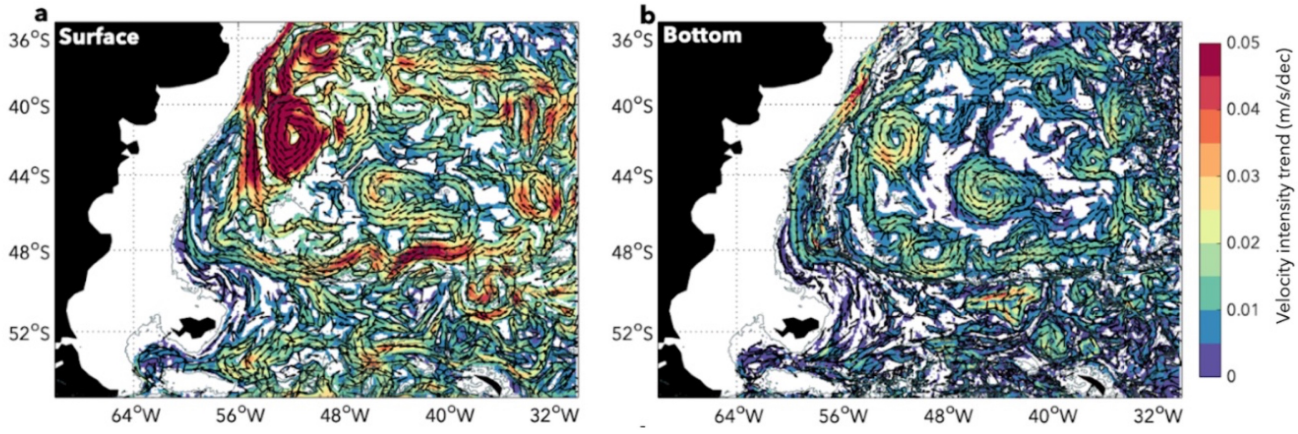

Figure S5: Horizontal velocity linear trends over the period 1993-2019 from GLORYS12 for surface (a) and bottom (b). Colors represent the amplitude of the horizontal velocity trends computed as $\sqrt{trend(u)^2 + trend(v)^2}$. Arrows (all of the same size) indicate the direction of the speed trend. Thick black lines indicate regions where the absolute value of the trend exceeds the interannual standard deviation. White color corresponds to non significant trends.

Significant positive temperature trends are found to the north of the SAF down to 1500 m (see Figure S6 a, which illustrates this at 541 m) (+0.5 to +1 °C.$decade^{-1}$s at 541m and along the zonal section). At depth, the trends in the subtropical gyre reach +1°C.$decade^{-1}$s (Figure

:

S6 a). The strong positive temperature trends down to 1500 m depth (Figure S6 b and c) could be the consequence of the southward shift of the warm subtropical gyre. In terms of salinity, the MC shows a negative trend reaching -0.05 PSS-78.$decade^{-1}$s Figure S5 c and d) associated to the freshening of the AAIW while the Basin interior shows positive trends reaching +0.2 PSS-78.$decade^{-1}$s in the BC (Figure c) probably associated to the salty waters coming from the north.

:

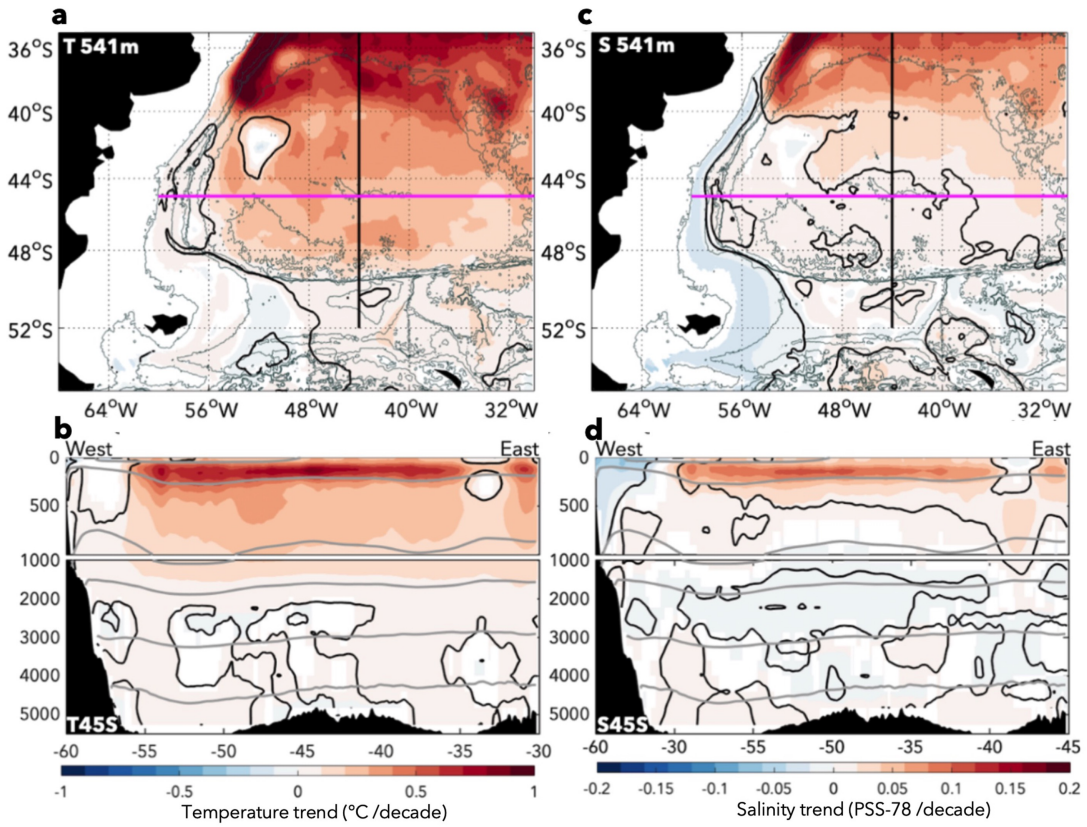

Figure S6: Linear trends over the period 1993-2020 for temperature and salinity a) Temperature at 541m. c) Salinity at 541m. b-d) Linear trends of temperature and salinity along 45°S section (Magenta in a and b). Thick gray contours are the mean gamma-n bounding the water masses (Table S2). Statistically significant values are shaded. Thick black lines indicate regions where the absolute value of the trend exceeds the interannual standard deviation.

Chapter 5

Conclusions and perspectives

5.1 Conclusions

In this thesis we examined some elements of ocean circulation in the Argentine Basin related to topography (mainly waves and currents). Due to the lack of in-situ observations in this region, we used a 27-year-long global ocean reanalysis (GLORYS12, daily fields with a spatial resolution of 1/12°). We compared the model outputs to several data sets coming from in-situ observations (moored current meter measurements along the Patagonian Platform, hydrographic properties from ARGO float data, tide gauges data) and satellite observations (sea level). Overall, we found a good agreement.

We first studied the various waves propagating along the sinuous Patagonian slope (Poli et al., 2020). We evidenced the presence of **slow waves** with the following properties :

- They propagate in the core of the MC above the 1500 m isobath.
- They have phase velocities ranging between 0.10 and 0.30 m/s, periods around 20, 60 and 100 days and wavelengths ranging from 450 to 1200 km.
- They can be tracked back to Drake Passage and the Malvinas Escarpment.
- They modulate the intensity of the main jet of the MC (offshore jet).

We also evidenced the presence of **fast waves** propagating along the shelf break.

- They have phase velocities ranging between 1.4 m/s and 3 m/s, periods ranging from 5 to 110 days

and wavelengths around 1500 km, matching the spatial scale of upwelling events documented along the Patagonian shelf.

- Their characteristics depend upon stratification, slope, shelf width, latitude and mean flow and correspond to mode 3-4 according to linear theory (see Appendix).
- They generate anomalies of vertical and cross-shore velocities and could enhance the nutrient supply to the platform (Figure 5.1b-c). The associated positive vertical velocities combined with anomalies of in-shore velocities could transport nutrients from the MC to the Patagonian shelf.
- They modulate the intensity of the in-shore jet of the MC (Figure 5.1b-c).
- Fast waves with periods between 5 and 40 days are often locally forced by strong variations of the zonal wind south of 47°S (Figure 5.1a).

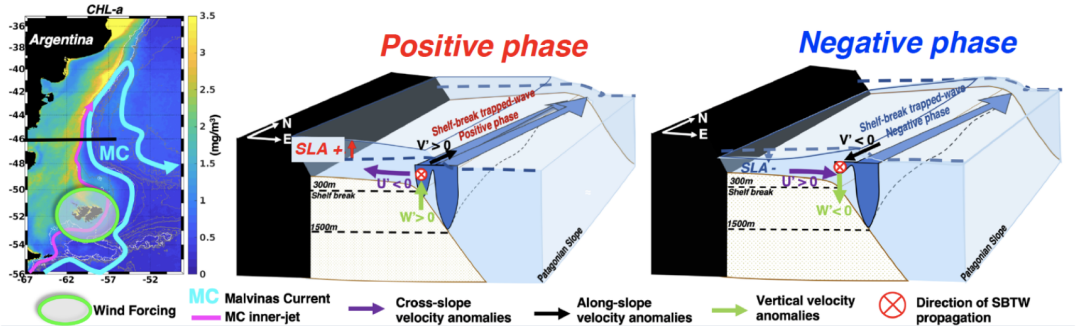

Figure 5.1: Wind-forced shelf-break trapped-waves modulate the intensity of the inner jet. Associated vertical and cross-shelf velocities bring nutrients to the Patagonian platform enhancing primary productivity.

We extended our analysis to the entire South American coast from the Pacific to the Atlantic and highlighted an oceanic teleconnection between the Equatorial Pacific and the Tropical Atlantic through topographically trapped waves (TW) (Poli et al. 2022).

- TWs propagate from the equatorial Pacific to the tropical Atlantic (22°S) where a part of their energy is dissipated due to the abrupt changes in shelf width and slope steepness.
- Their phase velocities range from 1.8 to 7 m/s depending upon local background characteristics. They reach 7 m/s over the Patagonian Platform where the slope is gentle and the shelf is wide (> 1000 km width at some points).

- The vertical structure of the waves varies during their propagation due to changes in background characteristics . Energy scattering between modes occurs: on the Pacific side and off Brazil, the waves have a baroclinic structure (the slope is steep) whereas the structure is rather barotropic along the Patagonian slope.

- The phase speeds and the spatial structures correspond to theoretical modes 1–2 on the Pacific side and off Brazil correspond to theoretical modes 2–3 along the Patagonian Platform (see appendix)

- The Madden-Julian Oscillation (MJO) plays a key role in forcing the TWs in two ways (a) through an oceanic connection implying equatorial Kelvin waves reaching the western American Coast and (b) through an atmospheric teleconnection enhancing southerly winds in the south-east Pacific.

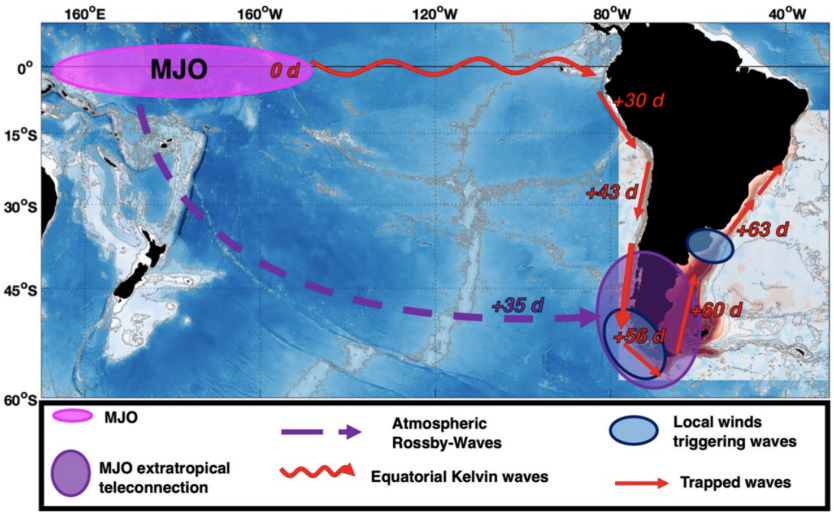

Figure 5.2: Schematics of mechanisms forcing TW around South America from Poli et al., [2022]. MJO is a key player in triggering TW around South America through equatorial oceanic Kelvin waves (red) and atmospheric Rossby waves (dashed purple line). Lags (red) in days are deduced from the correlation between the MJO and the SLA over the track following the 300 m isobath. Lag in days (purple) are deduced from the regression between meridional winds and the MJO index. The associated wind signal is represented with the purple circle. Local wind forcing (in blue), not linked with the MJO, reinforce and/or generate TWs.

- Furthermore, local winds, not necessarily linked with the MJO, modulate and trigger waves in specific locations, such as the BMC (Figure 5.2).

- The wave activity is enhanced during positive ENSO phase connecting the Equatorial Pacific to the Tropical Atlantic.

- Trapped waves impact the along-shore currents. During the positive phase of the waves the near-surface flow is enhanced by about 0.1 m/s.

In chapter four we examined another topographically related feature, the ZAC located at the center of the Argentine Basin above a sedimentary deposit (Poli et al., 2023, submitted). We studied the vertical structure of the ZAC over 27 years (1993-2019) and focused on the low-frequency variability (> 90 days). We could highlight the following features :

- The ZAC is reinforced at depth with bottom currents reaching 0.10 m/s.
- The ZAC transport has a mean of 122.6 Sv and a standard deviation of 48.5 Sv. Extremes peak at -18 Sv and 250 Sv.
- Extreme events with large transport are associated with stronger transient kinetic energy (TKE) at the periphery of the ZAC (especially to the west and south).
- In contrast during weak transport events, TKE increases in the center of the ZAC and decreases at the periphery.
- During weak events, the ZAC is more permeable to external mesoscale structures and receives the influence of surrounding waters. Each weak event features a cyclonic eddy at the center of the ZAC carrying cold and fresh waters. These eddies detach from a subantarctic front meander to the east of the ZAC and enter through the north-east boundary where the planetary vorticity gradient is relatively weak.
- The wind seems to play a role in the preconditioning and seasonal distribution of extreme events (more weak events in austral summer).
- The water masses characteristics of the Argentine basin and the ZAC exhibit a multi-year modulation of 4-5 years. During 1993-1997 and 2004-2009 the salinity anomaly is high while during 1998-2003 the salinity anomaly is low in the first 2000 m. These periods correspond to a large and low transport means respectively (160 Sv for period 1993-1997, 126 Sv for period 2004-2009 and 101.3 Sv for period 1998-2003).

- Over the last 27 years, waters of the Argentine basin became warmer and saltier in the first 2000 m of the water column. These trends are concomitant with an increase of transient kinetic energy in the south-west of the basin which is probably associated with the southward migration of the subtropical front.

- Over the last 27 years, the transport exhibit a robust negative trend of -15 Sv/decade.

5.2 Perspectives on waves

5.2.1 Origins of slow waves in the core of the MC

The slow waves propagating in the core of the MC identified in Poli et al., [2020] using model outputs have also been observed in satellite observations and mooring measurements (Paniagua et al., 2021). Further study is needed to understand the nature of these waves and how they are generated along the Malvinas Escarpment and at the entrance from Drake Passage to the Argentine Basin. The strong mesoscale activity associated to the ACC in Drake Passage could be a source of a part of these waves. Indeed, the passages across the North Scotia Ridge (EBB and SRP) could filter specific frequencies and generate the waves; transmission mechanisms should be carefully studied.

The other part of these waves have been tracked back to the Malvinas Escarpment and the generation mechanism have not yet been studied.

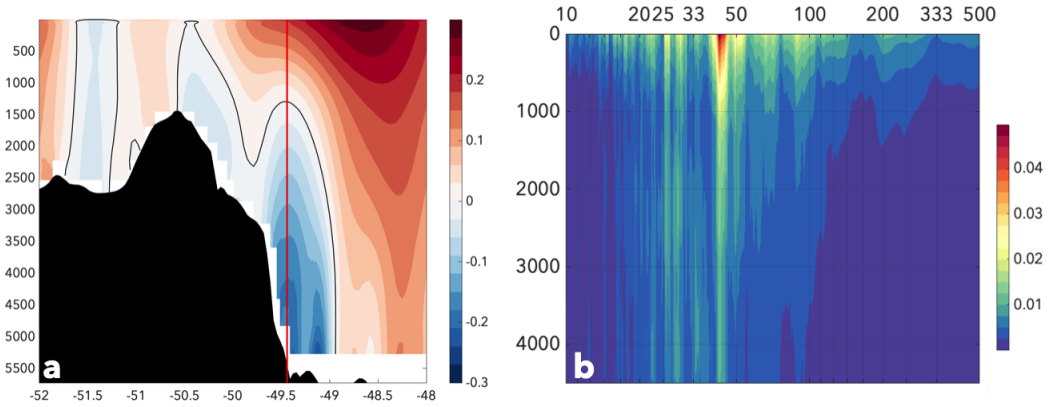

Figure 5.3: a) Mean zonal velocities along the Malvinas Escarpment at 45°W in m/s. The black contour correspond to the Zero velocity. b) Variance-preserving spectra in $(m/s)^2$ as a function of depth at the location of the vertical red line in panel a.

Along the Malvinas Escarpment there is a strong vertical velocity shear between the jets following the

PF and the SAF and a deep counter current (Figure 5.3a). This shear could induce baroclinic instability at the origin of the slow waves reaching the Patagonian Slope. Variance preserving spectra as a function of depth (Figure 5.3b) show peaks in the whole water column at periods between 30 and 90 days which could be the signature of the slow waves.

The impact of these waves on the position of the confluence should be also investigated. Indeed, Artana et al., [2019] described transport extrema at 41°S associated with propagating mesoscale features from the south. In addition, the propagation of anticyclonic eddies along the Malvinas escarpment, leading to blocking events (Artana et al., 2018), should be studied.

5.2.2 Fast Waves along the Patagonian Platform

Several aspects of the fast waves deserve further investigation. Are there fast waves propagating north of 22°S? How is their energy dissipated ? What can we learn on fast waves from the daily SWOT Data ? What is the link between the wave activity and primary production ?
Waves with periods of 40-130 days have more energy and are less dispersive than the higher frequency waves. Even if part of the signal is lost at 22°S after the Abrolhos plateau, some energy is transmitted northward and can reach the Equatorial Atlantic. As an example, we show in figure 5.4 a time-distance diagram from the Equatorial Pacific to the tropical Atlantic (Figure 5.4 a). The wave generated in May 2015 in the equatorial Pacific (marked with a dashed black line in Figure 5.4 b) crosses the BMC, the Abrolhos plateau, reaches the Equatorial Atlantic and continues propagating along the Equatorial Atlantic untill the Gulf of Guinea.

Waves could be reinforced during their path by local phenomena such as local wind forcing. A dedicated study of the evolution and the impact of those waves in the tropical Atlantic is needed.

Waves energy drastically reduces to the north of 22°S, where the Brazilian continental shelf steepens and narrows (De Freitas et al., 2021, Poli et al., 2022). The waves energy loss and scattering at this latitude should be investigated. This could be done with the help of a high-resolution regional model such as the one we developp with Camila Artana with the help of the Mercator Ocean team. This model has a 1/36° resolution and is forced at the boundaries by the operational model with a 1/12° resolution (PSY4) and by the ECMWF-IFS simulation at the surface. The region is between 10°S and 30°S and 54°W and 30°W (Figure 5.5). The more precise study of the dispersion of slope waves (described in

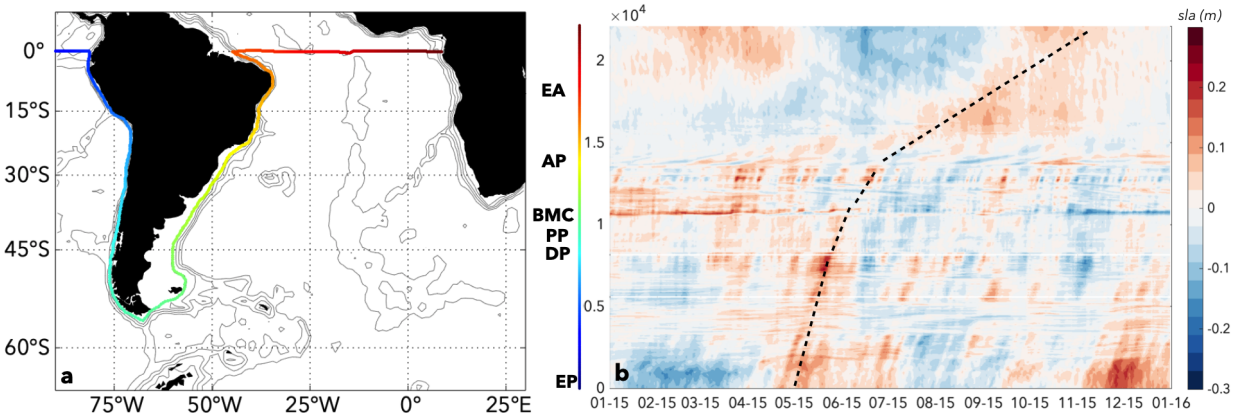

Figure 5.4: a) The colored track follows the 300 m isobath marking the shelf break. b)Time-distance diagram of Sea Level Anomaly (in m) in 2015 from GLORYS12 daily outputs. The locations of EP (Equatorial Pacific), DP (Drake Passage), PP (Patagonian platform), BMC (Brazil Malvinas Confluence), AB (Abrolhos Plateau), EA (Equatorial Atlantic) are indicated. The colorbar to the left is the reported distance in km as in panel a). The May wave is indicated with the dashed black line.

Poli et al., 2022 and De Freitas et al., 2021) when they arrive at the Abrolhos plateau was one of the motivation of the choice of the region. We ran two twin simulations: one with 6 tidal harmonics and one without tides between January 1, 2018 and December 31, 2019. The model is initialized with PSY4 fields from December 31, 2017. The model comprises 50 vertical levels (with finer resolution close to the surface).

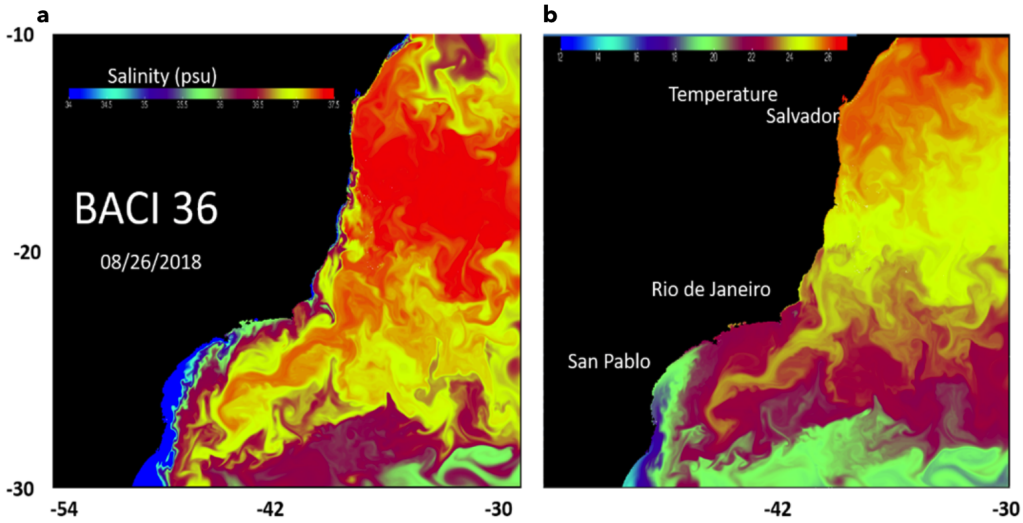

Figure 5.5: Synoptic fields of a) Salinity and b) temperature the 26/08/2018 from the run BACI36 without tide.

We show that trapped waves could impact the cross-shelf exchanges, through the anomalies of cross-shore and vertical velocities, by modulating the MC intensity. However, the impact of fast waves on the

primary productivity must be more deeply analyzed with the help of chlorophyll maps.

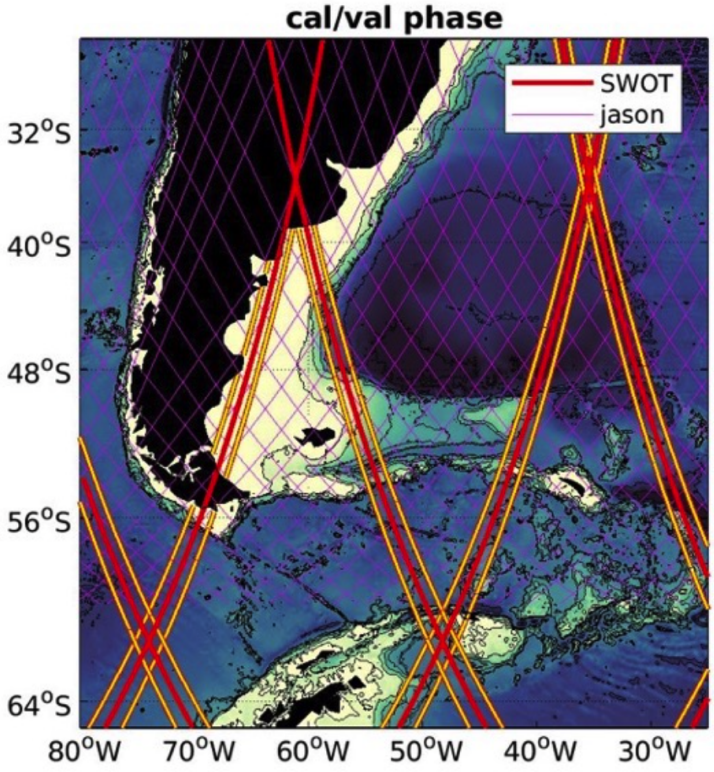

Figure 5.6: Jason tracks over the region in magenta and SWOT tracks during the CALVAL period crossing the Patagonian slope and the Malvinas Escarpment.

The SWOT (Surface Water Ocean Topography) satellite was launched December 16, 2023. During its initial Calibration/Validation (CALVAL) period with a daily resolution a SWOT track intercepts the Patagonian slope between 55°S and 41°S (Figure 5.6). The 1-day repetition phase will enable to examine the rapid evolution of structures (waves) which have energy at periods lower than 20 days. The CALVAL period corresponds to the austral summer, when cloud cover is minimal, a favorable situation for the joint examination of high-resolution satellite imagery (SST and water color). The signals from imagery will provide complementary information as, unlike SSH, SST is not affected by the signal from internal tides (Ponte et al., 2017).

5.3 Perspectives on the Zapiola anticyclonic circulation and the Argentine Basin.

5.3.1 Bottom circulation in the Argentine Basin.

The bottom circulation of the Argentine Basin is intense and is still poorly documented. Dedicated studies are needed to understand and monitor the elements of deep circulation which are of primary importance for the global climate. This could be done with the help of GLORYS12 and the deep ARGO floats measurements. The strong deep cyclonic circulation (DCC) fed by the deep waters (Figure 5.7) entering the basin through a gap in the Malvinas Plateau at 40°W (magenta arrow in Figure 5.7) should be deeply studied. The link between the ZAC and the DCC should also be characterized.

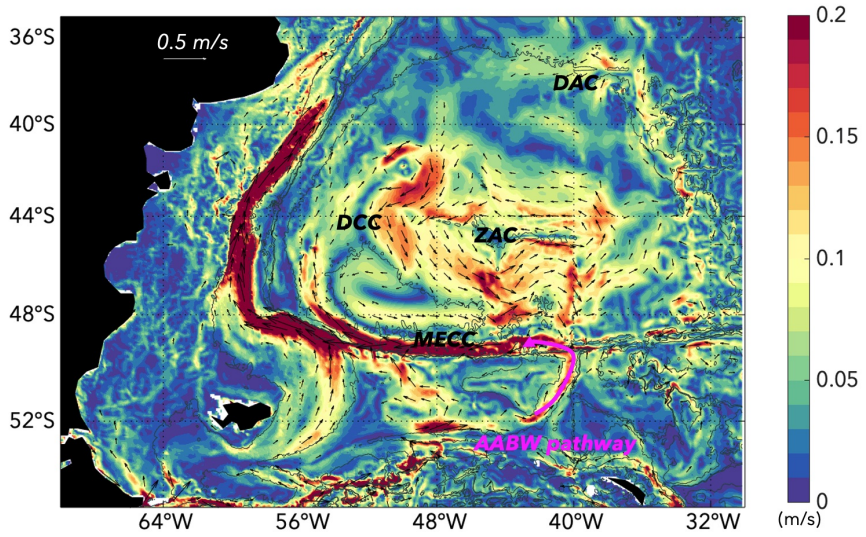

Figure 5.7: Schematics of the circulation cells and elements that should be investigated more deeply. Mean velocities near the bottom (amplitude in color) from GLORYS12 reanalysis (1993-2019). Thin grey lines mark the 200, 2000, 3400, 3800, 3900, 5000, and 6000 m isobaths. Only velocities exceeding 0.05 m/s are plotted.

5.3.2 High frequency modes of variability within the Basin

Barotropic Modes of variability with periods of 20-30 days in the Argentine Basin have been documented (Weijer et al., 2007 a and b) from satellite altimetry (Fu et al., 2001), bottom current measurements (Weatherly, 1993) and bottom pressure gauges (Hughes et al., 2007). The precise vertical structure

associated with these modes should be investigated. The role of these modes on the ZAC transport variability and in the water mass stirring needs further studies.

5.3.3 Water masses transformation in the Argentine Basin.

The Argentine Basin plays a key role in the global deep waters characteristics as it is a mixing hotspot. Indeed, strong mixing have been documented in the Argentine Basin especially at the BMC (Valla et al., 2018) and along the western boundary where the North Atlantic Deep Waters mixes with the fresher Circumpolar deep waters (Brand et al., 2023). As the deep circulation is mostly controlled by the thermohaline characteristics of the waters, documenting the water masses transformation is crucial for the global circulation understanding. Dissipation rate and diffusivity (using the strain method) can be inferred from ARGO profiles (e.g Whalen et al., 2012 and 2018) and a dedicated study in Argentine Basin is needed.

We investigate the mean vertically transport integrated in each water mass layer. The water masses are advected by different circulations cells which affect the water characteristics of the Argentine Basin. This point should be carefully investigated. A particular focus should be done on the variability of the DCC, the ZAC and the DAC.

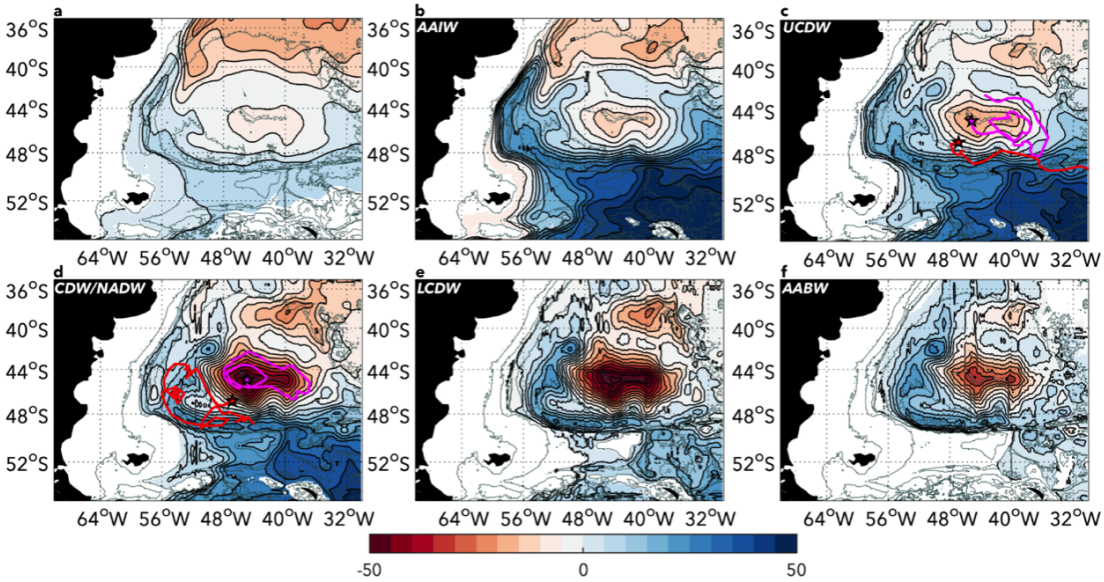

Figure 5.8: a-f) Mean transport stream function (in Sv) integrated over each water mass layer. "Red (blue) is for anticyclonic (cyclonic) circulation. Contours are plotted every 5 Sv. a) Surface waters b) AAIW. c) UCDW. The trajectory of two ARGO floats drifting at 1000m within the UCDW Layer are indicated in magenta (6902850) and red (6902848). d) CDW/NADW, The trajectory of two ARGO floats drifting at 3000m within the CDW/NADW layer are indicated in magenta (6902977) and red (6902992). e) LCDW. f) AABW. The bathymetry contours are plotted in grey (200 m, 2000 m, 3400 m, 3800 m, 3900 m, 5000 m and 6000 m). Note that the ARGO floats trajectories follow the stream lines.

5.3.4 Climate projections on Zapiola circulation

Finally, the evolution of the circulation in the context of climate change is a crucial issue. The majority of the climate models of the Coupled Model Intercomparison Project (CMIP) fail at representing the ZAC due to their coarse resolution. They do not resolve the Rossby radius which is key to the representation of topographic flows such as the ZAC (Hewitt et al., 2020). Indeed, the CMIP models ocean resolution still requires parameterisation of mesoscale eddies which are limited in projecting the future response of the horizontal and vertical circulation under climate warming (AR6 WG I.9). However, a particular attention is given to the effect of the increase resolution in the climate predictions in the High Resolution Model Intercomparison Project (HighResMIP) and Ocean Model Intercomparison Project phase 2 (OMIP-2). Improvement in resolution and parameterisation of eddy-dynamics will probably unable studies on the evolution of eddy-driven circulations (Hewitt et al., 2020).

Appendix: A linear model of topographically trapped waves

Theoretical Framework

We aim at describing the modal structure of coastal trapped waves along the Patagonian shelf break. For that we rely on linear theory of sub-inertial frequency waves (Brink (1989)). We consider a linear, inviscid problem and make Boussinesq and hydrostatic approximation. Dissipative effects are limited to a thin bottom boundary layer.

The unknowns are the velocity (U, V, W), the pressure P, and the density ρ. These variables are decomposed as the sum of a mean plus a small perturbation associated to the wave (allowing us to use linear approximation). As we only consider a meridional mean flow $V_0(x, z)$, we write $U = u(x, y, z, t)$, $V = V_0(x, z) + v(x, y, z, t)$ and $W = w(x, y, z, t)$. The pressure P is $P = P_0(z) + P_1(x, z) + p(x, y, z, t)$ and the density ρ is $\rho = \rho_0 + \rho_\infty(z) + \rho_1(x, z) + \rho(x, y, z, t)$ where $\rho_0 = 1015$ kg m^{-3}, $\rho_\infty(z)$ is the density associated with the mean stratification of the ocean and $\rho_1(x, z)$ is the geostrophically balanced density which depends on the mean flow $V_0(x, z)$.

More precisely, the hydrostatic hypothesis implies for the ocean at rest :

$$P_0(z) = P_{surf} - \rho_0 g z - g \int_0^z \rho_\infty(z) dz$$

where P_{surf} is the surface pressure and $N_\infty^2 = -\dfrac{g}{\rho_0} \partial_z \rho_\infty$. Geostrophy implies $-\rho_0 f V_0(x, z) = -\partial_x P_1(x, z)$.

Assuming that the mean pressure anomaly (related to the mean flow) vanishes when $x \to \infty$, we have

$$P_1(x, z) = \int_\infty^x \rho_0 f V_0(X, z) dX.$$

The hydrostatic hypothesis then makes possible the computation of $\rho_1(x,z)$:

$$\rho_1(x,z) = \frac{-f\rho_0}{g}\int_\infty^x \partial_z V_0(X,z)dX$$

The Brünt-Väisälä frequency $N^2(x,z)$ is now

$$N^2(x,z) = -\frac{g}{\rho_0}\partial_z(\rho_\infty(z) + \rho_1(x,z))$$

and remains close to $N^2_\infty(z)$ except in the areas where the mean current strongly varies. It can be compared to the " horizontal frequency " $M^2(x,z)$:

$$M^2(x,z) = -\frac{g}{\rho_0}\partial_x(\rho_1(x,z)) = f_0\partial_z V_0(x,z)$$

This frequency provides a typical time scale for the oscillations in the cross-shore x direction.

With these assumptions, the linearized equations for the small perturbations (u,v,w), p and ρ are (Brink, 2006) :

- Equations for the horizontal momentum :

$$\begin{aligned} \rho_0(u_t + V_0\, u_y - fv) &= -p_x + \tau^x_z \\ \rho_0(v_t + u\, V_{0,x} + V_0\, v_y + w\, V_{0,z} + fu) &= -p_y + \tau^y_z \end{aligned} \tag{5.1}$$

- Hydrostatic balance for perturbations

$$-p_z - g\rho_2 = 0 \tag{5.2}$$

- Continuity equation (incompressible ocean)

$$u_x + v_y + w_z = 0 \tag{5.3}$$

- Equation of mass conservation

$$\rho_{2,t} + u\,\rho_{1,x} + V_o\,\rho_{2,y} + w\,\partial_z(\rho_\infty + \rho_1) = 0 \tag{5.4}$$

In the following we neglect the dissipative effects due to the stress (τ_x, τ_y) (due to the turbulent nature of the flow). Note that there is a bottom stress $(\tau^x_0,\ \tau^y_0)$ which may be related to the interior bottom velocity by the relations $\tau^x_0 = \rho_0 r u_b$, $\tau^y_0 = \rho_0 r v_b$; here the index $_b$ corresponds to the bottom velocity and r is the bottom resistance coefficient (velocity units). Those fluxes are also neglected for the computation of modal structures just below.

The problem is invariant in alongshore direction y but varies in the cross-shore x and vertical z directions, which makes possible to decompose each variable in the following way:

$$p = \Sigma P_n(x,z) e^{i(\omega_n t + ly)} \tag{5.5}$$

Here l is a prescribed constant associated with the wavelength of the trapped wave and ω_n a family of unknown frequencies which will be determined by solving an eigenvalue problem. With this modal decomposition, hydrostatic balance implies $-g\rho_n(x,z) = \partial_z p_n(x,z)$ and equations 5.1 and 5.4 become

$$\begin{aligned} i\omega' U_n - fV_n &= -\Pi_{n,x} \\ f'U_n + i\omega' V_n + V_{0,z} W_n &= -il\Pi_n \\ sU_n + W_n &= -i(\omega'/N^2)\Pi_{n,z} \end{aligned} \tag{5.6}$$

with $\Pi_n = P_n/\rho_0$, $\omega' = \omega_n + lV_0(x,z)$, $f' = f + V_{0,x}$ and $s = M^2/N^2$ (ω' depends on n but we drop the index to simplify the notation). This yields an explicit expression of velocity as a function of pressure:

$$\begin{aligned} U_n &= i\theta\left[-\Pi_{n,x} + s\Pi_{n,z} - \frac{lf}{\omega'}\Pi_n\right] \\ V_n &= \theta\left[\frac{f^\star}{\omega'}\Pi_{n,x} - \frac{s\omega'}{f}\Pi_{n,z} + l\Pi_n\right] \\ W_n &= i\theta\left[s\Pi_{n,x} - \frac{F^2}{N^2}\Pi_{n,z} + \frac{lfs}{\omega'}\Pi_n\right] \end{aligned} \tag{5.7}$$

where $F^2 = ff' - \omega'^2$, $f^\star = f' - sM^2/f$, $D = ff^\star - \omega'^2 = F^2 - sM^2$ and $\theta = \omega' D^{-1}$. Note that we implicitly assume that $\sqrt{ff'} > \omega'$ if F is real. This means that the period of the trapped waves must exceed a few days. The continuity equation $u_x + ilv + w_z = 0$ yields a unique equation (Brink, 1982) for the reduced pressure Π (we drop below the index $_n$ corresponding to the n mode):

$$\Pi_{xx} - 2s\,\Pi_{xz} + (F/N)^2\,\Pi_{zz} + A\,\Pi_x + B\,\Pi_z + C\,\Pi = 0 \tag{5.8}$$

with $Q = D^{-1}[D_x - D_z]$, $A = -Q - s_z$ and

$$\begin{aligned} B &= -\omega'^{-1}[-\omega' sQ + (\omega' s)_x + lf^{-1}s(f^2 - \omega'^2) - F^2(\omega' N^{-2})_z - (\omega' N^{-2})(sM^2)_z] \\ C &= -\omega'^{-1}[lfQ + \omega' l^2 + lfs_z] \end{aligned} \tag{5.9}$$

As $(F/N)^2 > 0$ the equation is elliptic when $s^2 - (F/N)^2 < 0$ (if F/N is imaginary the equation is always hyperbolic). This condition is realized if $M^2 < FN$. The time scale associated to M (and linked to the vertical variations of the mean current) must therefore exceeds a few days (exactly $2\pi/\sqrt{FN}$) in order to fulfill this condition.

boundary conditions. The following boundary conditions have been introduced by Brink and Chapman (1987) to solve equation 5.8.

- At $x = x_{max}$ (theoretically $x_{max} = \infty$), $Pi = 0$ because of the hypothesis of coastal trapping.
- At $x = 0$ and $x = x_{max}$, there are open boundary conditions $\partial_x u = 0$. Because of the first equation in system (3.7), this condition leads to a complex relation between the derivatives of Π.
- At $z = 0$, $w(x,0) = \dfrac{-1}{g}(\Pi_t + V_0\Pi_y)|_{z=0}$ since the surface is free. Note that if the rigid lid assumption is made the divergence caused by the surface displacement is neglected and the phase speed of the modes increases.
- At $z = -h(x)$, $w(x,-h(x)) + u(x,-h(x))\,\partial_x h = 0$ since no flow perpendicular to the bottom is allowed.

To solve numerically this eigenvalue problem, we used the toolbox developed by Brink and Chapman (Brink and Chapman, 1987). It solves the eigenvalue problem using a technique based on a resonance iteration approach: through boundary conditions, a localized wind stress curl is applied near the center of the grid.

Bottom topography $h(x)$, offshore stratification $N^2_\infty(z)$), mean flow $V_0(x,z)$ and wavenumber l are requested by the program. The program then computes the mean state (see above and next section). For a given alongshore wave number $l = \frac{2\pi}{\lambda}$ with λ the alongshore wavelength, it next searches the real frequency ω_n, the pressure Π_n, the density ρ_n and the velocity (u_n, v_n, w_n) for increasing values of n as explained above.

If the computation is repeated for various l, a dispersion curve is produced for each mode.

Background characteristics and modal structures

Burger number and modal structure

The structure of the modes depends upon the background characteristics such as slope steepness, stratification and mean flow which are deduced from GLORYS12 outputs. The Burger number Bu is the non-dimensional number $Bu = (\frac{\alpha N}{f})^2$ where α is the cross-shore slope in m/m, N the mean coastal Brünt-Väisälä frequency, and f the Coriolis parameter (Figure A1e). For small values of Bu ($Bu < 1$), the rotation dominates over gravity and fast propagating barotropic shelf waves are produced; on the contrary large values of Bu ($Bu > 1$) correspond to slow-propagating baroclinic waves.

Throughout South America, with the exception of the Patagonian Platform (Figure 5.9), the Burger number exceeds one and consistently baroclinic waves are expected. The tropical regions up to 30°S,

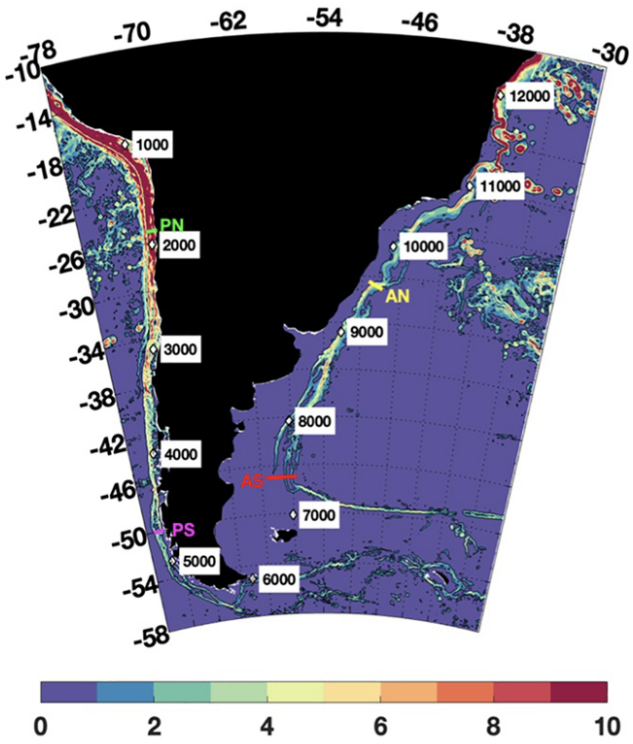

Figure 5.9: Mean Burger number from GLORYS12 over the 1993–2019 period. Black contour is $Bu = 1$

are highly stratified with steep slopes on both the Pacific and Atlantic sides and $Bu \gg 1$. Despite the relatively weak stratification along the southwestern coast of South America, the Burger number surpasses one due to the slope steepness. In contrast, the Patagonian region, which also exhibits weak stratification, features a gentle slope; consequently $Bu \leq 1$ and the waves show a rather barotropic structure.

Background characteristics : implementation of the model

Brink & Chapman toolbox (available at : `https://darchive.mblwhoilibrary.org/entities/publication/50dc38f7-de8f-545f-985d-4b01bcf7ed61`) requires the offshore stratification $N_\infty(z)$, the bathymetry $h(x)$ and the mean along-shore flow (Figure 2.1). We used GLORYS12 outputs along several sections (see Figure 5.10a, and Figures in chapter 3 and 4) to compute them.

The initial version of this toolbox made possible the implementation of a mean along-shore flow formed by an unique jet modeled by a decaying Gaussian curve. As the mean flow along the Patagonian platform is formed by two jets at some points we modified this version introducing a second decaying Gaussian curve and obtained the mean flows presented in Figures 5.10f-g. We took the same stratification

for the three sections as the Malvinas current system is homogeneously stratified and present a weak seasonal cycle (Artana et al., 2021).

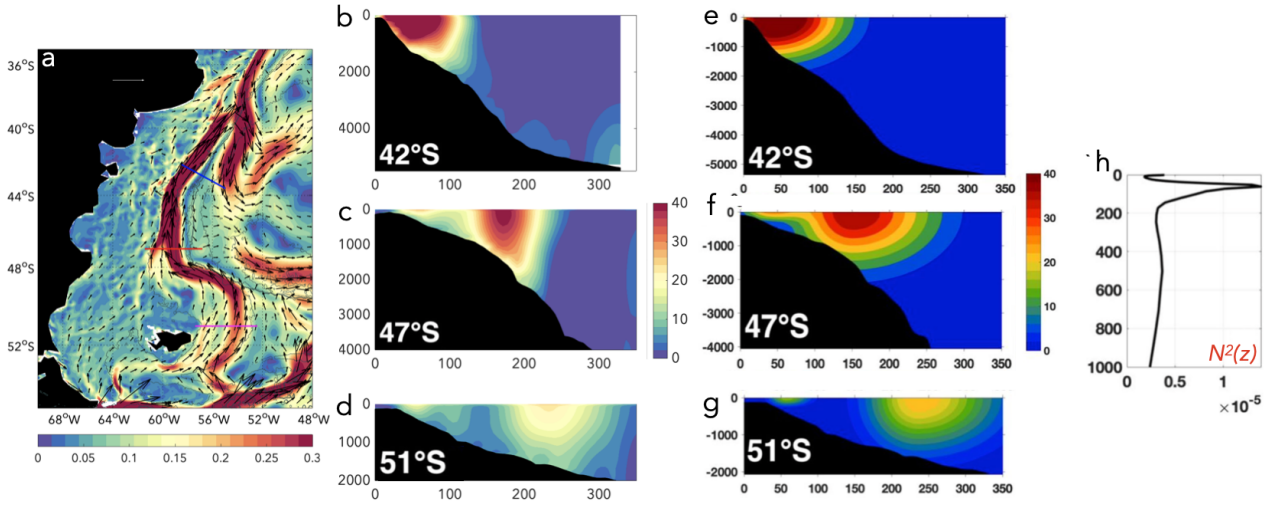

Figure 5.10: a) Mean Surface velocities and mean intensity in (m/s) over 1993-2019 period from GLORYS12. Magenta, red and blue lines correspond to the studied sections called 51°S, 47°S and 42°S respectively. b-c-d) Mean along slope velocities from GLORYS12. e-f-g) Mean flow modelled with the Brink & Chapman toolbox. h) Mean stratification used for the model implementation from GLORYS12.

Idealized modal structures and dispersion curves

The toolbox computes the dispersion curves (see below and Figure 5.12) and the structure of the modes giving the pressure, along-shore and across-shore velocities, density, vertical velocity and surface pressure. Figure 5.11 shows the first four gravest modes of along-shore velocity in cm/s normalized under the assumption of energy conservation ($\int \int p^2 dxdz = 1$ according to Brink (1989)).

The toolbox also computes the dispersion curves (Figure 5.12). The long waves at low frequency are non-dispersive (Figure 5.12a). When the order of the mode increases, the phase speed decreases.

Sensitivity tests showed that the amplitude of the generated anomalies decreases when the stratification increases (inhibition of the anomalies by the stratification); moreover the structure becomes more baroclinic, both frequency and phase speed increase and the wave dissipates faster.

For 1500 km (consistent with the length of the Patagonian slope of the order of 3000 km), the theory computed waves with periods ranging between 1 and 30 days and phase speeds between 0.30 and 8.00 m/s (Figures 5.12). In spite of idealized assumptions such as a straight coastline with uniform shelf bathymetry, which is not the case of the Patagonian slope, the analysis provided some insight in the modal structure of TW.

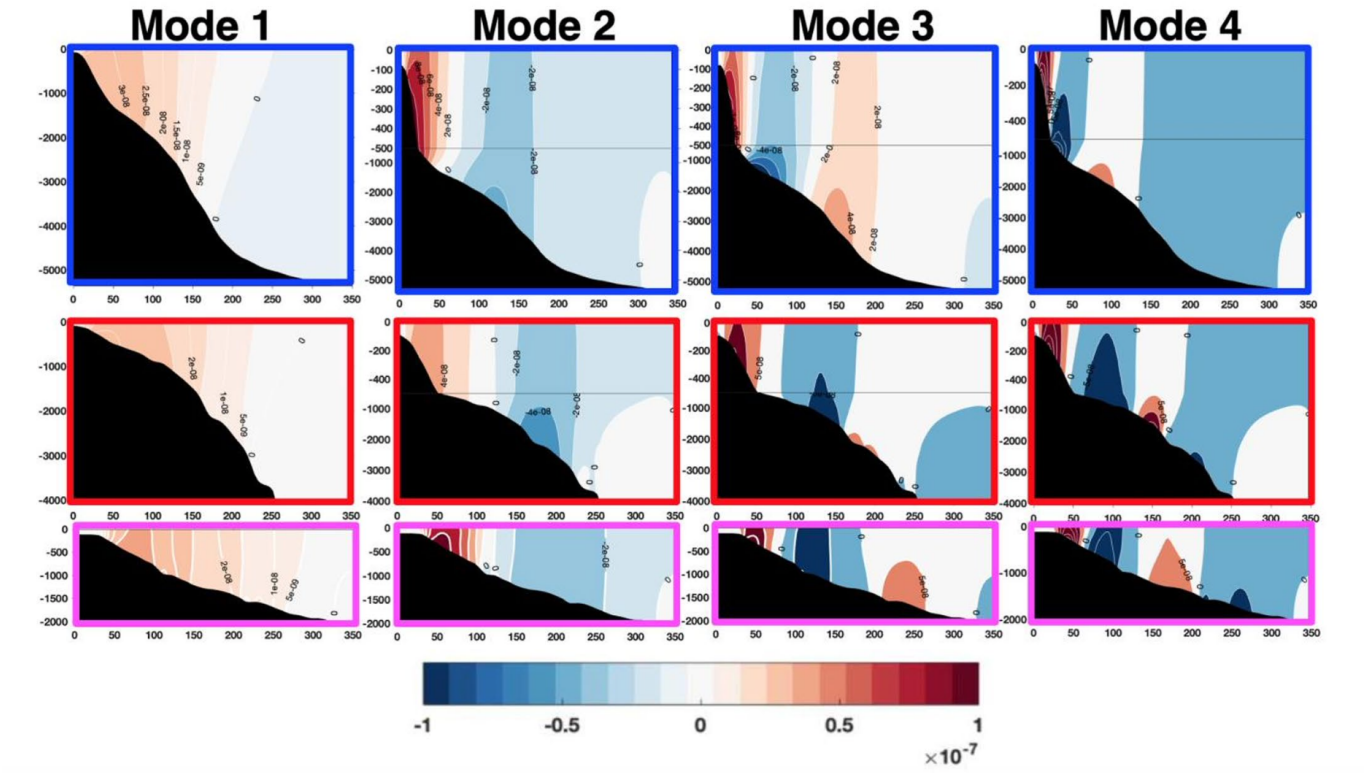

Figure 5.11: First four gravest modes of along-isobath velocity computed from Brink and Chapman (1987) toolbox at 51°S, 47°S and 42°S (pink, red, and blue sections in Figure 5.10) (the velocities are normalized consistently). x-axis is across-slope distance; y-axis is the depth.

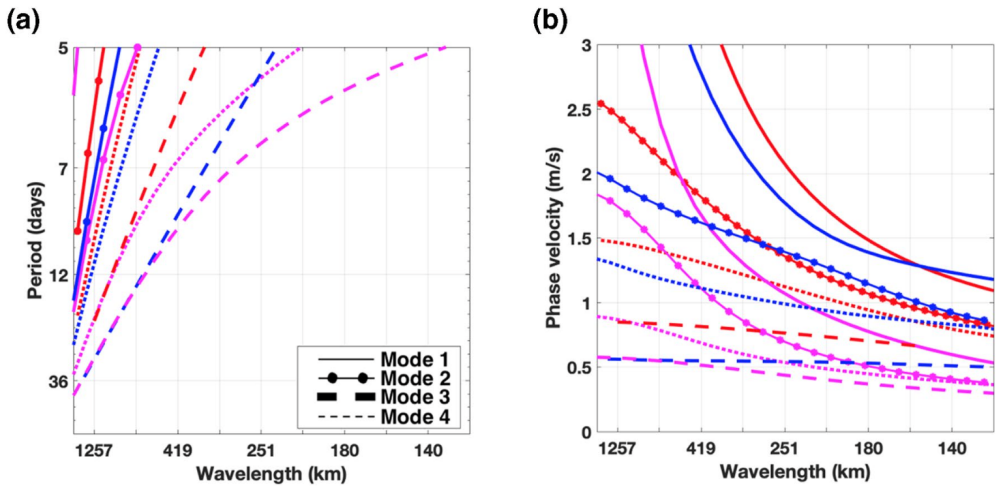

Figure 5.12: a) Dispersion curves for the first four gravest modes of the 51°S section (pink), 47°S section (red) and 42°S section (blue). x-axis is the wavelength in km, y-axis is the period in days. Thick lines correspond to mode 1, thick lines with dots to mode 2, thick dashed lines to mode 3, and dashed lines to mode 4. b) Phase velocity computed for each mode (same color code as a). x-axis is wavelength in km and y-axis is the velocity in m/s.

References

Acha, E. M., Mianzan, H. W., Guerrero, R. A., Favero, M., Bava, J. (2004). Marine fronts at the continental shelves of austral South America: physical and ecological processes. Journal of Marine systems, 44(1-2), 83-105.

Agra, C., Nof, D. (1993). Collision and separation of boundary currents. Deep Sea Research Part I: Oceanographic Research Papers, 40(11-12), 2259-2282. Archer, M. R., Li, Z., Fu, L.-L. (2020). Increasing the space–time resolution of mapped sea surface height from altimetry. Journal of Geophysical Research: Oceans, 124, e2019JC015878. https://doi.org/10.1029/2019JC015878.

Artana, C., Ferrari, R., Koenig, Z., Saraceno, M., Piola, A. R., Provost, C. (2016). Malvinas Current variability from Argo floats and satellite altimetry. Journal of Geophysical Research: Oceans, 121(7), 4854–4872. https://doi.org/10.1002/2016JC011889

Artana, C., Lellouche, J., Park, Y., Garric, G., Koenig, Z., Sennéchael, N., et al. (2018a). Fronts of the Malvinas Current System: Surface and Subsurface Expressions Revealed by Satellite Altimetry, Argo Floats, and Mercator Operational Model Outputs. Journal of Geophysical Research: Oceans, 123(8), 5261–5285. https://doi.org/10.1029/2018JC013887

Artana, C., Ferrari, R., Koenig, Z., Sennéchael, N., Saraceno, M., Piola, A. R., Provost, C. (2018b). Malvinas Current Volume Transport at 41°S: A 24 Yearlong Time Series Consistent With Mooring Data From 3 Decades and Satellite Altimetry. Journal of Geophysical Research: Oceans, 123(1), 378–398. https://doi.org/10.1002/2017JC013600

Artana, C., Lellouche, J.-M., Sennéchael, N., Provost, C. (2018c). The Open-Ocean Side of the Malvinas Current in Argo Floats and 24 Years of Mercator Ocean High-Resolution (1/12) Physical Reanalysis. Journal of Geophysical Research: Oceans, 123(11), 8489–8507. https://doi.org/10.1029/2018JC014528

Artana, C., Provost, C., Lellouche, J., Rio, M., Ferrari, R., Sennéchael, N. (2019). The Malvinas Cur-

rent at the Confluence With the Brazil Current: Inferences From 25 Years of Mercator Ocean Reanalysis. Journal of Geophysical Research: Oceans, 124(10), 7178–7200. https://doi.org/10.1029/2019JC015289

Artana, C., Provost, C., Poli, L., Ferrari, R., Lellouche, J. (2021). Revisiting the Malvinas Current Upper Circulation and Water Masses Using a High-Resolution Ocean Reanalysis. Journal of Geophysical Research: Oceans, 126(6). https://doi.org/10.1029/2021JC017271

Ballarotta, M., Ubelmann, C., Pujol, M.-I., Taburet, G., Fournier, F., Legeais, J.-F., et al. (2019). On the resolutions of ocean altimetry maps. Ocean Science, 15(4), 1091–1109. https://doi.org/10.5194/os-15-1091-2019

Barré, N., Provost, C., Saraceno, M. (2006). Spatial and temporal scales of the Brazil–Malvinas Current confluence documented by simultaneous MODIS Aqua 1.1-km resolution SST and color images. Advances in Space Research, 37(4), 770–786. https://doi.org/10.1016/j.asr.2005.09.026

Bigorre, S., Dewar, W. K. (2009). Oceanic time variability near a large scale topographic circulation. Ocean Modelling, 29(3), 176–188. https://doi.org/10.1016/j.ocemod.2009.04.004

Brand, S. V. S., Prend, C. J., Talley, L. D. (2023). Modification of North Atlantic Deep Water by Pacific/Upper Circumpolar Deep Water in the Argentine Basin. Geophysical Research Letters, 50, e2022GL099419. https://doi.org/10.1029/2022GL099419

Brink, K. H., Chapman, D. C. (1987). Programs for computing properties of coastal-trapped waves and wind-driven motions over the continental shelf and slope (Technical Report WHOI-87-24, p. 122). Woods Hole, MA: Woods Hole Institution.

Brink, K. H. (1989). Energy conservation in coastal-trapped wave calculations. Journal of Physical Oceanography, 19, 1011–1016.

Colin De Verdière, A., Ollitrault, M. (2016). A Direct Determination of the World Ocean Barotropic Circulation. Journal of Physical Oceanography, 46(1), 255–273. https://doi.org/10.1175/JPO-D-15-0046.1

De Freitas, P. P., Paiva, A. D. M., Cirano, M., Mill, G. N., Da Costa, V. S., Gabioux, M., França, B. R. L. (2021). Coastal trapped waves propagation along the Southwestern Atlantic Continental Shelf. Continental Shelf Research, 226, 104496. https://doi.org/10.1016/j.csr.2021.104496

De Miranda, A. P., Barnier, B., Dewar, W. K. (1999). On the dynamics of the Zapiola Anticyclone. Journal of Geophysical Research: Oceans, 104(C9), 21137–21149. https://doi.org/10.1029/1999JC900042

Ewing, M., Ludwig, W. J., Ewing, J. I. (1964). Sediment distribution in the oceans: The argentine basin. Journal of Geophysical Research, 69(10), 2003–2032. https://doi.org/10.1029/JZ069i010p02003

Ferrari, R., Artana, C., Saraceno, M., Piola, A. R., Provost, C. (2017). Satellite Altimetry and Current-Meter Velocities in the Malvinas Current at 41°S: Comparisons and Modes of Variations. Journal of Geophysical Research: Oceans, 122(12), 9572–9590. https://doi.org/10.1002/2017JC013340

Flood, R. D., Shor, A. N. (1988). Mud waves in the Argentine Basin and their relationship to regional bottom circulation patterns. Deep Sea Research Part A. Oceanographic Research Papers, 35(6), 943–971. https://doi.org/10.1016/0198-0149(88)90070-2

Fox-Kemper, B., H.T. Hewitt, C. Xiao, G. Aðalgeirsdóttir, S.S. Drijfhout, T.L. Edwards, N.R. Golledge, M. Hemer, R.E. Kopp,G. Krinner, A. Mix, D. Notz, S. Nowicki, I.S. Nurhati, L. Ruiz, J.-B. Sallée, A.B.A. Slangen, and Y. Yu, 2021: Ocean,Cryosphere and Sea Level Change. In Climate Change 2021: The Physical Science Basis. Contribution of Working Group I to the Sixth Assessment Report of the Intergovernmental Panel on Climate Change [Masson-Delmotte, V., P. Zhai, A. Pirani, S.L. Connors, C. Péan, S. Berger, N. Caud, Y. Chen, L. Goldfarb, M.I. Gomis, M. Huang, K. Leitzell, E.Lonnoy, J.B.R. Matthews, T.K. Maycock, T. Waterfield, O. Yelekçi, R. Yu, and B. Zhou (eds.)].

Cambridge University Press,Cambridge, United Kingdom and New York, NY, USA, pp. 1211–1362, doi:10.1017/9781009157896.011

Frey, D. I., Piola, A. R., Krechik, V. A., Fofanov, D. V., Morozov, E. G., Silvestrova, K. P., et al. (2021). Direct Measurements of the Malvinas Current Velocity Structure. Journal of Geophysical Research: Oceans, 126(4). https://doi.org/10.1029/2020JC016727

Fu, L.-L., Cheng, B., & Qiu, B. (2001). 25-Day Period Large-Scale Oscillations in the Argentine Basin Revealed by the TOPEX/Poseidon Altimeter. Journal of Physical Oceanography, 31(2), 506–517. https://doi.org/10.1175/1520-0485(2001)031<0506:DPLSOI>2.0.CO;2

Gordon, A. L., Greengrove, C. L. (1986). Geostrophic circulation of the Brazil-Falkland confluence. Deep Sea Research Part A. Oceanographic Research Papers, 33(5), 573–585. https://doi.org/10.1016/0198-0149(86)90054-3

Hewitt, H.T., Roberts, M., Mathiot, P. et al. Resolving and Parameterising the Ocean Mesoscale in Earth System Models. Curr Clim Change Rep 6, 137–152 (2020). https://doi.org/10.1007/s40641-020-00164-w

Hughes, C. W., V. N. Stepanov, L.-L. Fu, B. Barnier, and G. W. Hargreaves (2007), Three forms of variability in Argentine Basin ocean bottom pressure, J. Geophys. Res., 112, C01011, doi:10.1029/2006JC003679.
Huthnance, J. M. (1995). Circulation, exchange and water masses at the ocean margin: the role of physical processes at the shelf edge. Progress in Oceanography, 35(4), 353-431.

Lellouche, J-M. Greiner, E., Bourdallé-Badie, R., Garric, G., Melet, A., Drévillon, M., Bricaud, C., (2021). The Copernicus Global 1/12° Oceanic and Sea Ice GLORYS12 Reanalysis. Frontiers in Earth Science, 9, 698876. https://doi.org/10.3389/feart.2021.698876

Le Pichon, X., Eittreim, S. L., Ludwig, W. J. (1971). Sediment transport and distribution in the

Argentine Basin. 1. Antarctic Bottom Current passage through the Falkland fracture zone.Physics and Chemistry of the Earth,8, 3-28.

Johnson, G. C., King, B. A. (2023). Zapiola Gyre, Velocities and Mixing, New Argo Insights. Journal of Geophysical Research: Oceans, 128(6), e2023JC019893. https://doi.org/10.1029/2023JC019893

Jullion, L., Heywood, K. J., Naveira Garabato, A. C., Stevens, D. P. (2010). Circulation and Water Mass Modification in the Brazil–Malvinas Confluence. Journal of Physical Oceanography, 40(5), 845–864. https://doi.org/10.1175/2009JPO4174.1

Mason, E., Pascual, A., Gaube, P., Ruiz, S., Pelegrí, J. L., Delepoulle, A. (2017). Subregional characterization of mesoscale eddies across the B razil- M alvinas C onfluence. Journal of Geophysical Research: Oceans, 122(4), 3329–3357. https://doi.org/10.1002/2016JC012611

Matano, R. P. (1993). On the separation of the Brazil Current from the coast. Journal of Physical Oceanography, 23(1), 79-90.

Matano, R. P., Palma, E. D. (2008). On the Upwelling of Downwelling Currents. Journal of Physical Oceanography, 38(11), 2482–2500. https://doi.org/10.1175/2008JPO3783.1

Paniagua, G. F., Saraceno, M., Piola, A. R., Charo, M., Ferrari, R., Artana, C., Provost, C. (2021). Malvinas current at 44.7°S: First assessment of velocity temporal variability from in situ data. Progress in Oceanography, 195, 102592. https://doi.org/10.1016/j.pocean.2021.102592

Peterson, R. G., Whitworth, T. (1989). The subantarctic and polar fronts in relation to deep water masses through the southwestern Atlantic. Journal of Geophysical Research, 94(C8), 10817. https://doi.org/10.1029/JC094iC08p10817

Piola, A. R., Franco, B. C., Palma, E. D., Saraceno, M. (2013). Multiple jets in the Malvinas Cur-

rent: MULTIPLE JETS IN THE MALVINAS CURRENT. Journal of Geophysical Research: Oceans, 118(4), 2107–2117. https://doi.org/10.1002/jgrc.20170

Poli, L., Artana, C., Provost, C., Sirven, J., Sennéchael, N., Cuypers, Y., Lellouche, J. (2020). Anatomy of Subinertial Waves Along the Patagonian Shelf Break in a 1/12° Global Operational Model. Journal of Geophysical Research: Oceans, 125(12). https://doi.org/10.1029/2020JC016549

Poli, L., Artana, C., Provost, C. (2022).Topographically Trapped Waves Around South America With Periods Between 40 and 130 Days in a Global Ocean Reanalysis. Journal of Geophysical Research: Oceans, 127(2). https://doi.org/10.1029/2021JC018067

Poli, L., Artana, C.,Provost, C., Siven,J., Le Blanc-Pressenda,R., Collapses, maxima, multi-year modulation and trends of the Zapiola anticyclone: insights from Mercator Reanalysis.(submitted)

Ponte, A. L., Klein, P., Dunphy, M., Le Gentil, S. (2017). Low-mode internal tides and balanced dynamics disentanglement in altimetric observations: Synergy with surface density observations: SLOW VERSUS FAST SIGNATURES ON SEA LEVEL. Journal of Geophysical Research: Oceans, 122(3), 2143–2155. https://doi.org/10.1002/2016JC012214

Provost, C., Gana, S., Garçon, V., Maamaatuaiahutapu, K., England, M. (1995). Hydrographic conditions in the Brazil-Malvinas Confluence during austral summer 1990. Journal of Geophysical Research, 100(C6), 10655. https://doi.org/10.1029/94JC02864

Pujol, M.-I., Faugère, Y., Taburet, G., Dupuy, S., Pelloquin, C., Ablain, M., Picot, N. (2016). DUACS DT2014: the new multi-mission altimeter data set reprocessed over 20years. Ocean Science, 12(5), 1067–1090. https://doi.org/10.5194/os-12-1067-2016

Rodhouse, P. G., Elvidge, C. D., Trathan, P. N. (2001). Remote sensing of the global light-fishing fleet: an analysis of interactions with oceanography, other fisheries and predators. Academic Press.

Romero, S. I., Piola, A. R., Charo, M., Garcia, C. A. E. (2006). Chlorophyll- a variability off Patagonia based on SeaWiFS data. Journal of Geophysical Research, 111(C5), C05021. https://doi.org/10.1029/2005JC003244

Saunders, P. M., King, B. A. (1995). Bottom currents derived from a shipborne ADCP on WOCE cruise A11 in the South Atlantic. Journal of Physical Oceanography, 25(3), 329-347.

Saraceno, M., Provost, C., Piola, A. R. (2005). On the relationship between satellite-retrieved surface temperature fronts and chlorophyll a in the western South Atlantic. Journal of Geophysical Research, 110(C11), C11016. https://doi.org/10.1029/2004JC002736

Saraceno, M., Provost, C., Zajaczkovski, U. (2009). Long-term variation in the anticyclonic ocean circulation over the Zapiola Rise as observed by satellite altimetry: Evidence of possible collapses. Deep Sea Research Part I: Oceanographic Research Papers, 56(7), 1077–1092. https://doi.org/10.1016/j.dsr.2009.03.005

Saraceno, M., Provost, C. (2012). On eddy polarity distribution in the southwestern Atlantic. Deep Sea Research Part I: Oceanographic Research Papers, 69, 62–69. https://doi.org/10.1016/j.dsr.2012.07.005

Spadone, A., Provost, C. (2009). Variations in the Malvinas Current volume transport since October 1992. Journal of Geophysical Research, 114(C2), C02002. https://doi.org/10.1029/2008JC004882

Taburet, G., Sanchez-Roman, A., Ballarotta, M., Pujol, M.-I., Legeais, J.-F., Fournier, F., et al. (2019a). DUACS DT2018: 25 years of reprocessed sea level altimetry products. Ocean Science, 15(5), 1207–1224. https://doi.org/10.5194/os-15-1207-2019

Valla, D., Piola, A. R. (2015). Evidence of upwelling events at the northern P atagonian shelf break. Journal of Geophysical Research: Oceans, 120(11), 7635–7656. https://doi.org/10.1002/2015JC011002

Valla, D., Piola, A. R., Meinen, C. S., Campos, E. (2018). Strong mixing and recirculation

in the northwestern Argentine Basin. Journal of Geophysical Research: Oceans, 123, 4624– 4648. https://doi.org/10.1029/2018JC013907

Venables, H., and C. M. Moore (2010), Phytoplankton and light limitation in the Southern Ocean: Learning from highnutrient, high-chlorophyll areas, J. Geophys. Res., 115, C02015, doi:10.1029/2009JC005361.

Vivier, F., Provost, C. (1999). Direct velocity measurements in the Malvinas Current. Journal of Geophysical Research: Oceans, 104(C9), 21083–21103. https://doi.org/10.1029/1999JC900163

Vivier, F., Provost, C., Meredith, M. P. (2001). Remote and Local Forcing in the Brazil–Malvinas Region. Journal of Physical Oceanography, 31(4), 892–913. https://doi.org/10.1175/1520-0485(2001)031<0892:RALFIT>2.0

Von Schuckmann, K., Cheng, L., Palmer, M. D., Hansen, J., Tassone, C., Aich, V., et al. (2020). Heat stored in the Earth system: where does the energy go? Earth System Science Data, 12(3), 2013–2041. https://doi.org/10.5194/essd-12-2013-2020

Weijer, W., Vivier, F., Gille, S. T., & Dijkstra, H. A. (2007a). Multiple oscillatory modes of the Argentine Basin. Part I: Statistical analysis. Journal of Physical Oceanography, 37(12), 2855-2868.

Weijer, W., Vivier, F., Gille, S. T., & Dijkstra, H. A. (2007b). Multiple oscillatory modes of the Argentine Basin. Part II: The spectral origin of basin modes. Journal of physical oceanography, 37(12), 2869-2881.

Whalen, C. B., Talley, L. D., and MacKinnon, J. A. (2012), Spatial and temporal variability of global ocean mixing inferred from Argo profiles, Geophys. Res. Lett., 39, L18612, doi:10.1029/2012GL053196.

Whalen, C.B., MacKinnon, J.A. Talley, L.D. Large-scale impacts of the mesoscale environment on mixing from wind-driven internal waves. Nature Geosci 11, 842–847 (2018). https://doi.org/10.1038/s41561-018-0213-6

Weatherly, G. L. (1993). On deep-current and hydrographic observations from a mudwave region and elsewhere in the Argentine Basin. Deep Sea Research Part II: Topical Studies in Oceanography, 40(4–5), 939–961. https://doi.org/10.1016/0967-0645(93)90042-L

Whitworth, T., Nowlin, W. D., Pillsbury, R. D., Moore, M. I., Weiss, R. F. (1991). Observations of the Antarctic Circumpolar Current and deep boundary current in the southwest Atlantic. Journal of Geophysical Research, 96(C8), 15105. https://doi.org/10.1029/91JC01319